UNIVERSITÀ
DEGLI STUDI
FIRENZE

DOTTORATO DI RICERCA IN
Energetica e Tecnologie Industriali e Ambientali Innovative

CICLO XXVIII

COORDINATORE Prof. Maurizio De Lucia

Single & Two-Phase Supersonic Ejectors for Refrigeration Applications

Settore Scientifico Disciplinare Ing/Ind 10

Tutor
Prof. Grazzini Giuseppe

Dottorando
Dott. Mazzelli Federico

Co-Tutor
Ing. Adriano Milazzo

Coordinatore
Prof. De Lucia Maurizio

Anni 2012/2015

Single & Two-Phase Supersonic Ejectors for Refrigeration Applications

Abstract

At a first glance, the nature of this thesis may be considered somehow “sui generis”. By the author’s choice, its structure is not conceived as a report of the doctoral activities, but rather as a guide that can help the reader to appreciate the phenomena and critical points arising in the context of supersonic ejector research.

The rationale for this choice has progressively appeared clear in the course of the doctoral period. During the last two decades, the literature on ejector refrigeration has become mostly self-referential. However, deep understanding of the physics governing both single- and two-phase high-speed phenomena requires a strong effort in terms of “broadening the research horizons”. Work of high relevance to supersonic ejectors can be found in the fields of aerospace propulsion, wind tunnel, steam turbines and turbomachinery cavitation research areas. Consequently, the character of this dissertation is shaped by the firm belief that major advancements may only come by joining together the knowledge from all these different disciplines. Under this perspective, the main results of this three-year doctoral research should not only be considered the achievements in ejector chiller performances or the developments of analytical and numerical tools, but also the opening-up to different research fields and the elaboration of a logical structure where all the themes are rationally presented.

The thesis is divided into three main parts. The first chapters of each part are devoted to literature reviews and in-depth investigation of theoretical concepts. The reader who is already familiar with these aspects may skip these sections and find novel results in the corresponding second chapters.

Part I of the thesis introduces the reader to the basic ideas of ejector refrigeration. In the first chapter of this Part, the state of the art as well as the history and future perspective of this technology are discussed. Chapter 2 is devoted to the presentation of the results obtained with the industrial prototype developed by the University of Florence as well as to the development of rigorous tools for the analysis and optimization of ejectors and ejector cycles. Part II is concerned with the physics and modeling of single-phase supersonic ejectors. Specifically, Chapter 3 proposes a detailed examination of the phenomena occurring in the various ejector regions. In Chapter 4, the discussion concentrates on the problems related to the numerical and analytical modeling of single-phase ejectors. The knowledge of the single-phase aspects sets the basis to move on the more complex features of two-phase supersonic ejectors, explored in Part III. In Chapter 5, the physics of high-speed condensation is thoroughly investigated both from the point of view of macroscopic and microscopic behavior. Finally, chapter 6 concludes this work by focusing on the numerical modeling of condensing ejectors.

Table of Contents

Nomenclature

Latin letters:

a	sound speed [m s^{-1}]
A	Cross sectional area [m^2]
B	Second Virial coefficient [m^3 kg^{-1}]
C	Third Virial coefficient [m^6 kg^{-2}]
C_f	Skin friction coefficient [-]
C_p	Isobaric heat capacity [J K^{-1}]
C_v	Isochoric heat capacity [J K^{-1}]
$\dot{C}$	condensation rate [molecules s^{-1}]
$\dot{E}$	evaporation rate [molecules s^{-1}]
$\dot{E}x$	exergy flux [W]
F	Helmholtz free energy [J]
G	Gibbs free energy [J]
h	static enthalpy [J kg^{-1}]
h_{lv}	Latent heat of vaporization [J kg^{-1}]
J	nucleation rate [molecules s^{-1}]
$\dot{I}$	nucleation current [molecules s^{-1}]
k	Thermal conductivity [W m^{-1} K^{-1}]
k	Boltzmann constant [J K^{-1}]
K	Surface roughness [m]
ℓ	Molecular mean free path [m]
M	Mach number [-]
M_c	Convective Mach number [-]
m	mass of one molecule [kg]
$\dot{m}$	mass flow rate [kg s^{-1}]
n	cluster population [n. clusters m^{-3}]
n'	equilibrium cluster population [n. clusters m^{-3}]
p	pressure [Pa] or multiples
q	Specific Heat [J kg^{-1}]
q_C	Condensation accommodation coefficient [-]
q_E	Evaporation accommodation coefficient [-]
Q	Heat [J]
$\dot{Q}$	Heat flux [W]
R	specific gas constant [J kg^{-1} K^{-1}]
r	velocity ratio (chapter 3 and 4)
r	droplet radius [m] (chapter 5 and 6)

Greek letters:

α	Shape coefficient (chapter 4.1)
β	Shape coefficient (chapter 4.1)
β	liquid mass fraction (chapter 6)
γ	Specific heat ratio [-]
Γ	liquid mass generation rate [kg s^{-1}]
δ_ω	Shear layer vorticity thickness [m]
δ_ω'	vorticity thickness spreading rate [-]
ζ	general variable
Δ	variation
ξ	Kantrowitz non isothermal correction
η	efficiency
η	square root of density ratio (chapt. 3- 4)
η	number of droplets (chapter 6)
μ	dynamic viscosity [Pa s]
ρ	density [kg m^{-3}]
σ	surface tension [J m^{-2}]
τ	shear stress [Pa]
φ_{ss}	degree of supersaturation [-]
φ_{sc}	degree of supercooling [K]

Subscripts & superscripts:

0	reference conditions
II	Second-law
∞	isentropic region quantity
a	arithmetic
c	critical
Cond	Condenser
d	droplet
dsl	dividing streamline
D	Discharge
DPR	Discharge Pressure Ratio
e	external
E, eva	Evaporator
ec	ejector cycle
EER	Ejector Entrainment Ratio

s	specific entropy [J kg^{-1} K^{-1}]
S	Entropy [J K^{-1}]
$\dot{S}$	entropy generation [W K^{-1}]
t	Time [s]
T	Temperature [K] or [°C]
U, u	velocity [m s^{-1}]
U	Internal energy [J] (chapter 5)
v	Specific volume [m^3 kg^{-1}]
V	Volume [m^3]
w	specific work [J kg^{-1}]
W	Work [J]
$\dot{W}$	Power [W]
x	longitudinal coordinate [m]
y	transversal coordinate [m]

Acronyms and dimensionless numbers:

COP	Coefficient of Performance
ER	Entrainment Ratio
Gb	Gibbs number
Kn	Knudsen number
NXP	Nozzle Exit Plane
P	Prandtl number
Re	Reynolds Number

G, gen	Generator
i	internal
l	liquid
m	motive
m	mixture (chapter 6)
n	nucleation
NISO	Non Isothermal
r	refrigeration
RDP	Reversible Discharge Pressure
rev	reversible
rms	root mean square
s	secondary or suction
s	saturation (chapter 5 and 6)
sl	shear layer
t	turbulent
v	vapor
vc	vapor compression
w	wall
x	size of cluster group
–	(overbar) Arithmetic average
–	(overbar) Reynolds average (chapt. 4)
~	(overbar) Favre average

Part I – Ejector Refrigeration

Chapter's index:

Supersonic ejectors are passive compression devices that can be employed for a range of applications, from aeronautic high-speed propulsion systems (Papamoschou, 1993; Alperin and Wu, 1983) to nuclear reactor cooling (Cattadori *et al.*, 1995; Narabayashi *et al.*, 1997), pumping of volatile fluids in power plants and compression of working fluid in refrigeration systems (Chunnanond and Aphornratana, 2004). In particular, the use of ejectors in refrigeration applications discloses promising alternatives to standard vapor compression and absorption cycles. These alternatives constitute the subject of chapter 1.

The standard configuration of the Supersonic Ejector Cycle is illustrated in details in chapter 1.1. Chapters 1.2 and 1.3 illustrate the many alternative applications and ejector cycle configurations. After this brief review of the state-of-the-art, a glimpse is directed toward the historical route that supersonic ejectors have gone through in the last two centuries (chapter 1.4). The twisting path and the alternating fortunes of this technology, more than being of historical interest, give hints on the future possibilities of employment in the field of cold production. This is the subject of chapter 1.5.

The goal of chapter 2 is the description of ways in which performance could be measured and optimized. Chapter 2.1 is devoted to the presentation of the results obtained with the industrial prototype developed by the University of Florence. In chapters 2.2 and 2.3 various forms of Second Law efficiency will be illustrated both for the ejector refrigerator as a whole and for the supersonic ejector alone. It will be shown that some definitions provide more cogent information than others depending on the specific type of application. Although the use of Second Law or exergy analyses are tools by which any thermodynamic analysis cannot spare, the assessment and project of a thermal machine cannot be made just in terms of efficiency. The last section of chapter 2 proposes a somewhat speculative discussion about the definition of a more reasonable and complete objective function than the sole thermodynamic efficiency.

1. Overview

Despite more than a century of history, to date ejector refrigeration should be considered more as a promising perspective than a concrete industrial reality. The causes for this have historical roots that can be traced back to the period that followed the development of synthetic refrigerants and vapor compression devices (see chapter 1.4). Nevertheless, despite the lack of a strong industrial thrust, the scientific research on ejector refrigeration has never disappeared completely but has kept on searching for new ways to exploit these systems. The reason for this is probably related to the appealing idea of using such a simple device to produce something as precious as cold. As a result, a real plethora of cycle configurations and applications has seen the light during the last century of research.
Therefore, this chapter is intended to give a bird-eye-view over the broad landscape of ejector refrigeration.

1.1 Standard configuration

The scheme of a standard Supersonic Ejector Cycle is shown in Fig. 1.1. The configuration is similar to that of a conventional vapor compression machine, except the mechanical compressor is replaced by a system composed by a liquid feed-pump, vapor generator and supersonic ejector. The operation of the cycle is quite simple: the "primary" or "motive" stream arriving from the generator (high pressure and temperature – point G) flows through a de Laval nozzle and accelerates to supersonic speed. As it enters the mixing chamber, the primary stream entrains the "secondary" or "suction" flow coming from the evaporator at state E. The two streams mix and kinetic energy is transferred from the primary to the secondary fluid. Subsequently, the mixed stream is compressed as it flows through the diffuser section of the ejector and enters the condenser at point C. The condensate is then split into two currents: one is expanded through a throttling valve and fed back to the evaporator whilst the other is returned to the boiler via a feed pump.

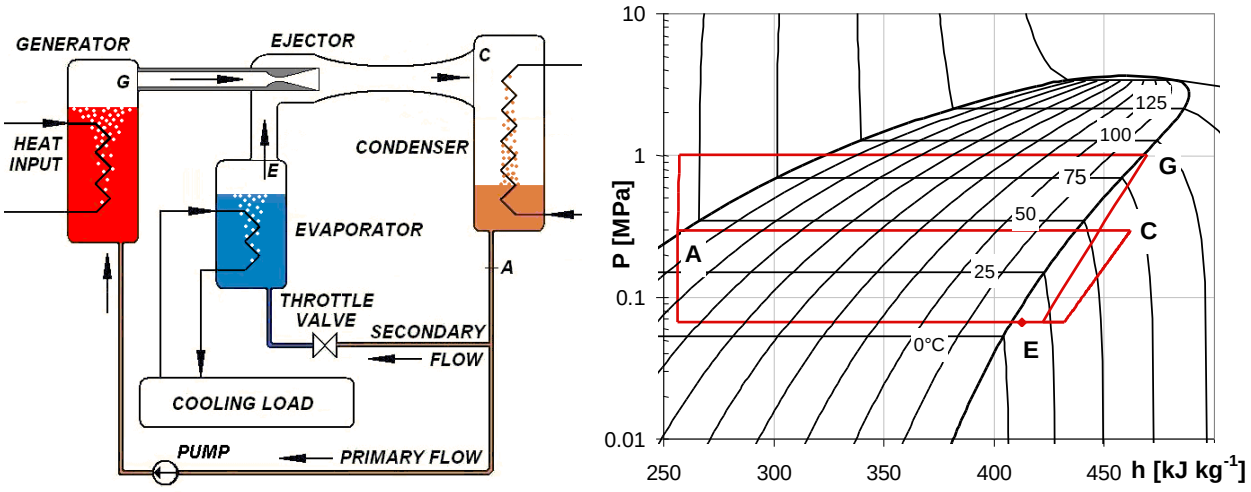

Fig. 1.1 – Schematics of the ejector refrigeration system and corresponding *p-h* diagram

Basically, the whole system can be thought as composed of two parts, the power and refrigeration cycles. The two cycles share the condenser and the power exchange between them occurs by means of a supersonic ejector. Under stationary conditions the power output of the motive cycle must equate that absorbed by the chiller.

System performance can be quantified by means of the Coefficient Of Performance (COP) which is defined as the cooling load divided by the total heat and mechanical power inputs:

$$COP = \frac{\dot{Q}_{refr}}{\dot{Q}_{gen} + \dot{W}_{pump}} = \frac{\dot{m}_s}{\dot{m}_m} \frac{(h_E - h_A)}{(h_G - h_A)} \qquad \text{eq. 1-1}$$

The *p-h* diagram in Fig. 1.1 qualitatively illustrates the ratio between enthalpy differences in eq. 1-1.
The ratio between the suction to motive mass flow rates defines the Entrainment Ratio (ER), which is a fundamental parameter for the performance of both the ejector chiller and the supersonic ejector:

$$ER = \frac{\dot{m}_s}{\dot{m}_m} \qquad \text{eq. 1-2}$$

Fig. 1.2 shows a typical supersonic ejector operating curve obtained at fixed evaporator and generator conditions and varying outlet pressure[1]. The ejector's operation is said to be "on design" or in "double-chocking regime" when the mixed flow in the mixing chamber/diffuser reaches supersonic speed. Under these conditions the quantity of entrained suction flow is independent of the discharge pressure (i.e., it is choked, whence the name double-chocking regime) and the Entrainment Ratio (ER) is maximum. This region is the horizontal part of the operating curve in Fig. 1.2, also called "the plateau". On the contrary, if the mixed (or better partially-mixed) flow is subsonic, the amount of suction flow drawn into the ejector depends almost linearly on the outlet pressure and the operation is said to be ''off-design". The value of discharge pressure separating these two operation zones is called "critical pressure".
It is worth to mention here, that the term "on design" is not intended as the condition for which the performances of the cycle are optimized. As will be demonstrated at the end of this chapter, the best operating condition in terms of efficiency is the locus of all the critical points at the various operating temperatures. However, being the critical conditions unstable (a small pressure perturbation can lead to the subcritical regime, with substantial decrease in system COP and cooling load), practical functioning of the cycle requires to operate at a certain distance from the critical points, whence the "on design" appellation for the plateau region.

[1] Fig. 1.2 represents also the operating curve of the whole cycle, because the COP is proportional to the ER through eq. 1-1.

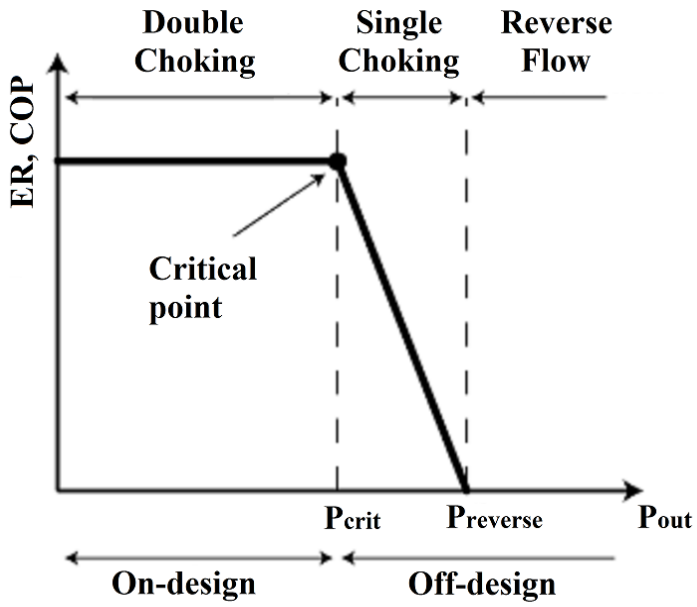

Fig. 1.2 – Typical supersonic ejector operating curve at fixed generator and evaporator P or T

The operating curve of Fig. 1.2 has been obtained at fixed evaporator and generator saturation temperatures. A change in these two temperatures leads to substantial modifications in ER and critical pressure. This is illustrated in Fig. 1.3. When the evaporator temperature increases (i.e., moving from T_{eva-1} towards T_{eva-3} in Fig. 1.3), the higher pressure at suction inlet causes a greater secondary mass flux and, consequently, a greater ER. Higher saturation temperatures of the evaporator lead also to greater critical pressures. This is due to the increase in secondary flow total pressure, which allows the mixed flow to withstand higher backpressures at the condenser. By contrast, when increasing the generator pressure (i.e., moving from T_{gen-1} towards T_{gen-2} in Fig. 1.3, evaporator being set at T_{eva-3}), the rise in primary mass flow rate is generally not followed by a higher entrainment of the secondary stream, whose mass flow rate remains approximately constant, as shown in Fig. 1.4 (this is true only after the secondary flow is chocked, which occurs at a pressure ratio of around 6 in the figure). Consequently, the ER is reduced. Nevertheless, the greater energy content introduced by the motive flow allows reaching higher backpressures, thus moving the critical point toward larger values of condenser pressures.

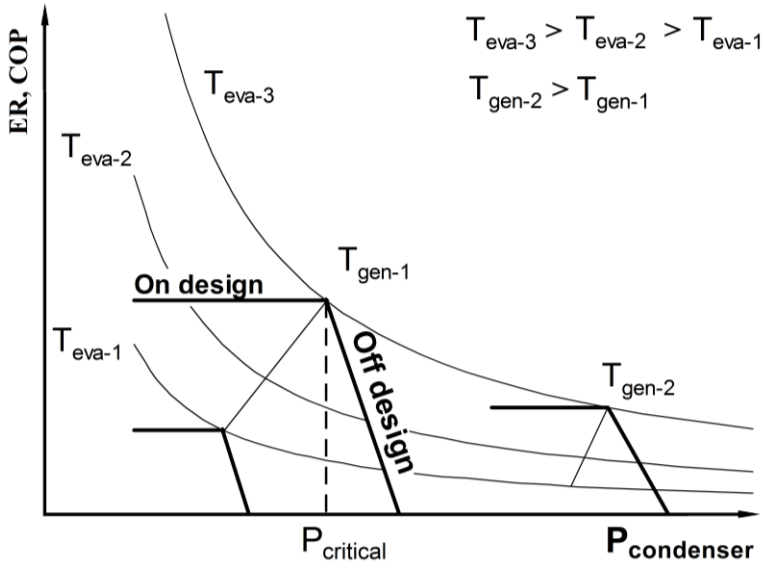

Fig. 1.3 – Typical trend of ejector operating curves as generator and evaporator temperatures are varied.

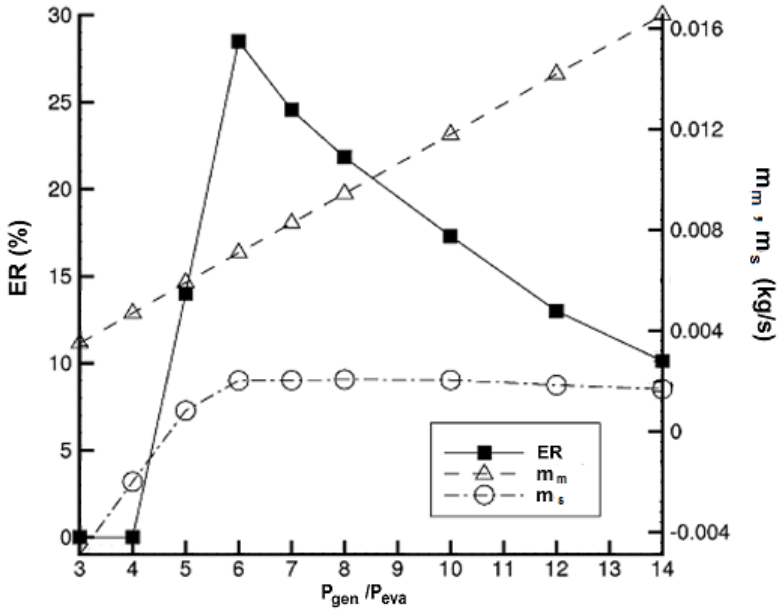

Fig. 1.4 – Mass flow rates and ER variations as the generator pressure increases (the evaporator pressure is only used to do scale the curves and is held constant), adapted from Bartosiewicz *et al.* (2005).

This peculiar behavior can be explained by performing a simple energy balance of the ejector. In the hypothesis that the ejector walls are perfectly adiabatic, the energy equation applied to the ejector system leads to the simple statement that the total enthalpy is conserved:

$$\dot{m}_m H_G + \dot{m}_s H_E = \dot{m}_D H_D \qquad \text{eq. 1-3}$$

where H is the total enthalpy and the subscripts G, E and D stands for *generator*, *evaporator* and *discharge* respectively.

As a consequence, no First Law efficiency can be defined from this balance because energy is completely conserved across the ejector. Nevertheless, after some manipulations, eq. 1-3 can show one of the main characteristic of the ejector.

By limiting the analysis to a single-phase ejector, ideal gas behavior can be assumed and eq. 1-3 simplifies to:

$$\dot{m}_m T_G + \dot{m}_s T_E = \dot{m}_D T_D \qquad \text{eq. 1-4}$$

where T are total temperatures and is assumed that the specific heat does not change much in the range of temperature under consideration.

By further considering negligible superheating at each of the inlets or outlets, the total temperature can be related to the saturation pressure by means of the Clasius-Clapeyron equation (this assumption is particularly crude for the ejector outlet, where the amount of superheat can be considerable). By considering an approximately constant latent heat and that the vapor density is much lower than that of the liquid phase, it can be shown that the Clasius-Clapeyron equation reduces to (Wegener and Mack, 1956):

$$\ln p = -\frac{h_{lv}}{R}\left(\frac{1}{T}\right) + c \qquad \text{eq. 1-5}$$

where h_{lv} is the latent heat of vaporization, R is the specific gas constant and c is a mathematical constant. Solving eq. 1-5 for T and inserting the resulting expression into eq. 1-4 the integration constant c simplifies and the energy equation reads:

$$-\dot{m}_m \frac{h_{lv}}{R \ln p_G} - \dot{m}_s \frac{h_{lv}}{R \ln p_E} = -\dot{m}_D \frac{h_{lv}}{R \ln p_D} \qquad \text{eq. 1-6}$$

By eliminating the constant terms and splitting the discharge mass flow rate into the sum of the evaporator and motive mass flow rates, eq. 1-6 becomes:

$$\dot{m}_m \left(\frac{1}{\ln p_G} - \frac{1}{\ln p_D} \right) = \dot{m}_s \left(\frac{1}{\ln p_D} - \frac{1}{\ln p_E} \right) \qquad \text{eq. 1-7}$$

It is now possible to introduce the ER and, by exploiting the properties of the logarithms, eq. 1-7 can be rearranged as follows:

$$ER = \frac{\ln p_E}{\ln p_G} \left(\ln \frac{p_G}{p_D} \Big/ \ln \frac{p_D}{p_E} \right) \qquad \text{eq. 1-8}$$

This formula connects the pressure levels inside the ejector with the resulting ER.
Moreover, a further simplification is possible by noting that the first term on the RHS it is of the order of unity and does not change much even for big pressure difference between the motive and suction inlets (for P_E=*0.1 bar* and P_G=*10 bar* the ratio is 0.67 while for P_E=*1 bar* and P_G=*10 bar* is 0.83). For clarity, two new symbols are introduced that represent the ratio of the primary to discharge pressure, which is generally called motive ratio, ξ, and the ratio of the discharge pressure to the suction pressure, called the compression ratio, β:

$$ER \approx \frac{\ln \xi}{\ln \beta} \qquad \text{eq. 1-9}$$

where both the motive and compression ratio are generally greater than unity.
This simple and approximated formula illustrates one of the most obvious feature of any ejector, i.e., that ER is proportional to the motive ratio, ξ, and inversely proportional to the compression ratio, β (to their logarithms precisely). Qualitatively speaking, eq. 1-9 shows that given a certain amount of energy of the primary stream, this can either be used to compress a large amount of suction flow to low discharge pressure or, vice versa, to compress the suction stream up to high discharge pressure when low mass flow rate is entrained.
From the above approximate relation, it may appear that any desired level of ER could be reached by simply adjusting the compression ratio accordingly. This is not always true because for fixed motive and evaporator inlet conditions there is a maximum level of ER due to the double-chocking of the ejector. The "black-box" analysis that led to eq. 1-9 overlooks any detail of the ejector internal dynamics and, therefore, it cannot capture the process of ejector chocking.
As mentioned before, the ejector double chocking is also the cause of the COP plateau line in the operating curve (see Fig. 1.2 or Fig. 1.3). It is important to understand that, though the COP is constant,

the efficiency of an operating point along the plateau is lower the farther it is from the critical point. This concept cannot be realized if the performance of the system is assessed only through COP and First Law considerations. There are at least two perspectives from which this performance decrease can be seen. The first and more rigorous requires the introduction of the concepts of Second Law efficiency: an ejector working at a point inside the plateau has equal COP but lower Second Law or exergy efficiency than one working closer the critical pressure. This will be shown in chapter 2.2. The second way is more empirical, and can be demonstrated by showing that, if the system is operated at a state inside the plateau line, there is always the chance to change the operating conditions and move the operating point toward a region of greater COP. This way of reasoning depicts the performance loss as a "lost chance" of working with greater efficiency. This has been well illustrated by Eames *et al.* (1995) and Aphornratana and Eames (1997) and will be detailed below.

Fig. 1.5 shows a classic *COP-*P_{cond} diagram with a set of operating curves at fixed evaporator temperature but different generator temperature. Let's now suppose that the system is operating on a point lying in the plateau of a curve with high generator temperature (point *a*). By ideally changing the generator temperature and keeping the condenser and evaporator temperature fixed, the operating point moves on a vertical line. At first, the point intersects curves with a higher COP that are still in the double-chocking regime (e.g., point *b*). However, the new operating points are closer to the critical pressure and work with a lower generator temperature. The trend is the same until the point reaches the curve that intersects the vertical line right at the critical pressure (point *c*). From this point on, further increases in the generator pressure drive the operating point into the off-design regions of operating curves with higher generator temperatures, with a significant reduction of the system COP (point *d*).

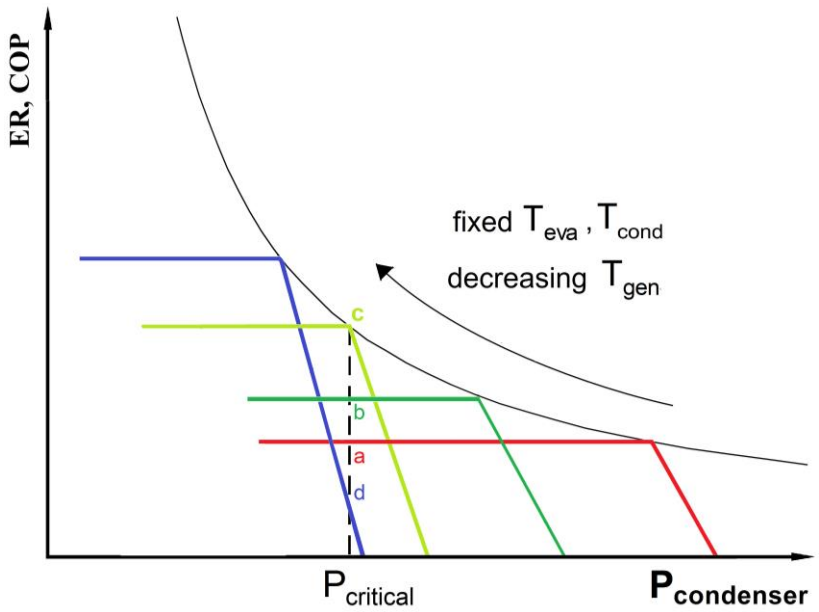

Fig. 1.5 – Operating curves at fixed evaporator temperatures and varying generator temperature

This type of analysis makes clear that whenever the cycle is working at an operating point inside the plateau it is always possible to increase the efficiency of the system by simply reducing the generator temperature. This is an important aspect as it brings about a double beneficial effect: in addition to the efficiency increase, the temperature and "quality" of the energy source are reduced. This effect becomes clear when analyzing the operation of the ejector from the point of view of Second Law analysis (chapter 2.2). It will be shown, that when working at an operating point inside the plateau there is a surplus of energy which is wasted. This surplus can be employed either to decrease the generator temperature and

COP (like just showed) or to increase the condenser temperature in case the ambient temperature gets warmer.
Finally, this way of reasoning is also at the base of the ejector system regulation. Aphornratana and Eames (1997) give a nice explanation about the ways for controlling the system temperatures for optimal operation of the chiller. The control can be aimed at reaching either the maximum COP and cooling load, or the minimum evaporator temperature (all other parameters being equal). Moreover, the authors analyze the use of a moveable primary nozzle as a further way to perform a fine control of the ejector performance. Fig. 1.6 illustrates the impact on the operating curve of a change in the primary nozzle axial position. In particular, the authors found that retracting the nozzle gives the same impact as a decrease in generator temperature, i.e., it produces a rise in the operating curve plateau while it reduces the critical pressure. Therefore, the control and regulation of the plant can be carried out by either changing the operating conditions (in particular the generator temperature) or by adjusting the position of the primary nozzle. This last point is nevertheless a bit controversial because not all the authors have found such a clear correspondence between the effects of NXP and generator temperature variation.

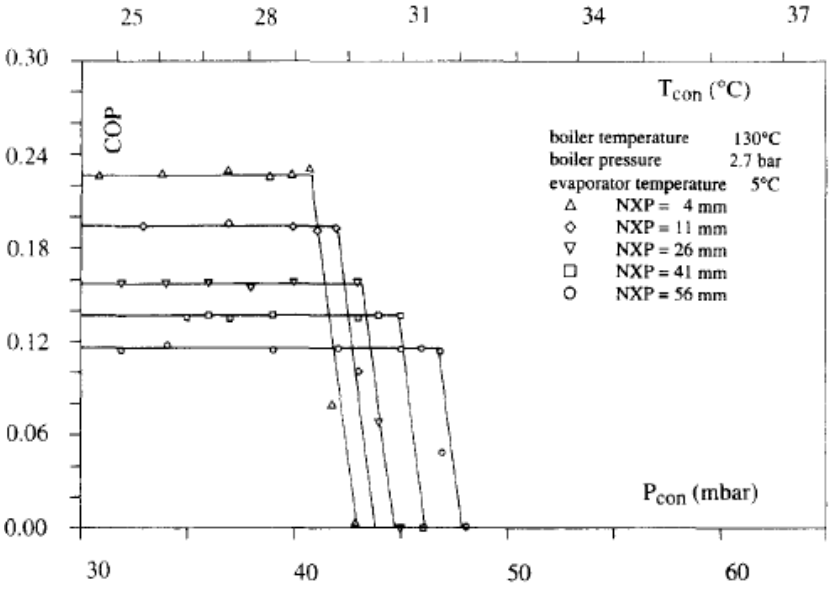

Fig. 1.6 – Trend of operating curves (COP vs. P_{cond}) as the NXP varies (from Aphornratana and Eames (1997))

In conclusion, the above analysis demonstrates that the best performances, for fixed operating conditions, are always achieved at the critical conditions. By joining together all the critical points at the various operating temperatures one obtains the "performance characteristics" or "performance map" of the ejector cycle, whose qualitative shape is shown in Fig. 1.7.
For a clear comparison of data, this type of map should always be provided in any experimental and numerical study on ejector refrigeration.

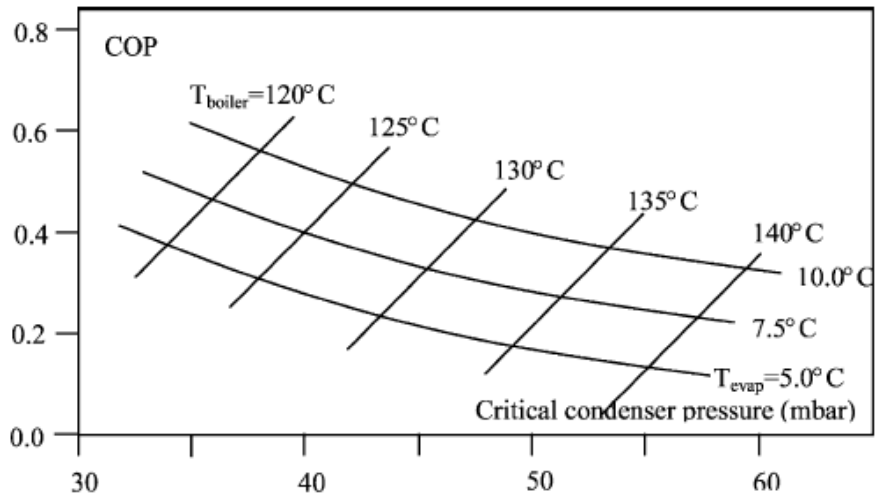

Fig. 1.7 – "Performance characteristics" or "performance map" of the ejector cycle, from Chunnanond and Aphornratana (2004)

1.2 Solar powered and passive cycles

Over the years, a large number of different applications and configuration alternatives to the standard ejector cycle have been proposed. These include the solar powered ejector chiller, passive systems, the multiple-stage ejector cycle, cycles with multiple parallel ejectors, multiple nozzles, annular nozzles, petal nozzles, booster-assisted ejectors and so forth…. Among the others, the two most extensively studied configurations are the passive system and the solar powered ejector refrigerator. These will be briefly illustrated in this chapter; for a complete overview of all the possible solutions, the reader may refer to one of the many review papers on the subject (e.g., Chunnanond and Aphornratana 2004; Abdulateef *et al.*, 2009; Elbel, 2011; Little and Garimella, 2011; Sarkar, 2012; Chen *et al.*, 2013; etc…).

In passive systems configurations, the elimination of the pump makes possible the construction of an off-grid refrigerator. In addition, the absence of any rotary device increases the system reliability and, in some cases, reduces investment and maintenance costs. However, depending on the type of configuration, the passive system may incur in performance penalties that are not entirely negligible.

One of the simplest ways to replace the liquid feed pump is represented by gravitational systems. These were first theoretically investigated by Grazzini and D'Albero (1998) and later by Nguyen *et al.* (2001), who built a solar powered prototype to provide 7kW of cooling to an office building. The scheme of the plant is depicted in Fig. 1.8A. The pump is eliminated by establishing a large gravity head between the condenser and the generator. Using water as the working fluid, the height difference required to produce a suitable pressure gradient is found to be around seven meters.

The system successfully ran at a boiler temperature of 80˚C, varying ambient temperatures, and 1.7˚C evaporator temperature, with a COP of 0.3 (η_{II} maximum ~ 0.21, see later Tab. 2.4). The authors states that from an operating perspective, the system has several advantages over conventional vapor compression refrigeration, including very long life-time, minimal maintenance requirement, low risk of breakdown and no associated noise or vibration. On the other hand, the main drawbacks include low performances, large specific volume of the refrigerant, the necessity to operate at sub-atmospheric pressures and large thermal inertia of the system.

Nguyen *et al.* studied also the economical feasibility of the system. From a cost-benefits analysis they concluded that over a 30-year lifetime, the ejector cooling system is more expensive than an equivalent vapor compression system. The payback time for the ejector cooling system is *33 years* and, consequently, a reduction in capital cost is necessary if commercial viability is to be achieved (Nguyen *et al.*, 2001).

Gravitational systems were also theoretically studied by Kasperski (2009) by means of a simulation model. The analyses conducted by the authors revealed that the main limitation of this system lies in its requirement of great height differences and length of pipe work, which increases friction and heat losses.
In order to limit or eliminate the requirement for height difference, an ejector may be used to substitute the feed-pump. Shen *et al.* (2005) refer to these cycles as the bi-ejector refrigeration systems. In their scheme, presented in Fig. 1.8B, the second ejector is used to feed the generator by exploiting the motive energy of the vapor coming from the generator itself. Rigorously, in this particular application the name "ejector" should be replaced by the more appropriate "injector". Shen *et al.* studied this type of cycles numerically and found that the overall COP of the system is mainly affected by the gas–gas ejector entrainment ratio in the refrigeration loop. Different refrigerants also impact the system performance. Under the same operating conditions, the entrainment ratio of water is high, but the best overall system COP (~0.26) is achieved using ammonia as the refrigerant.
As a curious remark, although this scheme may appear innovative, ejectors (or injectors) have actually been invented to replace the rotary pump feeding the boilers of old train locomotives working with steam engines. Hence, this type of application is actually more than 150 years old! (See chapter 1.4 for more details).

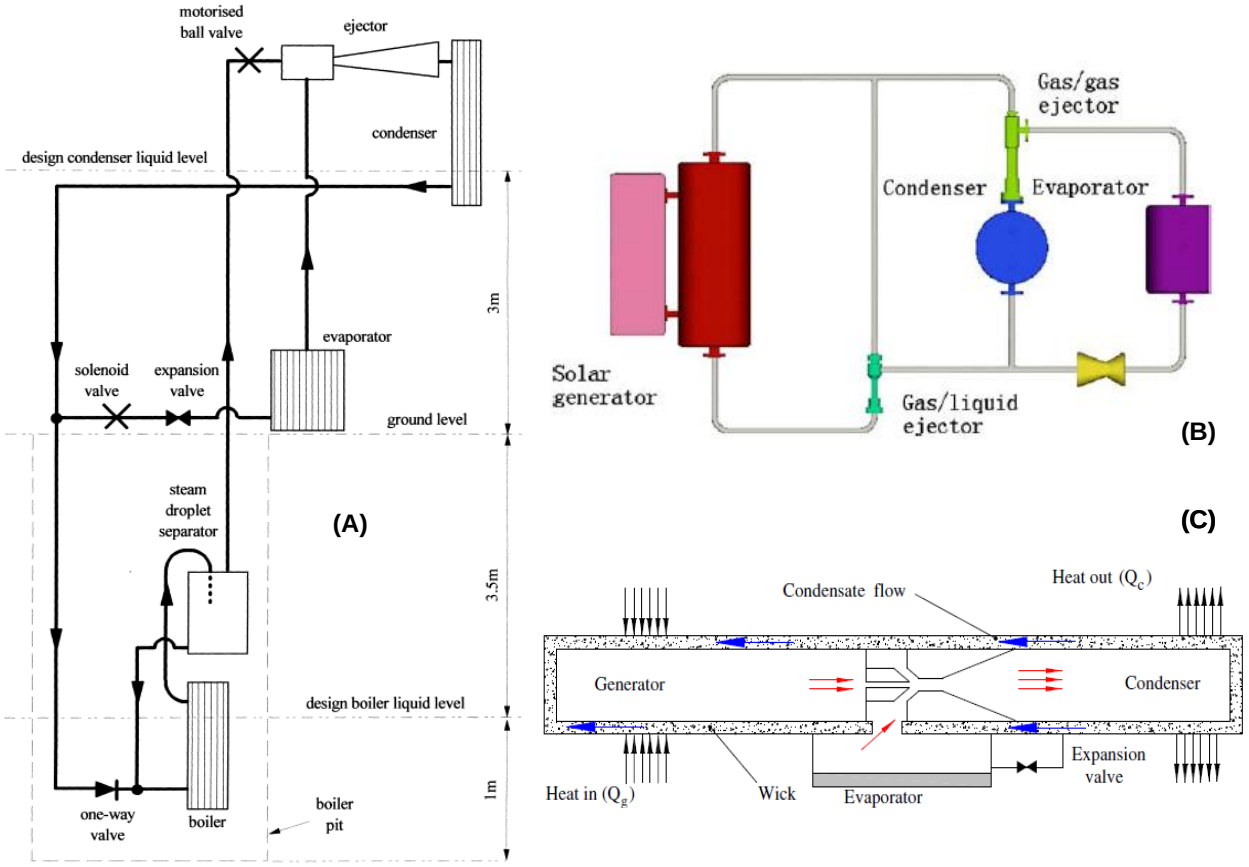

Fig. 1.8 – Passive cycles - (A) scheme of a gravitational ejector chiller, from Nguyen *et al.* (2001); (B) scheme of the bi-ejector refrigeration system from Shen *et al.* (2005); (C) the heat-pipe/ejector refrigeration system from Ziapour and Abbasy (2010).

A subtle problem in all these systems is that some active components are necessarily needed to run the auxiliary circuits (e.g. the cooling and hot water circuits, power controllers and valves). Although these may require small amounts of electrical input, the use of pumps or fans to circulate the external streams and the eventual need of a solar source of electricity (i.e., a solar PV) may nullify the very "raison d'être" of the passive systems. A possible way out would be to project heat exchanger cooled by natural

convection. However, these may result in very large, expensive and not-so-easily controllable components. An example of completely passive system is represented by the heat-pipe/ejector refrigerator.

This type of system have first been devised by Riffat (1996) and later studied by Riffat and Holt (1998) and Ziapour and Abbasy (2010). Integration of the heat pipe with an ejector results in a compact system that can utilize solar energy or waste heat sources. The scheme of the cycle is shown in Fig. 1.8C and consists of a heat pipe coupled with an ejector, evaporator and expansion valve. Heat is added to the generator where the working fluid evaporates and flows through the primary nozzle of the ejector. The flow exiting the nozzle entrains the secondary fluid and decrease the pressure in the evaporator. The mixed fluid is then condensate in the condenser. A part of the condensate is returned to the generator via the capillary tube, while the remainder is sent to the evaporator through the expansion valve.

Ziapour and Abbasy (2010) performed an energy and exergy analysis of the heat pipe/ejector system in order to find the optimum operating conditions. The results showed that COP could reach about *0.3* with a generator temperature of *100°C*, condenser temperature of *30°C* and evaporator temperature of *10°C*. Unfortunately, to date there is no experimental prototype supporting these theoretical results, and some doubts arise about the practical attainability and control of these systems.

Other alternatives to the use of circulation pumps have been explored by Srisastra *et al.* (2008), Srisastra and Aphornratana (2005), Huang *et al.* (2006) and Wang *et al.* (2009). These systems try to replace the mechanical feed pump by means of particular configuration of storage tank and set of valves that work with a cyclic process. Although, these systems require little external electrical or mechanical energy input, the efficiency is generally very low (Little and Garimella 2016).

Low efficiencies represent a limit also for solar powered ejector systems, whose performances are affected by both the efficiency of the refrigeration system itself and that of the solar collectors. Chunnanond and Aphornratana (2004) and Abdulateef *et al.* (2009) give nice overviews of this topic, and the following analysis largely builds on these two references.

The overall COP of the solar jet refrigeration cycle can be approximately expressed as (Chunnanond and Aphornratana 2004):

$$COP_{overall} = \eta_{solar\_panel} \cdot COP_{ejector\_chiller} \qquad \textbf{eq. 1-10}$$

This shows that the performance and cooling capacity of the solar powered system depends strongly on the type of solar collector. When the generator of the refrigeration system is operated at a temperature between *80* and *100°C*, a single glazed flat plate type collector with a selective surface is recommended, while the vacuum tube or parabolic solar concentrating collectors can provide higher operating temperature when required (Chunnanond and Aphornratana, 2004). Although the installation of these type of high-efficiency collectors may result in increase in the overall efficiency, a careful economic analysis is needed to understand whether the relatively higher costs are worth the efficiency gains (Zhang and Shen, 2002; Huang *et al.*, 2001; Nguyen *et al.*, 2001).

In the simplest configuration, the solar collector acts as the generator of the refrigeration system. However, this configuration poses some problems in terms of pump sizing and regulation because the solar collector and refrigerator circuits may require different flow rates and operating pressures (the control of the optimal flow rate and boiler pressure becomes difficult with a single pump, Al-Khalidy, 1997). In order to eliminate this restriction, the solar and refrigeration systems are usually separated. Fig. 1.9 shows both the integrated and separated configurations. In the separated configuration, the fluid circulating in the solar collector should have significant heat transfer properties, as well as a boiling point higher than the possible temperature occurring in the system (Chunnanond and Aphornratana 2004).

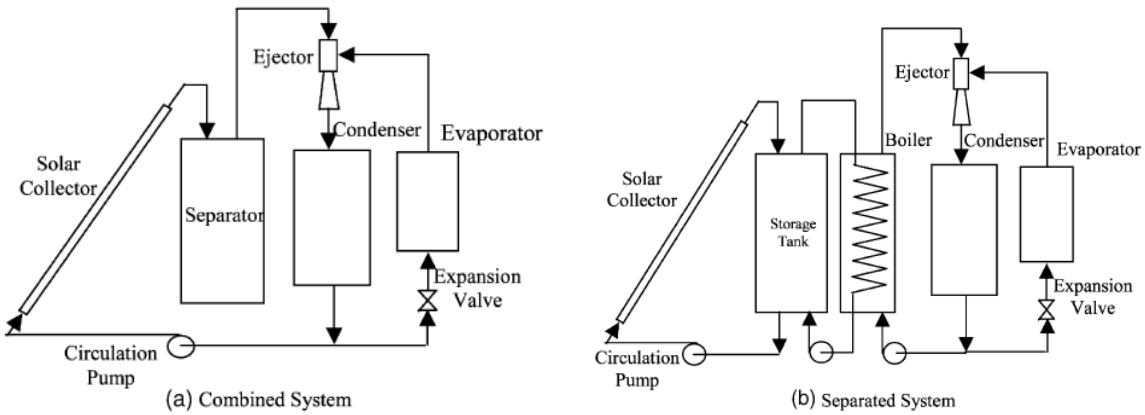

Fig. 1.9 – Solar powered ejector cycles. Left side: combined configuration. Right side: separated configuration (from Chunnanond and Aphornratana, 2004).

Many research groups worldwide have performed theoretical calculation, computer simulation and experimental work on solar powered ejector chillers (Abdulateef *et al.*, 2009).

One of the main technical problems of this type of configuration is to keep the system running at optimum performance under variable working conditions (Abdulateef *et al.*, 2009). In addition to seasonal and daily ambient temperature fluctuations (that impact condenser temperatures and pressures), the system is subject to variation in solar radiation that imply an unstable heat source. Thermal storage systems integrated with solar-driven ejector chillers allows reduction of thermal fluctuation and is thus becoming a hot research topic (Chen *et al.*, 2013). Attempts have also been made to solve this problem by combining ejectors with other types of refrigeration cycles (see next chapter) or by trying more sophisticated cycle configurations. For instance, some authors (Bejan et al, 1995; Sokolov and Hershgal, 1990) introduced the idea of multiple ejectors (improperly called multi-stage ejector chiller), where two or more ejectors are placed in parallel before the condenser. In this type of cycle, shown in Fig. 1.10, each ejector is designed to optimally run with different operating temperatures (e.g. summer/winter conditions). The activation of one ejector or another is generally determined by the condenser pressure. In practice, this type of configuration exploits the concept of variable geometry to optimize the performance of the system, without actually realizing a variable geometry ejector. However, the costs of the additional ejectors may preclude the economic viability of this solution.

In conclusion, due to the low efficiency when working under severe operating conditions, the solar powered ejector chiller seem to be more suitable for air-conditioning purposes rather than refrigeration applications (Chunnanond and Aphornratana, 2004; Prisadawas, 2006). However, the competition with other, more efficient systems (i.e. PV combined with conventional vapor compression system, solar powered absorption chillers) still prevents the industrial commercialization of ejector chillers even in this specific market.

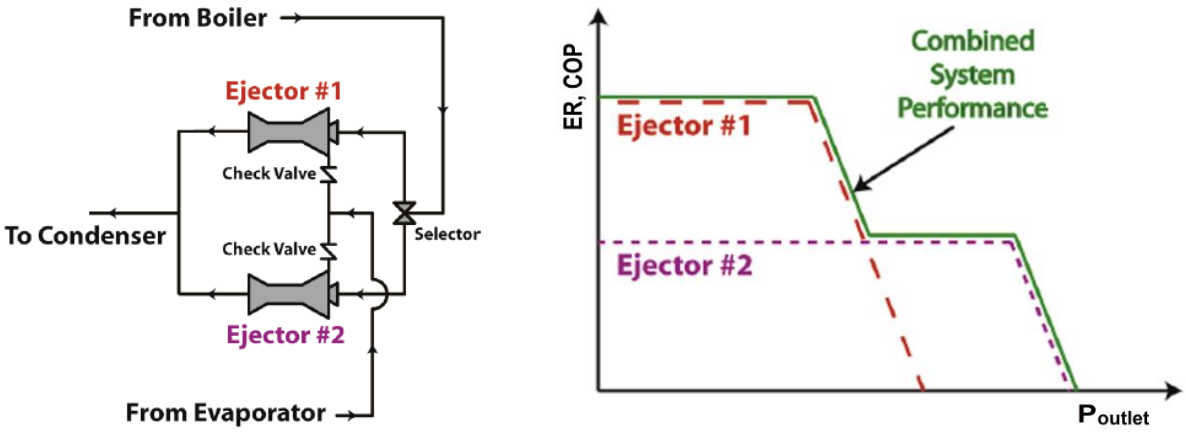

Fig. 1.10 – Multi-stage parallel ejector system and the corresponding aggregate operating curve. The ejector #1 is suited for winter operations, while ejector #2 for summer conditions (from Little and Garimella, 2011)

1.3 Combined cycles

The previous chapters were focused on the analysis of supersonic ejector cycles and their various configurations. In what follows, it will be briefly shown how supersonic ejectors can be profitably used to improve the performance of various types of conventional refrigeration systems.

A great variety of different hybrid cycles can be found in the literature, from combined vapor compression/ejector systems to absorption or adsorption-ejector refrigerators. Among the various alternatives, the most promising solutions in terms of practical attainability and potential performance increase seem to be the enhancement of standard vapor compression and absorption cycles. In these types of applications, the ejector is used to recover the throttling loss inside any of the expansion valves present in the cycle. This allows appreciable efficiency increases without requiring significant modifications of the cycle configuration.

The theme of throttling loss recovery in refrigeration plants has been extensively studied for a long time. In the case of standard vapor compression refrigerators, it could be demonstrated that the energy loss is particularly significant in chillers with a large gap between the condensation and evaporation temperature or when the condensation temperature is close to or higher than the refrigerant critical temperature (Brasz, 2003).

A large number of different systems for the throttling loss recovery have been proposed over the years: micro turbines, screw expanders, scroll expander, reciprocating engines etc… However, due to the difficulties in the realization of ad-hoc, reliable, two-phase flow devices, in most cases the costs of the new solution is greater than the efficiency gain. In this context, the use of ejector is particularly advantageous, as its operation and design are inherently robust with respect to two-phase flow (e.g., limited or absent problem of erosions).

Fig. 1.11 shows a scheme of the Ejector Expansion Cycle along with a *p-h* diagram showing the various transformation of the cycle. The operation is simple: the ejector receives high pressure liquid coming from the condenser; the liquid expands inside a convergent-divergent nozzle down to state (4), following an (ideally) isentropic transformation. Inside the nozzle, the liquid refrigerant undergoes phase change and enters the mixing chamber as a vapor-liquid mixture with relatively low quality. Inside the mixing chamber, the primary flow entrains and accelerates the saturated vapor coming from the evaporator (state 9-5). The two streams mix and then are recompressed along the ejector diffuser (6-7). The flow coming out from the ejector is a high-quality mixture of vapor and liquid. This enters the separator where the vapor is divided from the liquid, sent to the compressor (1) and then back to the gas cooler/condenser.

The remaining liquid passes through a metering valve that reduces its pressure down to the evaporator level (8-8a).
Due to the small pressure gap between the separator and evaporator (P8-P8a), the throttling loss of the combined chiller is much lower than in conventional cycles. The advantage of this type of configuration, which is sometimes called the "Ejector Expansion Cycle", comes from the fact that the energy recovered from the liquid is spent to compress the vapor coming from the evaporator, thus reducing the pressure ratio and work of the compressor. The scheme of Fig. 1.11 is just one among many other possible alternatives. One of these replaces the separator by a further evaporator, working at a higher temperature. The scheme of this configuration is presented in Fig. 1.12 below.

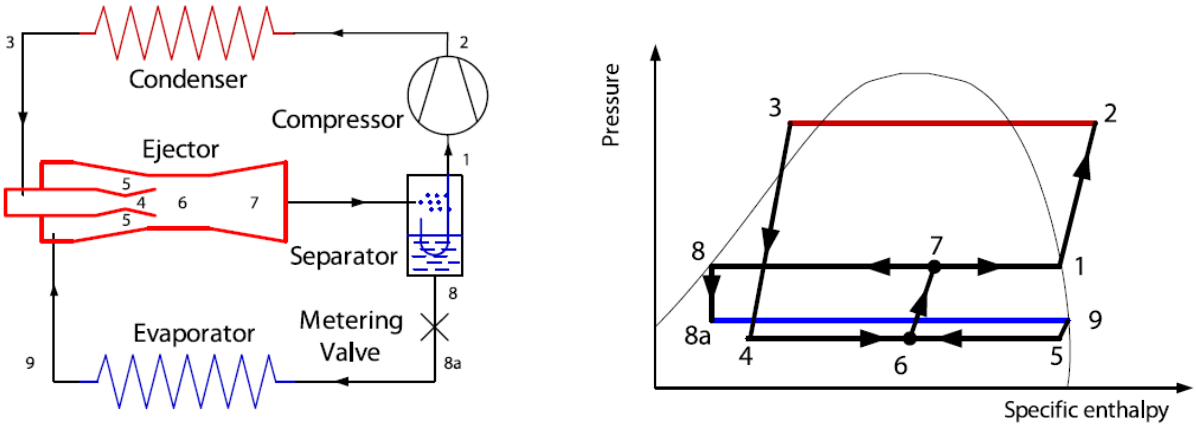

Fig. 1.11 –A simplified scheme of the cycle with the corresponding *p-h* diagram (from Lawrence and Elbel 2013).

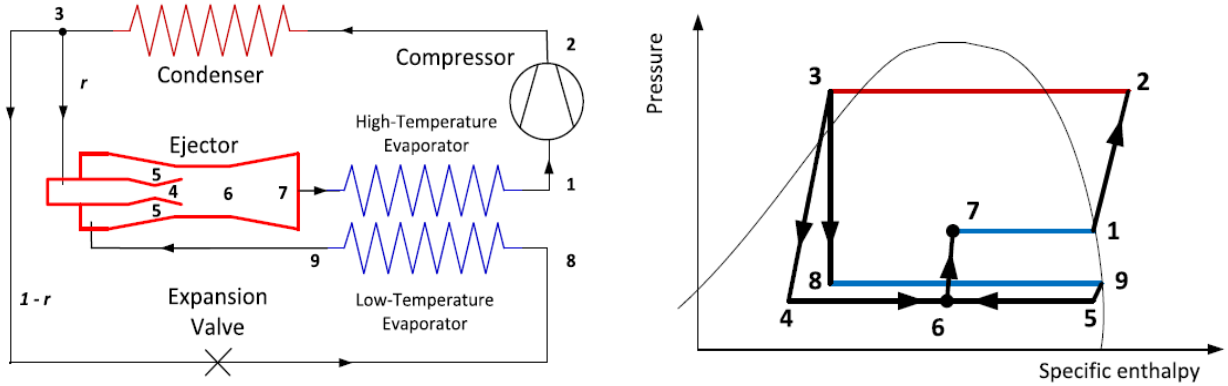

Fig. 1.12 – A scheme and *p-h* diagram of the "Ejector Expansion Cycle" with two evaporators (from Lawrence and Elbel, 2013).

From the point of view of cycle efficiency, it could be demonstrated that the two configurations are entirely equivalent in terms of COP (Lawrence and Elbel, 2013). Nevertheless, the presence of two evaporators may allow for greater exchange efficiency in cases where there is a large temperature excursion of the fluid to be cooled. In addition, this configuration offers the possibility of two separate levels of cold temperatures.
Most notably, this scheme has been adopted and realized by DENSO Corporation for the air conditioning of Toyota PRIUS (Takeuchi, 2009). In order to reduce space, the ejector has been inserted directly within the fluid collector of evaporator, which is of the micro-channel type. Fig. 2.4 shows the scheme and detail of this innovative application. Other possible configurations of combined vapor compression/ejector chiller can be found in Lawrence and Elbel (2013), Bergander (2006) and Disawas and Wongwises (2004).

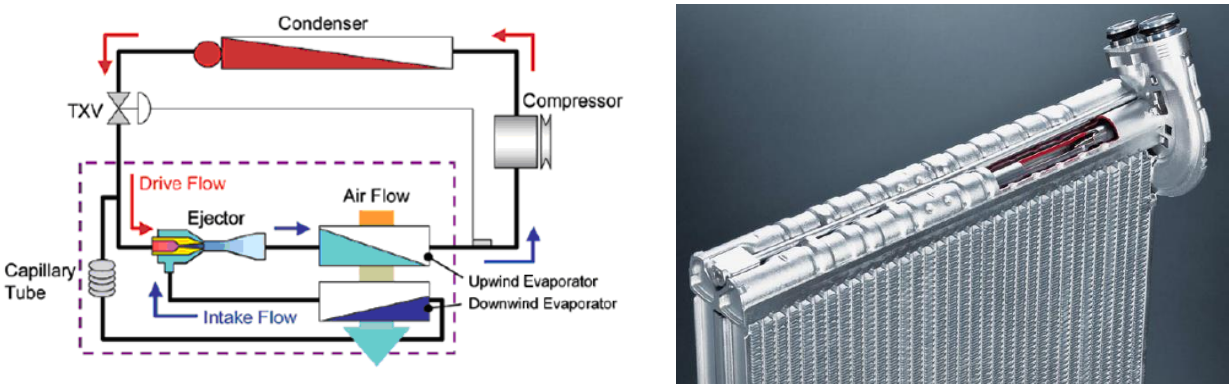

Fig. 1.13 – Left side: scheme of the Denso refrigerator. Right side: a detail of the micro-channel evaporator with integrated ejector.

A further way through which supersonic ejectors can be profitably used is the enhancement of absorption chillers. In a conventional absorption refrigerator there exist two distinct pressure levels. Two valves are commonly employed to separate the high pressure side, consisting of the generator and condenser, from the low-pressure side, made up by the evaporator and absorber. Both valves operate on a throttle process causing inefficiency in the system (Abdulateef *et al.*, 2009). Hence, the ejector can be used to recover the throttling losses from either the weak solution coming from the generator, or the saturated liquid coming from the condenser. In many cases, the improved configuration can lead to COP values close to that of a typical double effect absorption cycle machine (Chunnanond and Aphornratana, 2004). Moreover, the hybrid ejector-absorption refrigeration machine features a relatively simple scheme that requires less investment costs with respect to other conventional, high-performance absorption systems.

Many different schemes have been proposed in order to combine the ejector to the absorption cycle. One possible configuration, adopted by many researchers, consists of using the ejector to raise the absorber pressure, thus reducing the solution concentration. Chung *et al.* (1984) and Chen (1998) investigated this configuration by using the high-pressure liquid solution returned from the generator as the ejector's motive fluid. The scheme is illustrated in Fig. 1.14. Experimental investigation showed that the use of the ejector allowed a pressure ratio of around 1.2 across the absorber and evaporator. The higher absorber pressure resulted in a lower solution mass flow rate, thus reducing the pump work.

Sözen and Özalp (2005) proposed a similar scheme, operated with aqua-ammonia and powered by solar collectors. The authors investigated the possibility of using this system in Turkey. As a result, the COP improved by about 20% using the ejector (Abdulateef *et al.*, 2009).

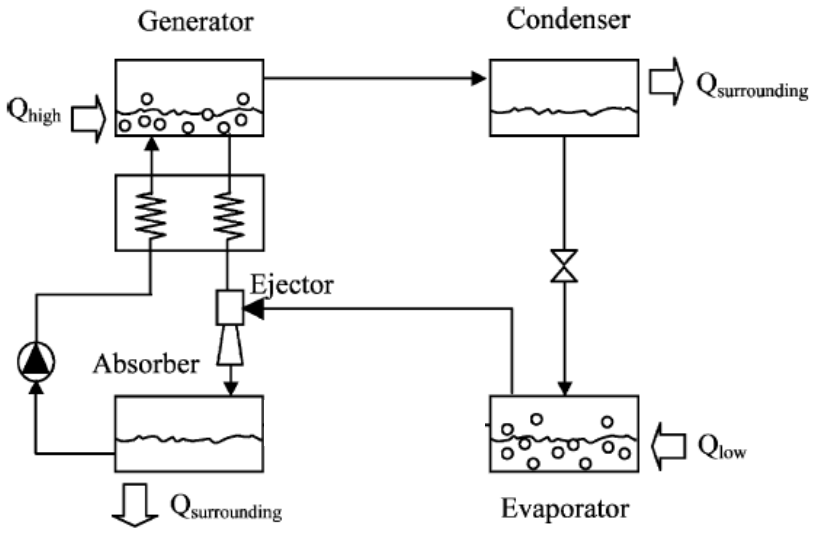

Fig. 1.14 – Scheme of the absorption/ejector refrigerator with throttling loss recovery from the weak solution (from Chunnanond and Aphornratana, 2004).

An alternative scheme, proposed by Aphornratana and Eames (1998), is shown in Fig. 1.15. The ejector uses high pressure vapor from the generator to entrain the gaseous refrigerant from the evaporator. This is deviated back to the condenser thereby increasing the mass flow rate of refrigerant that accomplishes the cooling cycle. Hence, COP should increase with respect to the conventional system and experimental investigation showed that COP of 0.86–1.04 could be achieved (Chunnanond and Aphornratana 2004).
Although this system may have an increased COP, the losses introduced by the ejector may penalize the maximum achievable condenser temperature. As a matter of fact, no throttling losses are recovered in this type of configuration, raising some doubts on the claimed performance benefits. To remove all doubts, a Second Law analysis should be performed to understand whether the COP improvements are worth the additional pressure losses (see chapter 2.2). Moreover, a further drawback of this system is that the generator must be operated at very high temperature (190–210 °C) leading to possible corrosion of the materials (Chunnanond and Aphornratana, 2004).

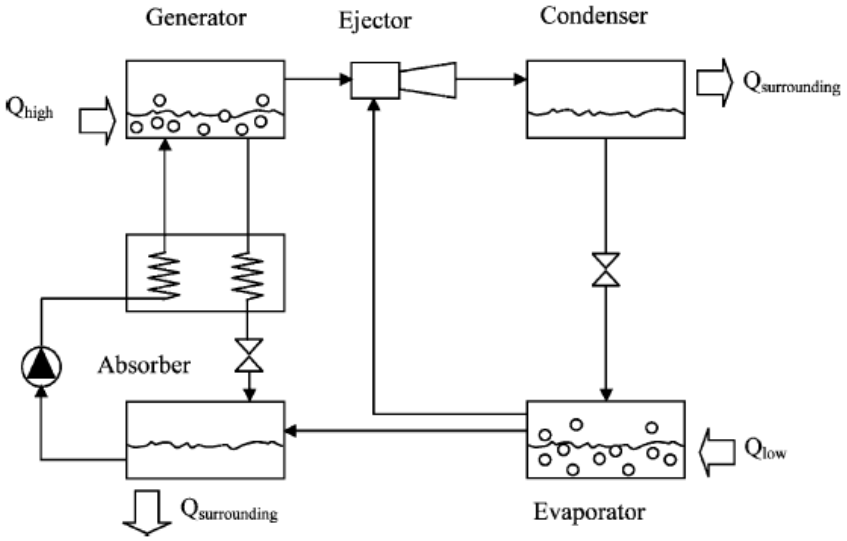

Fig. 1.15 – Scheme of the absorption/ejector refrigerator with motive flow coming from the generator (from Chunnanond and Aphornratana, 2004).

Finally, ejectors can also be used in combination with adsorption refrigerators in order to overcome the intermittent operation of these systems. Li and Wang (2002) investigated a solar-powered configuration using Zeolite 13X-water as the pair. The cycle consisted of two sub-systems: the ejector sub-system to provide refrigeration during the day and the adsorption sub-system which refrigerates at night-time. A COP of 0.4 was achieved with 9°C evaporating temperature, 40 °C condensing temperature, 120 °C regenerating temperature and 200 °C desorbing temperature (Chen *et al.* 2013). More details can be found in (Li and Wang, 2002).

1.4 Historical background

The historical path of ejector refrigeration is tightly nestled in the broader history of refrigeration. This has seen his birth and flourishing all the way in the era of Positivism, during the second half of the nineteenth century. In this chapter we give a brief account of the historical steps that laid out the basis for the use of supersonic ejectors in refrigeration applications. More details on the history of refrigeration can be found in books like those of Kneass (1910), Thevenot (1979) or Arora (2003). Below, a non exhaustive timeline is presented in order to give a bird-eye-view of the most relevant historical events up to the first half of the last century (dates in bold refer to events that are specifically relevant to ejector refrigeration).

1755 – Professor William Cullen at the University of Edinburgh builds the first evaporator by connecting a vacuum pump that constantly kept a reservoir of ether at the saturation pressure
1780 – U. F. Clouet and G. Monge demonstrates the process of condensation by liquefying a stream of SO_2
1797 – Giovanni B. Venturi describes the "Venturi effect" which relates pressure and velocity variations of a fluid flowing through an orifice or a variable area channel
1805 – Oliver Evans envisions the first closed refrigeration cycle to produce ice by ether under vacuum
1834 – Jacob Perkins designs the first vapor compression refrigeration cycle
1848 – John Gorrie Patents the first air cycle cooling machine
1856 – James Harrison takes a patent for the first practical vapor compression system using ether, alcohol or ammonia
1858 – Henri J. Giffard invents the first steam/water injector to pump a continuous stream of water into boilers feeding the engines of steam locomotives
1860 – Ferdinand Carre invents the water/ammonia absorption system
1869 – An Engineer named Schau discovers the advantage of the convergent/divergent nozzle for uses in steam injectors
1869 – Ernst Koerting devises and patents a double tube injector that improves the Giffard invention in terms of mass flow rate regulation
1876 – E. Koerting and L. Schutte form the "Schutte & Koerting" company
1878 – Windhausen conceives an absorption refrigerator that works on H_2SO_4 and water (later on the sulphuric acid will be replaced by Lithium Bromide, to form the renowned LiBr-water absorption system)
1888 – Gustaf De Laval applies the converging/diverging nozzle (later named the "De Laval" nozzle) to steam turbines and greatly improves the rotary speed and efficiency
1901 – Sir Charles Parsons use supersonic ejectors for removing air from a steam engine's condenser.
1903 – Aurel B. Stodola demonstrates experimentally the existence of supersonic flow inside a De Laval nozzle, by measuring the axial pressure profile at various discharge pressures
1908/10 – Maurice Leblanc invents the "steam jet refrigeration cycle"
1909 – Westinghouse realizes the first commercial system of steam jet refrigerator based on Leblanc's design

1911 – General Electric Company introduces the first domestic refrigerator: a vapor compression system whit sulphur dioxide as refrigerant, open type compressors and water-cooled condensers
1926 – The French engineer Follain improved the steam jet cycle by introducing multiple stages of vaporization and condensation of the suction steam
1931 – Norman H. Gay patents a cycle in which a two-phase ejector is used to improve the performance of refrigeration systems by partly recovering the throttling losses of the expansion valve.
1931 – Thomas Midgley brings out Freon-12 and starts the era of the "wonder gases", the CFCs
1940/50 – Joseph H. Keenan and his collaborators develop the first practical theory for the mixing inside a supersonic ejector, assuming either constant pressure or constant section mixing chambers.

The invention of steam ejector (or injector) dates back to the first half of the nineteenth century. Kneass (1910) mentions that a crude ejecting apparatus had been used as early as 1570 by Vitrio and Philebert de Lorme. However, the first device that bears any similarity to the operation of the injector was patented in 1818 by Mannoury de Dectot, who applied his invention for raising water and for propelling boats. Later on, in 1838 the Frenchman industrialist and physician Pierre Pelletan was granted a patent for the compression of water vapor by means of a jet of motive steam. However, all these devices and the theory behind them were still at an early stage of development. The merits of having clarified the importance and underlying principles of steam injectors is to be fully granted to Henri J. Giffard who thoroughly worked out the theoretical, operational and design aspects since 1850, eight years before his patent in 1858 (Kneass, 1910).
The first use of a steam ejector or injector was in train transportation to pump feedwater into the locomotive boiler to produce steam for the engine. At that time, pumps were neither efficient nor reliable machines and required mechanical power from the engine itself for starting and operation. This inevitably put forth some problems at train start-up. In this context, the Giffard invention presented considerable advantages. The steam injector was alimented by part of the vapor coming from the boiler. This obviated the problem of pump start-up, as steam was available from the boiler even prior than engine start. Moreover, after mixing with the liquid feedwater, the steam would condensate, preheat the water and return to the boiler. This allowed great benefits in terms of efficiency, as no heat and vapor were wasted.
In the following years, considerable efforts were made in order to optimize the injector in terms of efficiency and control. A large number of design alternatives were proposed (see Kneass1910 for details). Most notably, in 1869 Ernst Koerting devised a double tube injector that largely improved the Giffard invention in terms of mass flow rate regulation (he then founded with L. Schutte the "Schutte & Koerting" company that still today manufactures ejectors for several types of applications). In the same year, an engineer named Schau empirically discovered the advantage of the convergent/divergent nozzle which allowed for greater expansion ratios (though at that time, the principles of supersonic flow were still to be understood).
Thanks to all these developments the use of injector became soon very popular, to such an extent that in 1910 Kneass wrote in his book:

It need hardly be said that the Injector is the most popular boiler feeder now in use. There is scarcely a locomotive in the world that is not equipped with one or two Injectors. Compact, reliable and economical, it still deserves the high encomium bestowed upon it in 1859, by M. Ch. Combes, Inspector General and Director L'Ecole des Mines, — "It is without doubt better than all devices hitherto used for feeding boilers, and the best that can be employed, as it is the simplest and most ingenious."

Despite all these merits, the fortunes of injectors in train transportation were doomed to came to an end when advances in the metallurgical industries, as well as in engineering concepts, allowed the design of more efficient reciprocating and turbo-machineries that supplanted the simple but inefficient steam injector.

Nevertheless, at the same time that Kneass wrote his book, the use of ejector for refrigeration applications was being conceptualized. Around 1900, Charles Parsons studied the possibility of reduction of pressure by the entrainment effect from a steam jet. However, he did not envision the possibility of exploiting the effect for refrigeration uses. Some years later, between 1907-08, the French engineer and industrialist Maurice Leblanc invented the first steam jet refrigeration system. Only one year later, the first commercial system was produced by Westinghouse in Paris, based on Leblanc's design.

When the steam jet chiller first appeared, many different refrigeration cycles had already been devised and perfected: in 1848 the doctor John Gorrie patented an air compression refrigeration machine to provide cold and air conditioning to his malaria patients (Gladstone, 1998); in 1856 James Harrison was granted a patent for the first practical vapor compression system, while two years later Ferdinand Carre invented the water/ammonia absorption refrigerator.

All these devices had already been used for many years for both refrigeration and air conditioning purposes. Despite the presence of so many competitors, the steam jet refrigerator had the advantage that it could run using exhaust steam from any source (steam engines, industrial or chemical processes, etc…). Therefore, from 1910, steam jet refrigeration systems found diffusion mainly in breweries, chemical factories and warships. Later on, during the early 1930s, the system experienced a further wave of popularity (especially in USA) for air conditioning of large buildings such as factories, cinema theatres, ships and railway wagons (Stoecker 1958, Arora 2003). Several companies such as Westinghouse, Ingersoll Rand and Carrier started commercial production of these refrigerators from 1930. In the same year, an engineer named Norman Gay devised a further interesting application for the use of supersonic ejector for refrigeration. Gay patented the enhancement to standard compression cycle working with CO_2 in which the expansion valve is substituted by a supersonic ejector, i.e., the Ejector Expansion Cycle (Elbel, 2011). Fig. 1.16 shows the original scheme, as proposed by Gay.

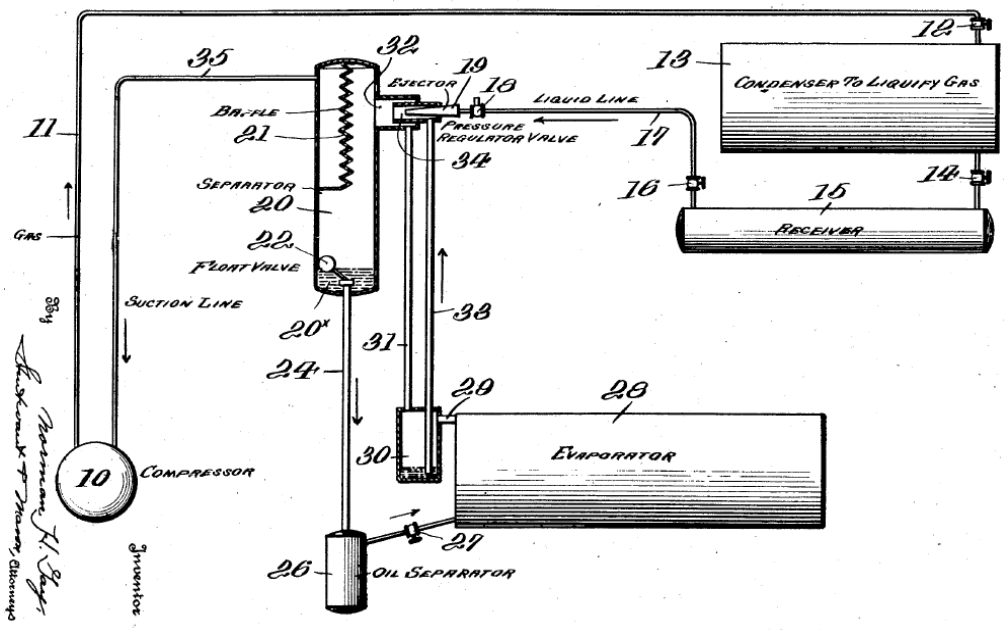

Fig. 1.16 –The original scheme of the "Ejector Expansion Cycle" as proposed by Gay (1931)

Despite the promising start, the use of supersonic ejectors for refrigeration applications came rapidly to an end when Thomas Midgley Jr. and his associates brought to light the first synthetic refrigerants during the '30s. These gases could completely overcome the problems of previous refrigerants that hampered the large-scale commercialization of vapor compression systems. These earlier refrigerants were mainly CO_2, ammonia, ether and sulphuric acid which suffered either of problems of high operating pressure or safety issues such as flammability and toxicity (see Arora 2003 for details). The use of CFCs, and in particular of Freon, allowed construction of efficient reciprocating and rotary compressors. Moreover, the diffusion of synthetic fluids supplanted the use of CO_2 in compression systems due to their moderate operating pressures. In this way, losses in the expansion valve were considerably reduced thus making the use of supersonic ejectors for throttling loss recovery worthless. Similarly, the steam jet cycles were gradually replaced by more efficient vapor compression and vapor absorption systems (although, some east European countries such as Czechoslovakia and Russia manufactured these systems as late as 1960s, Arora, 2003).

Nevertheless, the research on supersonic ejectors did not stop. During the first half of the 20th century huge theoretical progress were made in the understanding of the principle of aerodynamics and the nature of compressible flows. The developments were mostly pioneered by scientists like Ernst Mach, Ludwig Prandtl and its dynasty of brilliant students: Theodore Von Karman, Theodore Meyer, Adolf Busemann, Hermann Schlichting, Walter Tollmien and many others.

In the 1950s, the growing nuclear industry took an interest in ejectors for emergency cooling systems in nuclear reactors. As a result, much research on ejector flow phenomena started (Little and Garimella, 2011). By the end of the '50s, Joseph Keenan and his colleagues at MIT had perfected the theory of mixing inside supersonic ejectors. This exploited the principle of 1D gas dynamics to model a supersonic ejector with either constant area or constant pressure mixing chamber (Keenan and Neumann, 1942; Keenan *et al.*, 1950). Many design concepts has been developed since then and systematic experimental activities had been performed in order to find optimal system designs.

1.5 Future perspectives

Despite the unfortunate fate in refrigeration applications, the diffusion of supersonic ejectors did not slow down. Due to their simplicity and robustness, ejectors found widespread use in many other fields like the pumping, compression and vacuuming of "complex" fluids, such as chemicals and "dirty" suspensions (Power, 2005), or in rocket and aerospace propulsion (Papamoschou, 1993; Alperin and Wu, 1983, Bartosiewicz *et al*., 2005). Unfortunately, developments and refinements of jet refrigeration systems have been almost at a standstill up to these days, due to the market supremacy of vapor compression systems using artificial gases.

However, during the '70s, the oil crisis following the Yom Kippur War in 1973 and the raise up of ozone depletion problem in 1974, laid out the groundwork for a rediscovery of ejector systems. These two events, in conjunction with the increase in refrigeration demand and the appearance of stringent regulations on ozone depletion and global warming (Montreal and Kyoto Protocol in 1987 and 1992 respectively), has prompted the research toward new, economical and environmentally safe technologies. As a result, the supersonic ejector technology has experienced a renovated interest and a great number of research centers worldwide are taking on studies in this field (many of which in the Middle-East, China and India). Despite so, currently the market is still dominated by conventional systems and the future perspectives of ejector refrigeration are quite difficult to foresee.

To date, the use of supersonic ejectors to enhance conventional cycle's efficiency seem to be the solution most likely to catch on. In particular, the integration of ejectors in absorption system seems to produce significant results without requiring too heavy modifications to the cycle. However, to the author's knowledge, there are no real attempts of commercialization yet.

As for Ejector Expansion Cycles, the emergence of this technology seems to be mostly tied on future regulations about environmentally-safe refrigerants. The use of synthetic refrigerants in standard compression cycles allows very moderate losses in the expansion valve and high cycle efficiency. Hence, the insertion of additional components to increase the system efficiency does not seem to be worth the additional expenses and complications. The possible issue of more restrictive international regulations can encourage the production of CO_2 vapor compression cycles, whose efficiency can be greatly ameliorated by the integration with supersonic ejectors.

By contrast, the future of standard supersonic ejector cycles seems to be even more uncertain. The activity performed by our research group on the DIEF plant (see chapter 2.1) suggests that ejector refrigerators can be easily operated and manufactured with low-cost, off-the-shelf components (apart from the ejector itself which represents a small fraction of the total costs). However, the weak point of this type of system is still represented by the low thermodynamic efficiency. This is particularly true for the passive and solar powered configurations.

Within this context, the use of solar energy to power ejector cycle must be carefully evaluated. In a recent review, Kim and Infante Ferreira (2014) make a comparison between solar thermal, solar electric and new emerging technologies both in terms of thermodynamic performances and economic feasibility. The results show that at present the cheapest solution is represented by the PV panels coupled with commercial vapor compression chiller. This result is largely due to the recent dramatic decrease in PV cost and to the large production volumes that make vapor compression chillers very inexpensive (Milazzo and Mazzelli, 2016).

However, solar thermal collectors have also seen a significant decrease of their cost, mainly due to the large amount of collectors manufactured and installed in China. In particular, evacuated tube collectors, thanks to their reduced heat loss towards the environment, perform better at relatively high temperatures and have reached a high market share. These could be profitably adopted to power heat driven refrigerators.

Once the solar thermal option is selected, heat powered cooling may be obtained through various operating principles and cycles. In particular, the main competitor with respect to ejector system is the absorption refrigeration. This technology is by far the most established and competitive technology, due to its high efficiency and long time practice: the first attempts to run vapor absorption systems by solar energy dates back to the first years of 1950s. During the oil crisis of the 1960s several systems were built in many parts of the world for air conditioning purposes and by 1976, there were about 500 solar absorption systems in USA alone (Arora, 2003).

Despite the long tradition and high performance of absorption chillers, ejector refrigeration could offer an effective alternative in all cases where simplicity, reliability and low investment costs are required. Compared with lithium-bromide/water absorption refrigerators, ejector cycles require fewer heat exchangers and do not suffer from problems of internal corrosion and crystallization of the solution (Srikhirin *et al.*, 2001). Ammonia/water absorption refrigerators, on the other hand, use a toxic fluid, while ejector chillers present no restrictions on the use of refrigerants and non-toxic, non flammable and environmentally safe options may be found (e.g. water). These advantages potentially offer significant savings due to lower capital and life-cycle maintenance costs. Hence, under a long term perspective, it could be worth to concentrate some research effort on systems that, though more expensive at current prices, are still at an early stage of development and may benefit from both the "experience curve effects" and scale production costs abatement.

At the very beginning of this chapter it was stated that the use of ejectors in refrigeration applications discloses promising alternatives to standard vapor compression and absorption cycles. Here we clarify that ejector refrigeration seems promising in the way it represents a valuable alternative in specific kinds of market. One of these markets may be that of developing countries, where there is limited or no access

to electric power as well as a lack of technical expertise for the maintenance and reparation of standard compression cycle (in particular, the gas compressor).
Therefore, ejector refrigeration may have more than a chance of playing a role in the wide and increasing market of industrial refrigeration, provided that favorable legislations (i.e. restrictions on synthetic fluids) and adequate commercial strategies will emerge in the international scenario.

2. Analysis and optimization

The analysis of chapter 1 has shown how the major bottleneck that prevents the industrial diffusion of ejector cycles, and especially of the standard configuration, is represented by the low thermodynamic efficiency of these systems. Although losses may be partly due to heat transfer irreversibility inside the three heat exchangers, these types of losses are equally found in all types of standard or heat powered chillers. Indeed, absorption systems have at least one additional heat exchanger with respect to supersonic ejector cycles, but the efficiency is usually much higher. Therefore, it is quite clear that the weak point of supersonic ejector cycles it is not to be found in the heat exchange, but rather in the supersonic ejector itself.

In the following chapters we first show the results obtained with the ejector chiller developed by the University of Florence in collaboration with an industrial partner. Then we address the problem of performance analysis by introducing ways to correctly define the efficiency for both the ejector cycle and the supersonic ejector alone. However, thermodynamic considerations alone are not enough to assess the quality of the project. The reason is that thermodynamic efficiency is a parameter that pertains to a single and specific resource, i.e., the **available energy** or **exergy**. Unfortunately, this is not the only resource of limited amount that an engineer must cope with. Further examples are the availability of material, space, money and time, to list some. In other words, **efficiency is not the objective function of the system design** (or not the only one). In chapter 2.4, some of these issues are addressed in order to somehow discuss what should be the goal of an engineering design or optimization process.

2.1 The DIEF chillers

Ejector refrigeration has been studied at DIEF (Department of Industrial Engineering of Florence) since the '90s and the use of environmentally safe fluids has always been at the centre of the research efforts (Milazzo *et al.*, 2014). The first prototype built by the research group was a double-stage steam ejector chiller with cooling capacity of 5 kW. The second stage was designed to pull down the evaporator to the water triple point and therefore produce ice. The steam ejector was designed by an optimization procedure described by Grazzini and Rocchetti (2002). The main innovative feature of this ejector was the peculiar second-stage injection design, with the primary stream flowing through an annular nozzle that surrounded the partially mixed stream coming from the mixing chamber. This configuration, shown in Fig. 2.1, was intended to avoid the deceleration and losses of the intermediate diffuser in a standard two-stage system (with ejector placed in series).

Unfortunately, since the beginning, the prototype has been affected by significant problems in the ejector operation. A late study (Grazzini *et al.* 2011) addressed the fluid behavior within the primary nozzle, showing that homogeneous condensation (see chapter 5) is likely to occur very near the throat region. This can produce severe pressure oscillation across the nozzle throat and prevent the chocking of the primary stream as well as stable operation[2]. Therefore, the construction of new primary nozzle is currently on the agenda, waiting for a detailed theoretical and numerical two-phase modeling.

[2] This type of condensation is sometimes called "Supercritical condensation" because the heat release is sufficient to decelerate the flow to the sonic velocity. A number of different steady or oscillating regimes have been identified under these conditions, see Bakhtar *et al.* (2005) for more details.

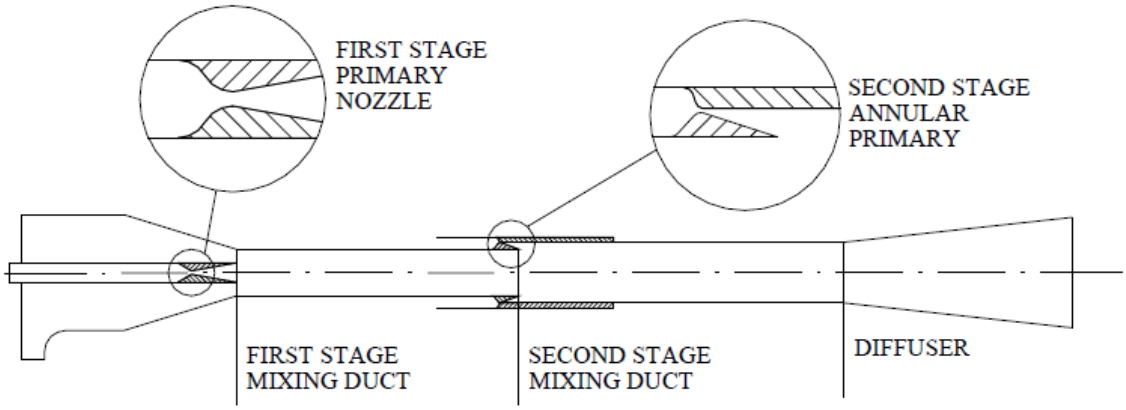

Fig. 2.1 – Design of the double-stage ejector build at DIEF laboratories

In 2010, DIEF started a fruitful cooperation with Frigel Firenze S.p.A. (Joint stock Company) in order to open new market opportunities in the field of heat driven chillers for industrial use.
The cooperation led to the project and construction of a new supersonic ejector chiller of large size. The plant has a nominal cooling power of 40 kW and is powered by low temperature heat (from 90 up to 100 °C or more). After an initial attempt to use R134a (which is the common choice for chillers in the power range covered by Frigel), thermodynamic and environmental reasoning suggested to revert to R245fa (Milazzo and Rocchetti, 2015). This fluid was selected because of its relatively high critical temperature, low system pressure ratio and, most importantly, positively sloped saturation vapor curve. Refrigerants with this last characteristic are called "dry-expansion" fluids, because an isentropic expansion from saturated conditions leads to a region of superheated vapor. By contrast, most of the natural fluids (e.g. water) are referred to as "wet-expansion" fluids because the same expansion leads to states well inside the two-phase dome (see Fig. 2.2). Despite all the aforementioned qualities, R245fa has a relatively high GWP, posing potential restrictions with respect to expected regulations on fluorinated gases. However, the growing ORC market has stimulated the formulation of low GWP alternatives matching the thermodynamic properties of R245fa, like HFO1233zd. Therefore, the results obtained with this peculiar fluid may retain their significance in the future (Mazzelli and Milazzo, 2015)[3].

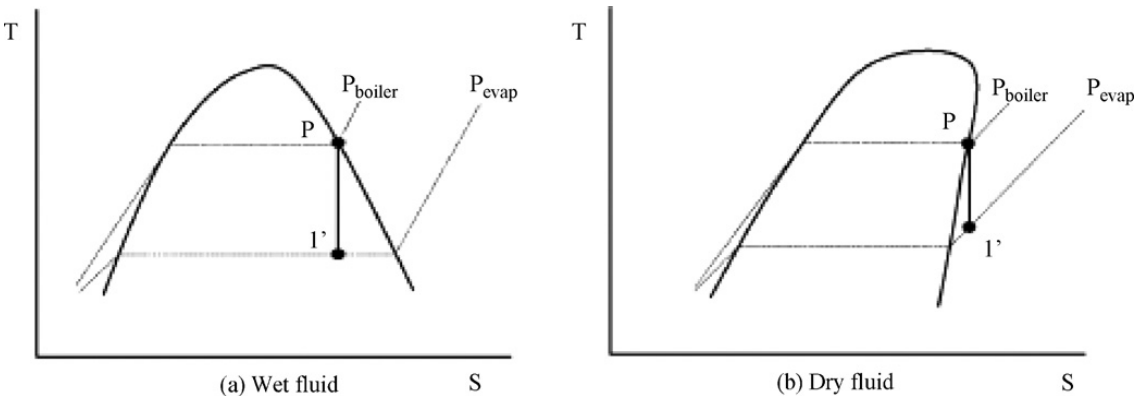

Fig. 2.2 – Wet and dry fluids (from Abdulateef *et al.* 2009)

Fig. 2.3 shows two pictures of the prototype[4]. The prototype is conceived with a "ready to market" structure. During components placing, several features had to be taken into account to permit easy

[3] Latest numerical simulations performed with HFO1233zd confirm that the performances are practically the same as those obtained with R245fa, as long as the same pressure conditions are imposed at the ejector inlets and outlets.
[4] Note that the ejector depicted in the left image was a previous version, which is now substituted by the one shown on the right

connection with external water circuits, allow user access for assembly and disassembly operations and create a compact and moveable structure. A vertical arrangement was chosen for heat exchangers. This allowed reduction of space and mitigation of cavitation problems at the pump inlet. As a consequence, the main axis of ejector is vertical as well. The ejector is equipped with a movable primary nozzle in order to optimize the axial position relative to the diffuser. At present the mechanism cannot be operated when the system is running, but in principle it could be modified for continuous adjustment during operation. Nine static pressure probes are installed along the mixing chamber/diffuser duct in order to analyze the internal pressure trends. An electronic expansion valve is used to control the liquid level in the evaporator based on overheating at the evaporator exit.

Temperature measurements are obtained by resistance temperature detectors Pt100 whose precision class is 1/10 DIN. The probes are placed at the inlet and outlet connection of each heat exchanger. Resistance values are read and converted by a National Instruments cFP-RTD-124 module. Piezoresistive pressure transducers produced by Keller are used to obtain pressure values. Two pressure probes are placed at the inlet and outlet connections of each plate heat exchanger, and nine along the ejector mixing chamber and diffuser. Water mass flow measurements in the external circuit are carried out with Endress+Hauser Promag electromagnetic flow meters. Electric power consumption of the feeding pump is measured by an electronic wattmeter.

Thus far, flow measurements inside the refrigeration plants are absent. This was made necessary by the choice of the refrigerant; in that R245fa is a non-polar fluid with very low viscosity for which the use of very large Coriolis mass flow meters is mandatory. Therefore, heat fluxes and refrigerant mass flow rates are measured by equivalence with the thermal fluxes flowing through the external water circuit. Due to this indirect method of measuring the mass fluxes, steady conditions are always sought to assure equality between water and refrigerant thermal fluxes. Nonetheless, the lack of direct mass flow measurement can lead to low accuracy of the experimental data. Hence, an extensive and detailed uncertainty analysis was performed to understand the level of confidence in the measurements; this is detailed in Appendix A.

Tab. 2.1 summarizes the final level of accuracy for each measured quantity.

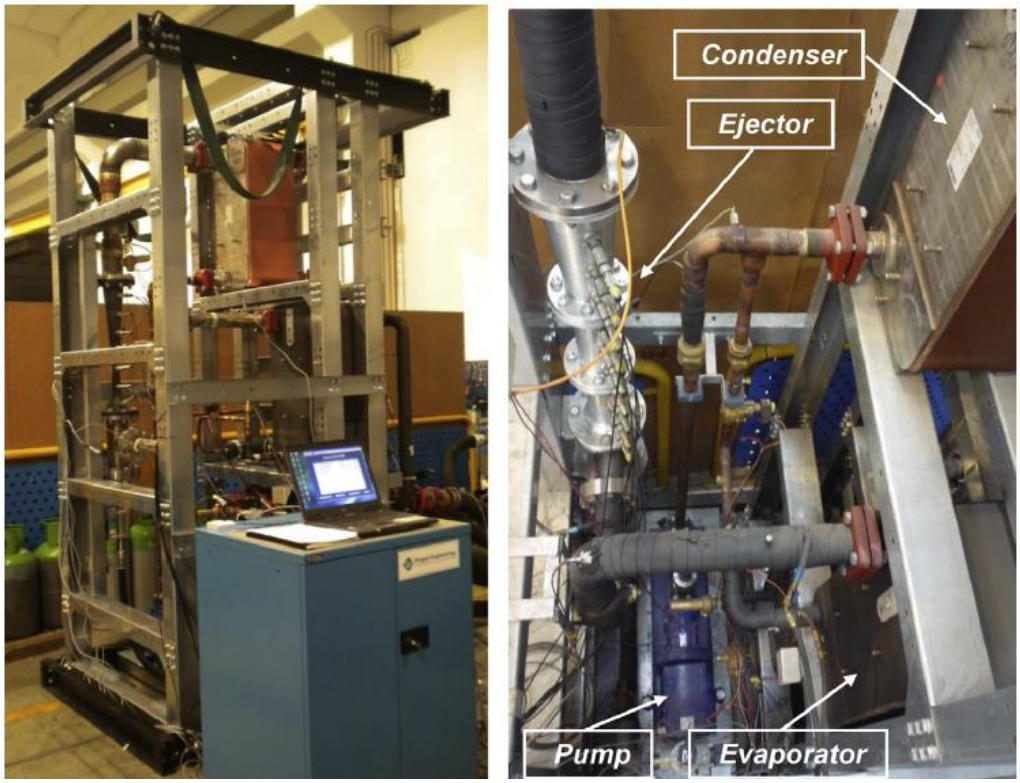

Fig. 2.3 – Pictures of the DIEF chiller build in cooperation with Frigel Firenze S.p.A.

Instrument	Model	Equipped component	ADC module	Total uncertainties
Piezoresistive pressure transducer	PA25HTT 0–30 bar	Diffuser	cFP-AI-111	±(0.1% + 0.22% FS)
	PR23R 0.5–5 bar	Evaporator	cFP-AI-111	±(0.1% + 0.22% FS)
	PA21Y 0–30 bar	Generator, Condenser	cFP-AI-110	±(0.08% + 1% FS)
Resistance temperature detectors	Pt100	Whole plant	cFP-RTD-124	±0.25 °C
Electromagnetic water flow meters	Promag 30F	Evaporator	cFP-AI-111	±(0.22% + 0.06% FS)
	Promag 50P	Generator	cFP-AI-111	±(0.5% + 0.04% FS)
	Promag 50W	Condenser	cFP-AI-111	±(0.5% + 0.04% FS)

Tab. 2.1 – Instrumentation uncertainty

The whole plant, including heat exchangers and piping, was designed using a numerical design tool based on a one-dimensional calculation method presented by Grazzini *et al.* (2012). Real fluid properties are used throughout the model by incorporating the NIST REFPROP subroutines (Lemmon *et al.*, 2013). The design code implements a routine for the design of the supersonic ejector profile. This is based on the CRMC (Constant Rate of Momentum Change) criterion by Eames (2002). The CRMC method is an attempt to reduce throat shock intensity by giving a prescribed momentum reduction rate throughout the mixing chamber and diffuser. The resulting mixing chamber/diffuser profile is continuous and, from now on, it will be called "supersonic diffuser" or just "diffuser". Two different ejectors were designed according to this code and tested. However, the performances obtained with the first two configurations were unsatisfactory (Eames *et al.*, 2013). Hence, the design concepts were reconsidered and a new ejector was manufactured. The new supersonic diffuser follows the CRCM criterion but has an increased length to improve mixing and pressure recovery (Milazzo *et al.*, 2014). Fig. 2.4 shows the geometry of the ejector currently installed in the plant while its main geometrical parameters are summarized in Tab. 2.2.

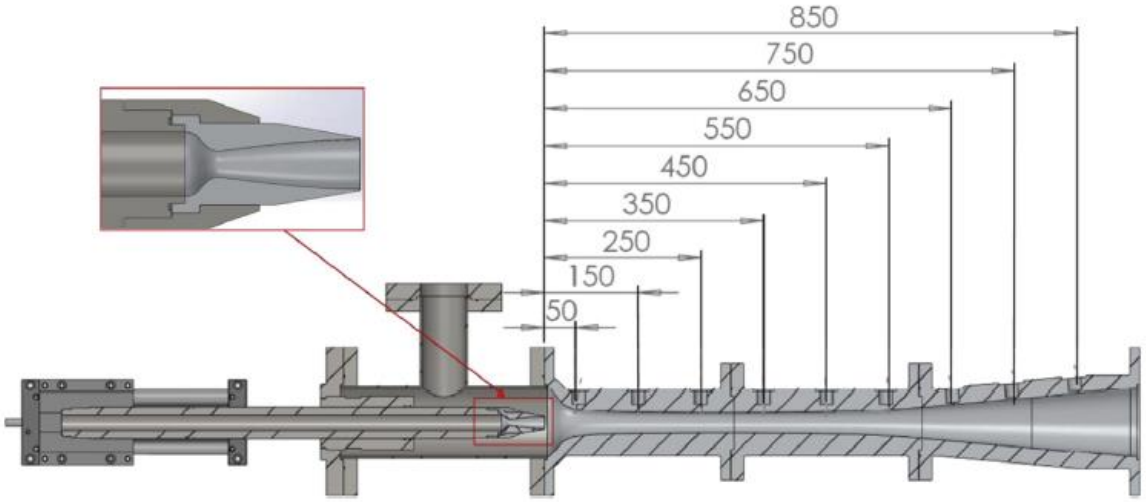

Fig. 2.4 – Design of the ejector prototype currently installed inside the DIEF chiller

	Nozzle	Diffuser
Throat diameter [mm]	10.2	31.8
Exit diameter [mm]	20.2	108.3
Length [mm]	66.4	950
Material	Aluminum	Aluminum

Tab. 2.2 – Main dimensions of the ejector prototype currently installed inside the DIEF chiller

Numerical analyses on this third design showed that, for the set of operating conditions specified by the industrial partner, the primary nozzle was working under a high level of over-expansion. Therefore, two nozzles with a smaller exit area were simulated numerically and the results are presented in Fig. 2.5 (the

related CFD scheme will be introduced later). As can be seen in the figure, a reduction of the nozzle exit area results in significant improvements both in terms of entrainment ratio and critical pressure. The improved performance is due to a reduction in the expansion level of the primary flow, which is attained by matching the nozzle exit pressure with that of the mixing chamber.

Fig. 2.6 elucidates this concept by showing the static pressure field in the mixing chamber for two simulated cases. In the previous configuration (upper half of the figure), the primary flow expands down to very low exit pressures and shocks in order to reach the mixing chamber pressure. In the new configuration (lower half of the figure), the smaller pressure difference at the nozzle exit allows for a reduction in shock train intensities and pressure losses. This is also shown in Fig. 2.7 where the region with Mach number above unity is highlighted. The sonic line is much smoother in the new configuration and correctly follows the primary nozzle profile.

Based on these results, the nozzle design with exit diameter 20.2 mm was finally selected, manufactured and inserted in the ejector. In agreement with numerical analyses, substitution of the primary nozzle produced significant improvements and now chiller performance is aligned with or exceeds the results published by other authors (as will be shown later).

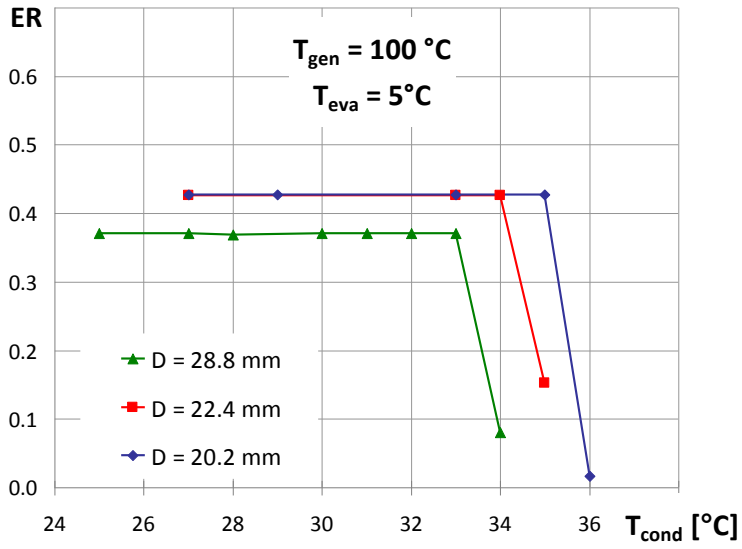

Fig. 2.5 – Entrainment Ratio for different values of the nozzle exit diameter

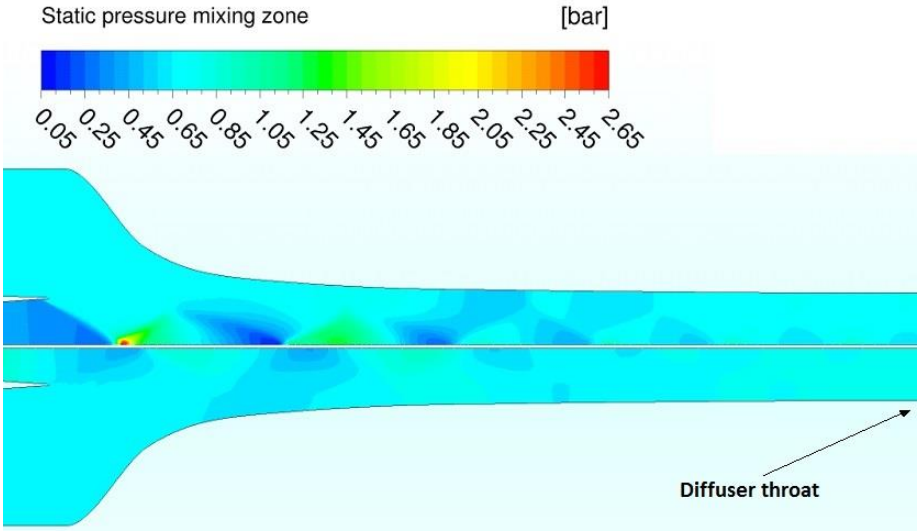

Fig. 2.6 – Static pressure in the mixing region for two different nozzle exit diameters: 28.8 mm (above the axis) and 20.2 mm (below the axis)

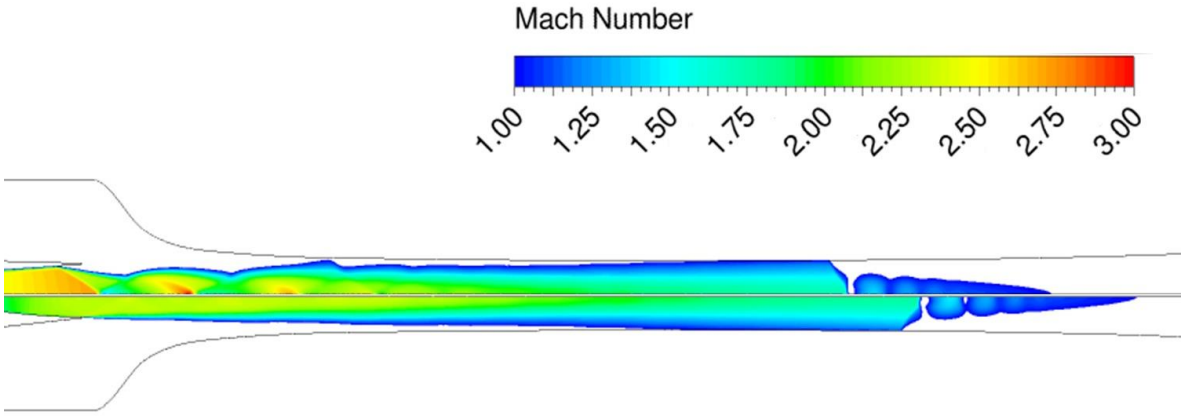

Fig. 2.7 – Supersonic Mach field along the diffuser for two different nozzle exit diameters: 28.8 mm (above the axis) and 20.2 mm (below the axis)

Fig. 2.8 shows some experimental results of the refrigerator in terms of Coefficient of Performance (COP). The error bars for each evaluated operating point represent a confidence level of 95% and were calculated according to the procedure explained in Appendix A. The generator temperature is around 90 °C which is a temperature suitable for solar cooling or waste-heat recovery applications; 5 and 10°C are imposed at the evaporator, which represent standard values for air conditioning. Finally, 5 °C superheating is set at the evaporator exit to avoid entrainment of liquid refrigerant inside the ejector.
Fig. 2.8 shows that the COP reached by the DIEF chiller is well above 0.4 when evaporating at 5 °C and around 0.55 when evaporating at 10 °C. These levels are not too far from those obtained by single-effect absorption chillers and match or exceed the performance obtained by other cycles in the literature.

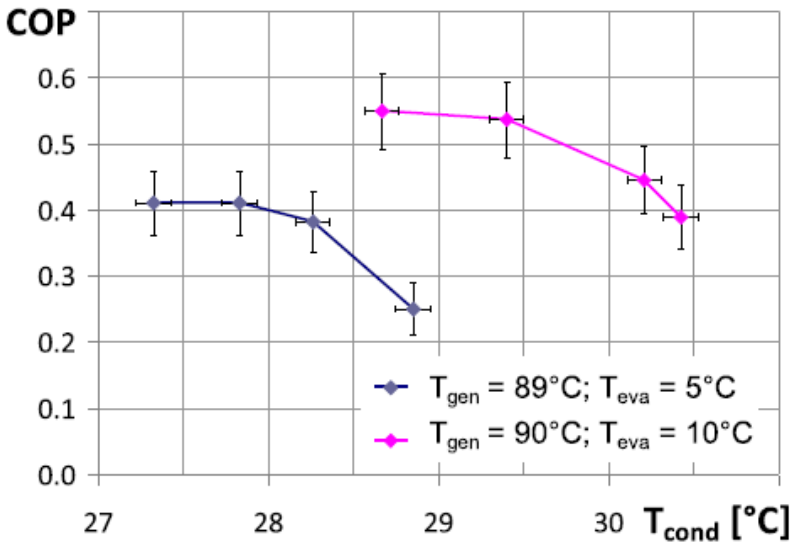

Fig. 2.8 – COP vs. condenser temperatures curves for the DIEF chiller

In recent reviews, Chen *et al.* (2013) and Little and Garimella (2016) have summarized the COP obtained by several authors. The summary from Chen *et al.* (2013) is reported in Tab. 2.3 for comparison with the results obtained by the DIEF plant. Although the COP of the DIEF chiller is the highest among those

reported in the table, the value of critical condenser temperature is below 30 °C[5]. This means that the energy content of the motive stream is mainly exploited to draw in a consistent amount of secondary flow inside the ejector. Although these aspects may transpire from a careful analysis of Tab. 2.3, in the case of chillers working under different operating conditions it is practically impossible to make quantitative performance evaluations based on the only COP.
In the next chapters the use of the Second Law efficiency is introduced with the aim of developing a tool to characterize and compare the efficiency of different plants, working under different operating conditions.

Reference	Cooling capacity (kW)	Working fluid	Evaporator temperature (°C)	Condenser temperature (°C)/pressure	Boiler temperature (°C)	COP	Conclusion
Chunnanond and Aphornratana [7]	3	Water	5:15	22:36	110:150	0.28:0.48	(1) A decrease in the boiler pressure caused the cooling capacity and COP to rise and the critical condenser pressure was reduced. (2) An increase in the evaporator pressure increased the critical condenser pressure, cooling capacity and COP, which sacrificed the desired cooling temperature.
Selvaraju and Mani [8]	0.5	R134a	2:13	26:38	65:90	0.03:0.16	(1) COP critical $= -0.375976R_d - 0.284386R_c + 0.242682\Phi + 0.933787$ (R_d=driving pressure ratio, R_c=compression ratio, Φ=ejector area ratio) (2) For given condenser and evaporator temperatures, every ejector with particular configuration has an optimum boiler temperature, at which the maximum COP can be obtained.
Sankarlal and Mani [9]	2	Ammonia	5:15	30:36	62:72	0.12:0.29	COP increased with increase in expansion ratio and decreased in compression ratio
Chaiwongsa and Wongwises [10]	1.8–3	R134a	8:16	26.5:38.5	50:60	0.3:0.48	Cooling capacity varied inversely with the heat sink (where condenser rejects heat to the cold water) temperature while it varied identically with the heat source (where evaporator is supplied by using hot water) temperature
Yapıcı et al. [13]	2	R123	0:14	108 kpa:142 kpa	83:103	0.12:0.39	(1) Optimum nozzle exit position was 5 mm outwards from the mixing chamber (2) Generator temperature higher than 97 °C resulted in constant cooling capacity but lower COP.
Ma et al. [6]	5	Water	6:13	25 mbar:65 mbar	84:96	0.17:0.32	(1) Increase the boiler temperature does not always accompany by increase in system efficiency. Maximum cooling capacity was found at boiler temperature around 90 °C. (2) Spindle can help to control ejector's primary flow and achieve fine tuning for system operation.

Tab. 2.3 – Experimental COP for various systems under different operating conditions, (from Chen et. al 2013)

2.2 Efficiency of the Supersonic Ejector Cycle

In chapter 2.1 it was pointed out that the use of the COP alone give incomplete information and is inadequate in comparing the performance of different refrigerators working under different operating temperatures. The reason for this is that parameters based on First Law evaluations do not consider the quality (or exergy) content of the energy sources and sinks. Despite so, in the every day experience it is customary to run across literature and review papers that overlook any more advanced concept than the estimation and comparison of a simple First Law efficiency.

[5] Some improvements may be reached by reducing the amount of friction losses inside the ejector. To this aim, numerical simulations have been conducted to analyze the impact of wall roughness on the global and local variables. This is detailed in chapter 4.1

In order to define the Second Law efficiency for the supersonic ejector cycle, one must compare the useful output of the real system with that of a corresponding ideal device. The ideal thermodynamic cycle of a supersonic ejector chiller can be thought as composed by two reversible parts, the motive and the refrigeration cycle, as shown in Fig. 2.9. Under stationary conditions the power output of the motive cycle must equate the power demanded by chiller (this is true for real systems as well). Despite this, the two parts of the system can produce and require different "work per cycle" and have different areas in a *T*-*s* diagram depending on the corresponding mass flow rates ("s" is the specific entropy in Fig. 2.9). Rigorously, when analyzing reversible systems one should not speak about powers and mass flow rates but rather of work output and masses, as reversibility requires quasi-static transformations which imply zero fluxes and zero power output. Hence, in order to deduce the ideal efficiency, it is assumed that the system is composed by two separated control volumes, with no energy or material fluxes crossing their boundaries (except the work exchange).

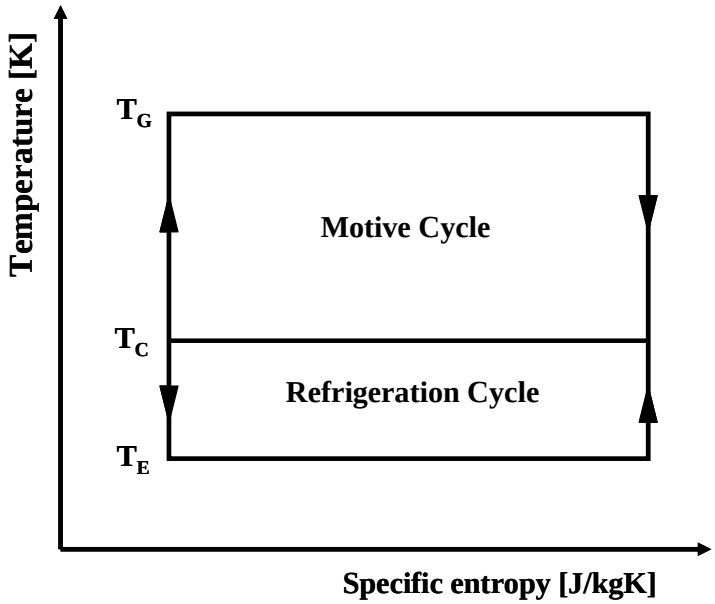

Fig. 2.9 – Ideal ejector refrigeration cycle

For the ideal motive cycle, the formulation of its efficiency is the well known Carnot efficiency, which is derived by using the Clausius theorem:

$$\eta_{m\_ideal} = \frac{W_m}{Q_G} = \frac{Q_G - Q_C}{Q_G} = \frac{T_G - T_C}{T_G} \qquad \text{eq. 2-1}$$

Where the subscript *C* stands for condenser.
The ideal efficiency or COP of the reverse cycle is obtained in the same way, provided that the useful output and input energy source are changed accordingly:

$$COP_{r\_ideal} = \frac{Q_E}{W_r} = \frac{Q_E}{Q_C - Q_E} = \frac{T_E}{T_C - T_E} \qquad \text{eq. 2-2}$$

The efficiency of the complete ideal ejector cycle is derived based on the previous relations. In this case, the useful output is the cooling load while the only energy input is the heat transferred at the boiler. The ideal efficiency is then easily obtained by considering that the work output of the motive cycle must

equate that required by the refrigeration cycle (although the specific work can be different as stated before). Moreover, the condenser temperature is the same:

$$COP_{ec\_ideal} = \frac{Q_E}{Q_G} = \frac{Q_E}{W_r}\frac{W_m}{Q_G} = COP_{r\_ideal} \cdot \eta_{m\_ideal} = \frac{T_E}{T_C - T_E}\frac{T_G - T_C}{T_G} \qquad \text{eq. 2-3}$$

The ideal efficiency is useful in many ways. First, it provides an easy tool to understand efficiency trends that are approximately followed by the real cycle. Second, it forms the basis for the definition of the Second Law efficiency, which is given by the ratio of the real to the ideal First Law efficiencies:

$$\eta_{II\_ec} = \frac{COP_{ec\_real}}{COP_{ec\_ideal}} = \frac{Q_E}{Q_G + W_{pump\_real}}\frac{Q_G + W_{pump\_ideal}}{Q_{E\_ideal}} \approx \frac{Q_E}{Q_{E\_ideal}} \qquad \text{eq. 2-4}$$

where it has been assumed that the difference between the ideal and real pump work is negligible.
It is important to underline that although it may seem natural to select the cooling load as the useful output of the system, the choice is actually arbitrary. As an example, the ejector cycle could be used in reverse mode as a heat pump (or in both ways simultaneously). The efficiency definition then would change, despite the system is the same. Fortunately, for power and refrigeration systems this problem is really marginal, as the number of different possibility are few and the useful output is usually well defined. By contrast, this is not the case when trying to define the efficiency of the supersonic ejector alone, as detailed in chapter 2.3.
Finally, it is interesting to note, that the approximate formulation for the ejector chiller efficiency, eq. 2-4, coincide with those of absorption and standard vapor compression systems. For this last, the efficiency is given by:

$$\eta_{II\_vc} = \frac{COP_{vc\_real}}{COP_{vc\_ideal}} = \frac{Q_E}{W_r}\frac{W_{r\_ideal}}{Q_{E\_ideal}} = \frac{Q_E}{Q_{E\_ideal}} \qquad \text{eq. 2-5}$$

where the ideal and real work inputs are imposed as equal.
Despite the equivalence of the final form of these equations, the way to actually calculate the efficiencies is different. In terms of practical calculations, the form of Second Law efficiency change according to type of cycle. For instance, in the case of supersonic ejector cycle, the Second Law efficiency is calculated through the following equation:

$$\eta_{II\_ec} = \frac{COP_{ec\_real}}{COP_{ec\_ideal}} = \frac{Q_E}{Q_G\left(\frac{T_E}{T_C - T_E}\frac{T_G - T_C}{T_G}\right)} \qquad \text{eq. 2-6}$$

where all the terms are known from the real system. By contrast, the equation for the vapor compression cycle is:

$$\eta_{II\_vc} = \frac{COP_{vc\_real}}{COP_{vc\_ideal}} = \frac{Q_E}{W_r\left(\frac{T_E}{T_C - T_E}\right)} \qquad \text{eq. 2-7}$$

As anticipated in chapter 1.1, the use of the Second Law efficiency provides reasons to understand the performance decrease along the "on-design" regime. When moving toward lower condenser temperatures along the plateau line, the COP of the real system remains constant. However, the COP of the ideal cycle increases due to the lower T_C. Consequently, η_{II_vc} decreases. This means that there must be a surplus of available energy (or exergy) that is wasted by the system. This exergy surplus is destroyed through a progressive increase of shock intensity in the ejector diffuser.
Fig. 2.8 presents some trends of the DIEF chiller COP. By simply dividing each value of COP by the corresponding ideal COP, it is possible to reproduce the equivalent diagram for the Second Law efficiency. Fig. 2.10 shows the results of such operation.
Although the points are few, it is clear that the two curves present a definite maximum which occurs exactly at the critical operating conditions (check Fig. 2.8 for comparison). This demonstrates again that the best operating points are always at critical condition. Moreover, the maximum height of the two curves is very similar (with a difference of around 10%), meaning that there is a lower sensitivity of this type of efficiency to operating conditions. All these aspects legitimate the use of performance maps (like that in Fig. 1.7) as the best mean to represent the results of ejector refrigerators.

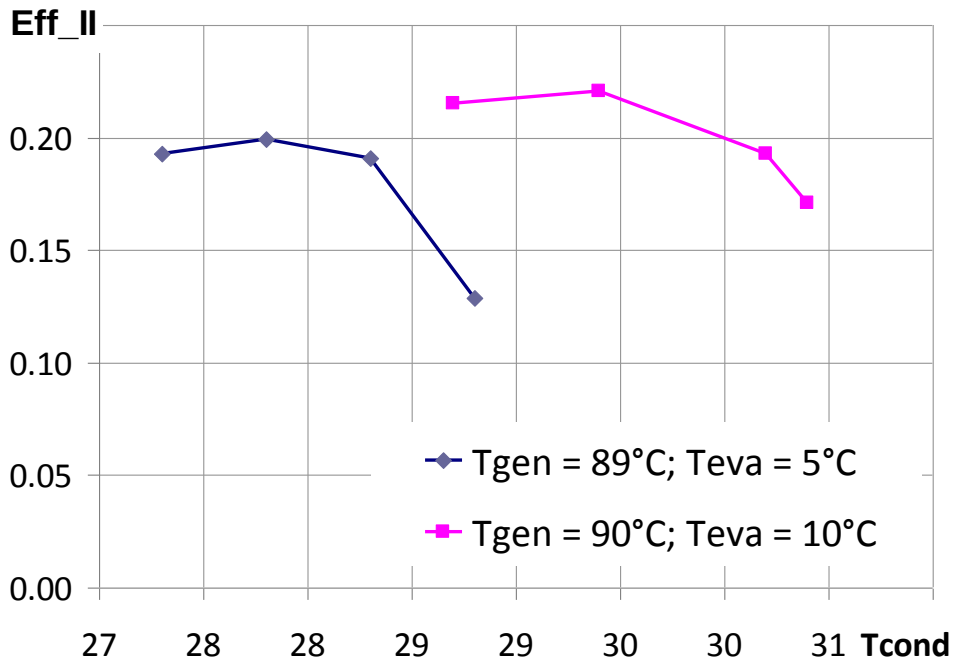

Fig. 2.10 – Second Law efficiency trend for two operating curve of the DIEF refrigerator

In Fig. 2.10 above, the curves were obtained by calculating the ideal COP based on the cycle saturation temperatures. This is a useful but rough approximation, as it implies that the level of overheating/subcooling at inlets and outlets of any heat exchanger is negligible. This may lead to some biases when comparing chillers with different levels of overheating/subcooling, e.g., in the case of cycles working with "wet fluids" like steam, where the primary fluid superheating is used to avoid or reduce condensation phenomena inside the ejector.
Furthermore, a consistent source of thermodynamic losses is always found within any heat exchanger. This type of available energy destruction may easily be greater than the one occurring inside the supersonic ejector and throttling valve. Nonetheless, this kind of efficiency loss is totally neglected when calculating the ideal COP based on the saturation temperatures. Fig. 2.11 shows a comparison between one efficiency curve from Fig. 2.10 and the corresponding curve based on the temperatures of the flow entering the heat exchangers from the external circuit side (i.e. the inlet temperature of the flow that cools

the condenser and heat up the generator and evaporator, see Fig. 1.1). As can be clearly seen, the efficiency with the new formulation is less than half of that calculated by means of the saturation temperatures.

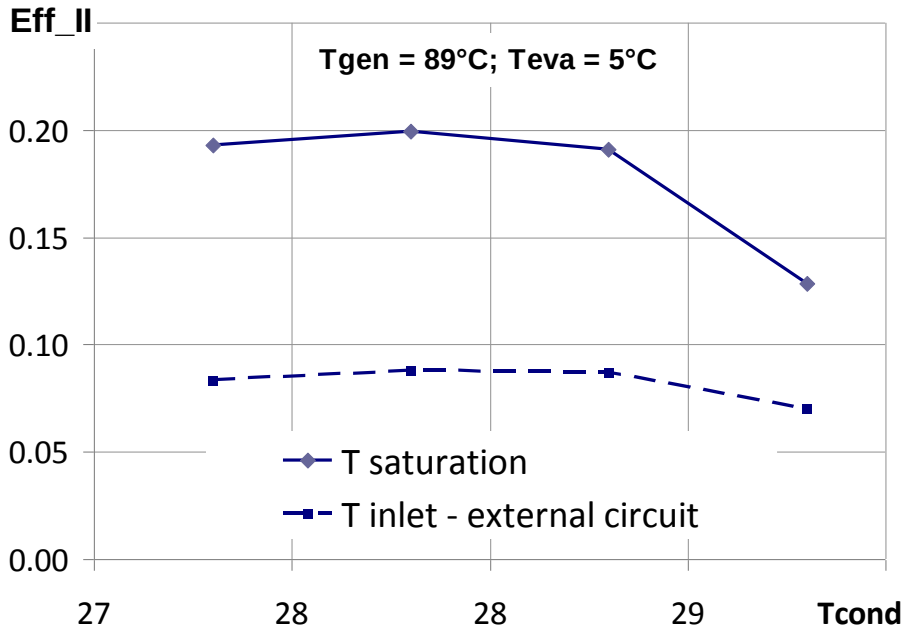

Fig. 2.11 – Comparison between η_{II} calculated through either saturation temperatures or external circuit inlet temperatures

Although the calculation of the Second Law efficiency could be made more precise by taking into for this new set of temperatures[6], in practice, this information is almost never found in the literature. Therefore, the choice of the saturation temperatures, though approximate, is most of the time the only one that allows practical comparison between different cycles.

In Tab. 2.4, the maximum value of Second Law efficiency is calculated (based on the saturation temperature) for many cycles whose data can be found in the literature. In many cases, authors do not provide for complete performance maps or charts where the critical conditions are properly highlighted. In some cases, it is also unclear whether the pump work is considered in the COP calculations. Hence, some data may not represent the real maximum performance point of the cycle.

Contrarily to what happened with COP data, the efficiency levels of different cycles are comparable despite the quite different working temperatures. This fact suggests that η_{II} is mostly influenced by differences in terms of system design while being unaffected by changes in operating conditions. In particular, having neglected all the heat exchanger losses, this comparison give information specifically on the quality of the supersonic ejector design, which is the main source of losses left. To further prove this concept, Fig. 2.12 shows an experimental COP characteristics mapped into the equivalent Second Law performance chart (data taken from Eames *et al.* 2007).

The new map clearly shows a much attenuated dependence on the operating temperatures (the points almost lye on a horizontal line). Nevertheless, though the sensitivity is lower it is still present, meaning that some conditions are more suited than other to a specific geometry (for instance, the primary nozzle is correctly expanded only for a specific set of pressure conditions, see Fig. 2.5, Fig. 2.6 and Fig. 2.7).

[6] Strictly speaking, even this way of calculating the efficiency is approximate. This is because the evaluation of the real COP does not consider the power spent by the pumps and fans to circulate water and air in the external circuits. This is, however, a usual approximation, as the external moving components may be considered features that do not belong to the cycle itself.

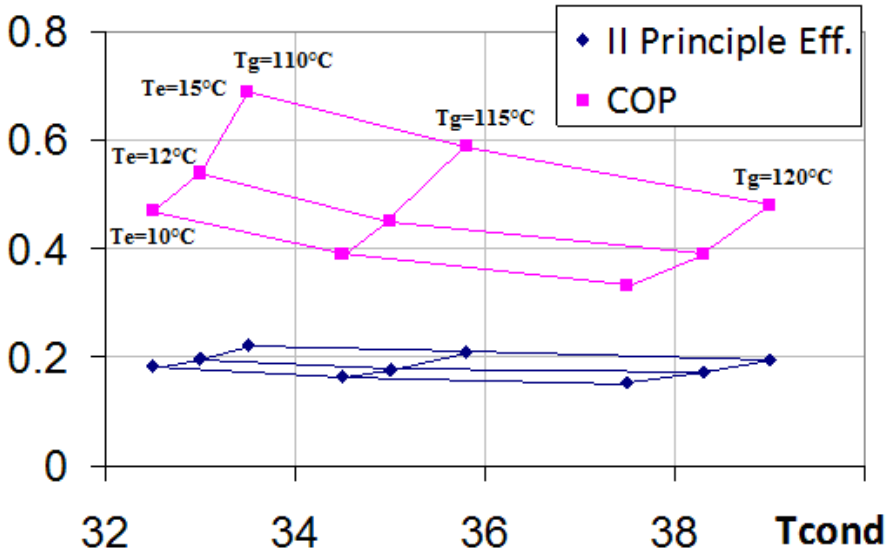

Fig. 2.12 – Comparison between COP and η_{II} performance map, data from Eames *et al.* (2007)

paper	Fluid	Cooling capacity	Super heating	Temperature range [°C]			other	Best operating point (Temperatures in °C)					
				T_{eva}	T_{gen}	T_{cond}		T_{eva}	T_{gen}	T_{cond}	COP	COP_{ideal}	η_{II}
Aphornratana and Eames (1997)	Water	1kW	not used	5:10	120:140	26:36	by excluding heat losses COP results 30% higher on average	10	120	28	0.39	3.68	0.106
Nguyen *et al.* (2001)	Water	7kW	no	1.7:5.1	73:79	26.9	passive system with 7 meter gravity head, few conditions tested	1.5	76.7	26.9	0.32	1.54	0.21
Chunnanond and Aphornratana (2004)	Water	3kW	not used	5:15	120:140	24:39	no effect detected with superheating	10	120	28	0.49	3.68	0.133
Selvaraju and Mani (2006)	R134a	0.5kW	no	2:12	65:90	27:37	6 geometry tested, nxp varies with different nozzles	12.5	70	30	0.49	1.90	0.258
Eames *et al.* (2007)	R245fa	4kW	no	10:15	110:120	32:40	recuperative heat exchanger, 2 nozzles tested, CRMC diffuser design	15	110	33.5	0.69	3.11	0.222
Yapici and Yetisen (2007)	Freon R11	1kW	no	0:16	90:102	27:34	difficult to identify critical conditions from results	9.5	102	32	0.2	2.34	0.085
Yapici *et al.* (2008)	R123	1.5kW	no	8:15	80:105	32:37	6 different geometries with different area ratios	10	90	34	0.35	1.82	0.192
Ma *et al.* (2010)	Water	5kW	10°C	6:13	84:96	17:36	primary flow control through movable spindle	13	90	36	0.47	1.85	0.254
Mazzelli and Milazzo (2015)	R245fa	40kW	no	5:10	90:100	26:36	tests made in industrial environment	10	90	29.4	0.54	2.44	0.220

Tab. 2.4 – Best performance of different refrigerators taken from the literature

2.3 Efficiency of the Supersonic Ejector

The definition of the efficiency for the supersonic ejector has been the cause of much debate and confusion, due to the possibility of selecting several different definitions depending on the arbitrary

choice of the useful output. The following analysis tries somehow to make order to this confusion and should be considered with care because the definition of a correct efficiency is at the base for any engineering design process. The analysis builds on and improves a previous work carried out by McGovern *et al.* (2012).
The common mean to define a Second Law efficiency[7] is to envision a thermodynamically reversible reference process against which the real processes may be compared. In order to effectuate this comparison, the following 4 steps are necessary:

1. Identify the "physical" input and output quantities (flows) and equations describing the process at hand.
2. Define a thermodynamically reversible reference process which can potentially substitute the real system (this means that it must have the same type of input and output parameters).
3. Choose a "useful product" or "useful output" among the different parameters at hand. The choice usually depends on the specific task that the device must perform and need not necessarily be the physical output of the system.
4. Develop a performance metric based on a comparison between the real and reversible "useful outputs". This could simply be chosen as the ratio between the two quantities.

Within this framework, efficiency can be thought as a parameter which compares the desired output of a real system with the ideal output of a reversible system that can potentially substitute it.
Following the procedure outlined above, the first step requires to identify the "physical" input and output quantities (flows), as well as the equations describing the process at hand. This is done by considering a black-box system like that shown in Fig. 2.13, for which the mass, energy and entropy balances can be written without considering the spatial dimension and geometry of the system (0D analysis).

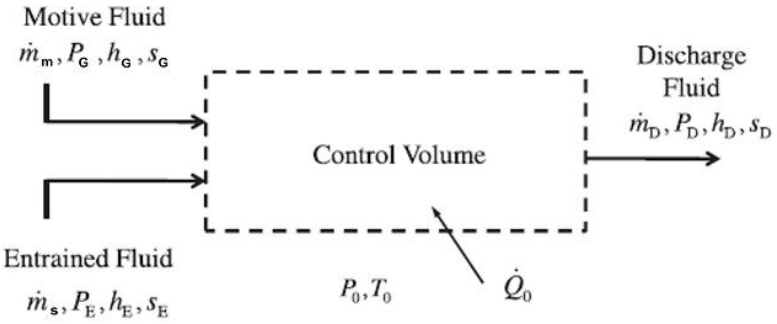

Fig. 2.13 - Simplified ejector scheme from McGovern *et al.* (2012)

This type of analysis entirely overlook the internal dynamics of the device (i.e. the momentum equation is not analyzed). At inlets and outlets equilibrium states are assumed and the fluid is considered to be in stagnation condition. For the specific case of the supersonic ejector the equations are:

$$\begin{aligned} &\dot{m}_m + \dot{m}_s = \dot{m}_D \\ &\dot{m}_m h_G + \dot{m}_s h_E = \dot{m}_D h_D \\ &\dot{m}_m s_G + \dot{m}_s s_E + \dot{S}_{irr} = \dot{m}_D s_D \end{aligned} \qquad \text{eq. 2-8}$$

In the second step, an ideal reference process must be identified. As explained by McGovern *et al.* (2012), for an ejector this can be envisioned as an ideal turbocharger coupled with a reversible engine. This ideal

[7] The first law efficiency cannot be defined for an ejector, because energy is conserved across it (see chapter 1.1)

machine, shown in Fig. 2.14, would be able to transform the pressure and temperature gradients between the primary and secondary streams into work. This work would then be reversibly delivered to the secondary flow in a way that the thermodynamic state of the two streams match prior to get in contact. Ideally, this should avoid production of mixing irreversibilities.

In the case of zero temperature difference between the primary and secondary fluid, the ideal system is simplified by the absence of the thermal engine[8]. As shown by Chunnanond and Aphornratana (2004), in this isothermal case the ideal machine becomes a simple turbocharger. Moreover, two different but equivalent configurations are possible depending on where the mixing process take place (Fig. 2.15 B or C). One of the two options consists in mixing the two currents after the compression of the suction flow (Fig. 2.15 B). In this case the primary stream expands just until the exhaust pressure (or condenser pressure). This should be the best configuration for loss reduction in a real machine, because the compressor deals just with the secondary flow and works with a lower pressure ratio (for an ideal cycle it doesn't matter, because there are no losses in any case). An alternative configuration is one in which the mixing occurs before the recompression. This second option is analogous to what happens inside ejectors, in which the primary flow expands until the evaporator pressure and then both the primary and secondary flow are recompressed until condenser pressure.

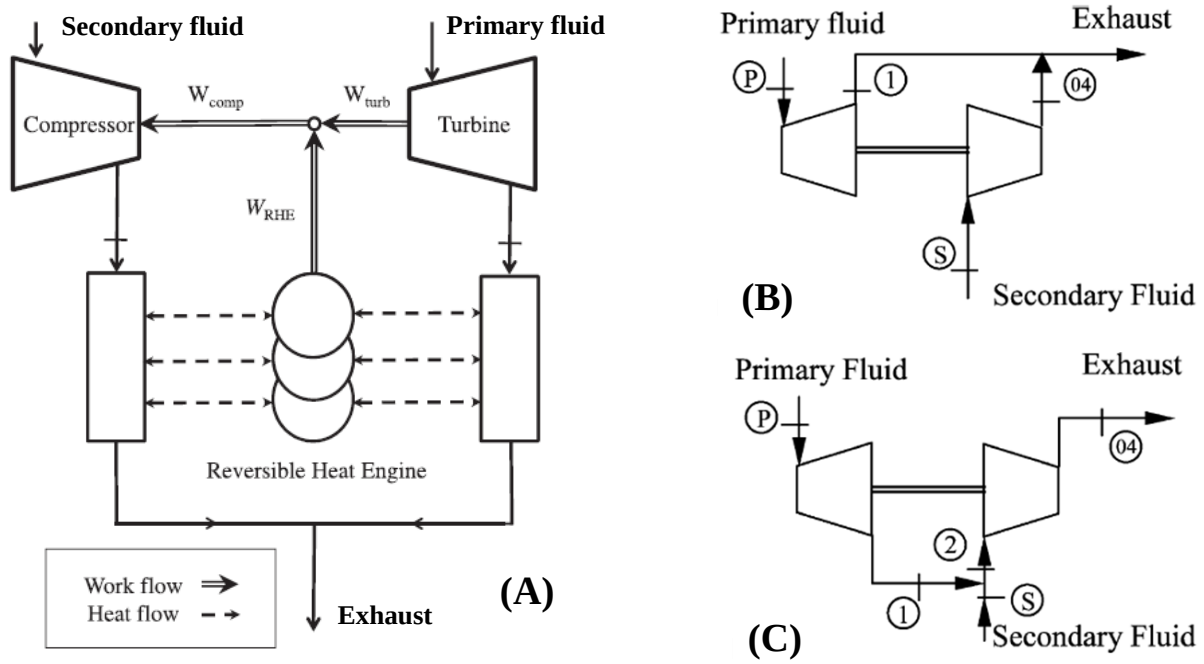

Fig. 2.14 – ideal reference systems for a supersonic ejector: reversible turbocharger coupled with heat engine (A) (adapted from McGovern *et al.*, 2012), simple reversible turbocharger with mixing after (B) or before the compression (C) (from Chunnanond and Aphornratana, 2004).

The last two steps of the procedure consist in the choice of the useful output and of the performance metric. This is the point that leads to great confusion within the literature: the arbitrariness in the choice of both the useful output and performance metric gives rise to several different efficiency definitions. For instance, one could equally adopt the ratio between the ideal and real discharge pressure, the entrainment ratio, the secondary fluid mass flow rate and so forth. Some of these options are discussed below but more can be found in (McGovern *et al.*, 2012).

[8] As could be easily observed in a *T-s* diagram, this condition occurs when the inlet value of entropy of the two streams coincides.

In order to better understand the process of these last two steps, it is useful to make a simple example that will introduce the somewhat more complicated case of the ejector efficiency. The example considers the definition of the efficiency of a gas turbine whose "black-box" scheme is shown in Fig. 2.15.

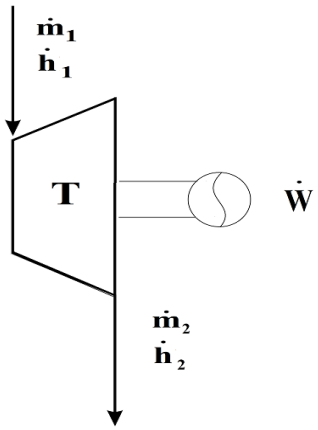

Fig. 2.15 – gas turbine "black-box" scheme

The equations of the real and reversible systems are the following:

$$\begin{aligned} & m = const && m^{rev} = const \\ & m\left(h_2(p_2, s_2) - h_1(p_1, s_1)\right) = W && m^{rev}\left(h_2^{rev}(p_2^{rev}, s_2^{rev}) - h_1^{rev}(p_1^{rev}, s_1^{rev})\right) = W^{rev} \\ & s_1 + s_{irr} = s_2 && s_1^{rev} = s_2^{rev} \end{aligned} \qquad \text{eq. 2-9}$$

where the superscript "*rev*" over the variables indicates quantities of the ideal system[9].
In order to arrive at the efficiency definition, the useful output must be identified. At the same time, all the other variables must be equated to the corresponding real quantities. In this way the two systems operate under the same boundary conditions and the comparison of the different outputs is meaningful. A common choice in the case of a gas turbine is to choose the work delivered by the turbine as the quantity of interest and to impose equal the inlet states, the cycle masses, and the outlet pressure:

$$m = m^{rev},\ p_1 = p_1^{rev},\ s_1 = s_1^{rev},\ p_2 = p_2^{rev} \qquad \text{eq. 2-10}$$

It should be noted that imposing equal pressure and entropy at inlet implies that the inlet enthalpies are the same for both systems. By contrast, the outlet enthalpy is different because the discharge entropies are different.
By substituting eq. 2-10 into eq. 2-9, the system of equations becomes:

$$\begin{aligned} & m = m^{rev} && m = m^{rev} \\ & m\left(h_2 - h_1\right) = W && m\left(h_2^{rev} - h_1\right) = W^{rev} \\ & s_1 + s_{irr} = s_2 && s_1 = s_1^{rev} = s_2^{rev} \end{aligned} \qquad \text{eq. 2-11}$$

[9] It is important to note that eq. 2-9 is written in terms of masses and work instead of mass flow rates and power output (i.e., the equations are not expressed on a per unit time basis). This is an essential feature in that, otherwise, the equation for the ideal system would produce an unattainable reversible power output

where the only different quantities between the real and ideal systems are the work outputs and exit entropies (or enthalpies). At this point, the performance metric can be simply defined as the ratio between the ideal and real useful output:

$$\eta_{turbine} = \frac{W}{W^{rev}} = \frac{(h_2 - h_1)}{(h_2^{rev} - h_1)} \qquad \text{eq. 2-12}$$

which is the well known "isentropic efficiency" for a turbine and is usually graphically described by means of an *h-s* diagram like that shown in Fig. 2.16. The larger the difference between the outlet entropies the lower the efficiency.

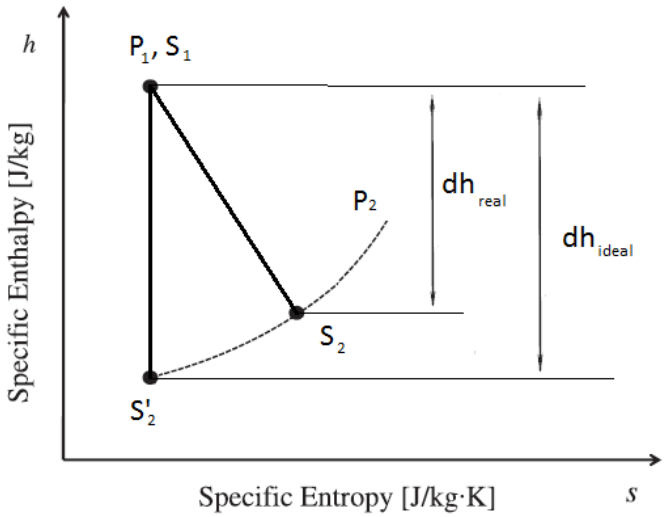

Fig. 2.16 – *h-s* diagram showing the isentropic efficiency for a gas turbine

It is important to recognize that the "isentropic efficiency" is just one of the many possible alternatives that could be devised. In particular, there are 6 independent variables in common between the two systems (m, p_1, p_2, s_1, s_2, W). In order to define the efficiency and boundary conditions only one "desired output" must be specified while leaving a further variable floating (s_2 in the preceding example). Therefore, there are 15 (6-choose-2, i.e., 6!/4!/2!) different ways in which the efficiency could be defined. In practice, the choices are lower due to additional constraints. One of these is that the inlet and outlet entropy cannot be imposed together equal to the real system, as this would imply that the irreversible entropy term is zero. This reduces the option to 12 different alternatives (e.g. the ratio of mass flow rates, the ratio of outlet pressures or inlet pressures, etc….).
Now let's turn back to the case of a supersonic ejector. The ideal reference system can be any one of the three shown in Fig. 2.14. In any of the three cases, the conservation equations for the ideal system can be written as follows:

$$\begin{aligned} m_m + m_s &= m_D \\ m_m h_G + m_s h_E &= m_D h_D \\ m_m s_G + m_s s_E &= m_D s_D \end{aligned} \qquad \text{eq. 2-13}$$

where the superscript *rev* is omitted for clarity.
By making use of the continuity equation, the discharge specific enthalpy and entropy become the mass weighted average of the corresponding inlet quantities:

$$\frac{m_m h_G + m_s h_E}{m_m + m_s} = h_D$$
$$\frac{m_m s_G + m_s s_E}{m_m + m_s} = s_D$$

eq. 2-14

On a Mollier diagram the fluid outlet state is univocally determined by the knowledge of h_D, s_D and must lie on the line joining the states of the inlet streams, as shown in Fig. 2.17.

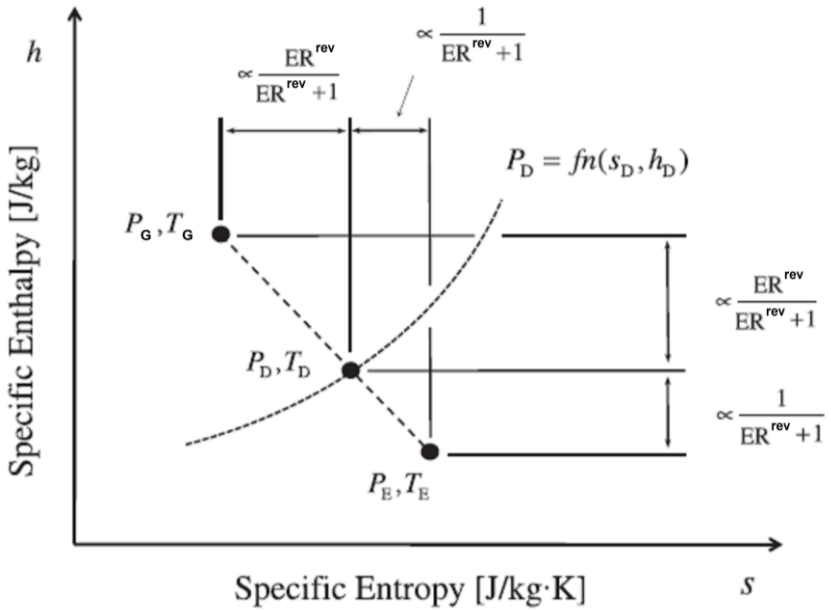

Fig. 2.17 – The final state of the reversible process must lie in the line joining the inlet motive and suction states, taken from McGovern *et al.* (2012)

The definition of the ejector efficiency follows the same procedure outlined for the gas turbine. In order to simplify the analysis, the system is reduced to the only energy and entropy equations by eliminating the discharge mass from the independent variables:

$$m_m\left(h_G - h_D\right) = m_s\left(h_D - h_E\right) \qquad m_m^{rev}\left(h_G^{rev} - h_D^{rev}\right) = m_s^{rev}\left(h_D^{rev} - h_E^{rev}\right)$$
$$m_m\left(s_G - s_D\right) = m_s\left(s_D - s_E\right) + \dot{S}_{irr} \qquad m_m^{rev}\left(s_G^{rev} - s_D^{rev}\right) = m_s^{rev}\left(s_D^{rev} - s_E^{rev}\right)$$

eq. 2-15

There are 8 independent variables in common with the real system. We must choose one variable as the useful output and let another to float, so there are totally 28 different alternatives (8 choose 2). Among these many options, there are at least two that seem to be best suited for supersonic ejector applications. The first identify the ER as the useful output and may be called the Ejector Entrainment Ratio Efficiency, η_{EER}[10]. The second, which may be called the Discharge Pressure Ratio efficiency, η_{DPR}, considers the outlet pressure as the useful variable. In order to define η_{EER}, the link between the real and ideal system boundary conditions must be as follows (where, instead of the enthalpy, we considered the pressure as an independent variable):

[10] McGovern *et al.* (2012) calls this Reversible Entrainment Ratio Efficiency, η_{RER}

$$m_m = m_m^{rev},\ \ p_G = p_G^{rev},\ \ s_G = s_G^{rev},\ \ p_E = p_E^{rev},\ \ s_E = s_E^{rev},\ \ p_D = p_D^{rev},$$ **eq. 2-16**

In practice, the inlet boundary conditions, the primary mass flow rate and discharge pressure are equated while the discharge entropies are let to be different: $s_D \neq s_D{}^{rev}$.
The equations for the ideal system thus become:

$$\begin{aligned} m_m\left(h_G - h_D(p_D, s_D^{rev})\right) &= m_s^{rev}\left(h_D(p_D, s_D^{rev}) - h_E\right) \\ m_m\left(s_G - s_D^{rev}\right) &= m_s^{rev}\left(s_D^{rev} - s_E\right) \end{aligned}$$ **eq. 2-17**

By comparing eq. 2-17 with the equations of the real system, the "Reversible Entrainment Ratio Efficiency" can be defined as:

$$\eta_{EER} = \frac{m_s}{m_s^{rev}} = \frac{m_s}{m_s^{rev}}\frac{m_m}{m_m} = \frac{ER}{ER^{rev}}$$ **eq. 2-18**

The graphical representation of the η_{EER} on the *h-s* diagram is very useful. As stated before, the final state of the ideal system lies over the line joining the motive and suction inlet states. As for the real system, the discharge pressure is the same as in the ideal process but the discharge entropy is different. Hence, the final state must lie on the same isobar passing from the ideal state but in a position shifted toward larger entropy levels. Once the real and ideal states are located in the diagram, one may compare the ER achieved in a reversible process with that obtained by the real system. This is shown in Fig. 2.18.

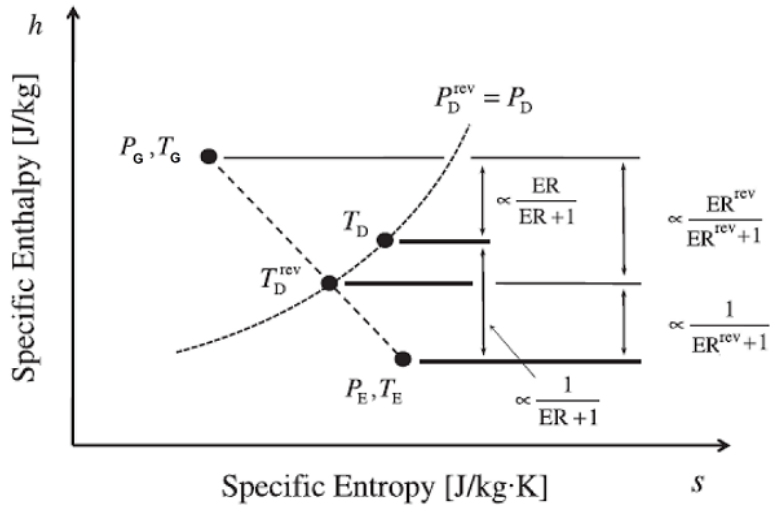

Fig. 2.18 – *h-s* diagram showing the Ejector Entrainment Ratio Efficiency, adapted from McGovern *et al.* (2012).

The definition of the Discharge Pressure Ratio Efficiency, η_{DPR}, is analogous and requires the equivalence between the inlet boundary conditions and both the primary and secondary mass flow rates (i.e. the ER):

$$m_m = m_m^{rev}, m_s = m_s^{rev},\ p_G = p_G^{rev},\ \ s_G = s_G^{rev},\ \ p_E = p_E^{rev},\ \ s_E = s_E^{rev}$$ **eq. 2-19**

where again, we let the exit entropy to be the floating variable ($s_D \neq s_D{}^{rev}$).
The ideal system equations thus become:

$$m_m\left(h_G - h_D^{rev}(p_D^{rev}, s_D^{rev})\right) = m_s\left(h_D^{rev}(p_D^{rev}, s_D^{rev}) - h_E\right)$$
$$m_m\left(s_G - s_D^{rev}\right) = m_s\left(s_D^{rev} - s_E\right) \qquad \text{eq. 2-20}$$

The Discharge Pressure Ratio Efficiency can therefore be defined as:

$$\eta_{DPR} = \frac{p_D}{p_D^{rev}} \qquad \text{eq. 2-21}$$

The η_{DPR} may also be represented graphically on a Mollier diagram where the final state of the real process must lie on a horizontal line passing from the discharge ideal state but in a position shifted toward larger entropy levels. Hence, the real discharge state is always lower than the ideal case, as shown in Fig. 2.19.

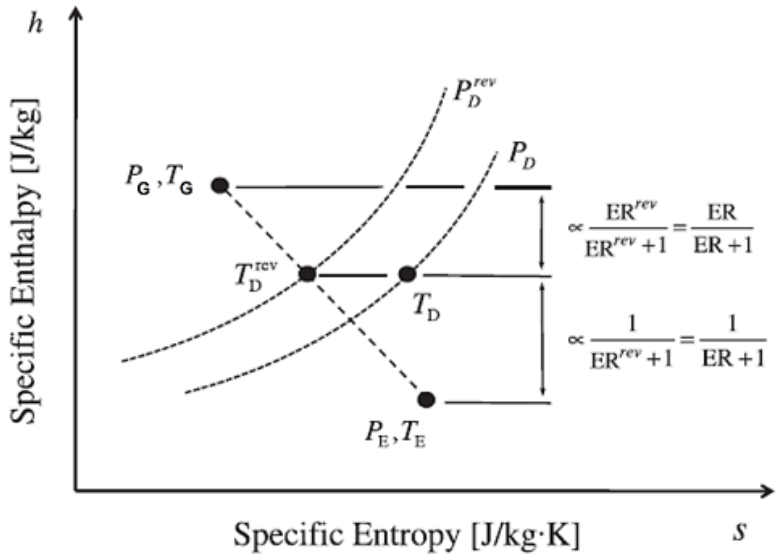

Fig. 2.19 – *h-s* diagram showing the Discharge Pressure Ratio Efficiency, adapted from McGovern *et al.* (2012).

The two efficiencies give obviously different information. The first shows the limit of ER attainable by a reversible machine while the second gives indications of the maximum discharge pressure (but it is important to remember that these limits can in principle be completed only in infinite time).
Although the choice of one efficiency over the other may be dictated by the specific application of the ejector (McGovern *et al.*, 2012), the joint adoption of both these efficiencies give an indication on how the ejector is operating by roughly answering to this question: is the ejector putting more energy into drawing secondary fluid or into compressing it?
Unfortunately, the Ejector Entrainment Ratio Efficiency, η_{EER}, and the Discharge Pressure Ratio Efficiency, η_{DPR}, are only two among 28 different alternatives. Although additional constraints may lower this number, different ways to define the performance metric can add many more options. For instance, an analogous version of the Discharge Pressure Ratio Efficiency was proposed by Arbel *et al.* (2003) and is named the Reversible Discharge Pressure Efficiency:

$$\eta_{RDP} = \frac{p_D - p_E}{p_D^{rev} - p_E} \qquad \text{eq. 2-22}$$

In this case the useful output is the same, but the performance metric is different (a ratio of differences, instead of a simple ratio).
Consequently, the real possibilities for the definition of the ejector Second Law efficiency seem to be countless. Nevertheless, there exists one approach to analyze the system efficiency that is totally independent from the arbitrary definition of specific goals: this is the exergy analysis.
In the specific case of the supersonic ejector, the exergy analysis leads to a simple efficiency definition as the ratio between the outlet to inlet exergy fluxes:

$$\eta_{ex} = \frac{\dot{E}x_{out}}{\dot{E}x_{in}} = \frac{\dot{E}x_{out}}{\dot{E}x_{primary\_in} + \dot{E}x_{secondary\_in}} \qquad \textbf{eq. 2-23}$$

where, in the case of absence of chemical reactions, the exergy flux of a power or cooling system can be defined as follows (Bejan *et al.*, 1995):

$$\dot{E}x = \dot{m}(h - T_0 s) \qquad \textbf{eq. 2-24}$$

where the T_0 is the reference state temperature.
The exergy definition, eq. 2-24, allows an easy calculation of the efficiency by simply evaluating the conditions at the ejector's inlets and outlet. Moreover, the exergy efficiency does not compare the performance of the system with those of an ideal device. Instead, it measures how much of the available energy entering the device has been destroyed or lost in the unit of time. Hence, this type of analysis is independent from the definition of an arbitrary "useful output". However, the choice of reference temperature still remains arbitrary.
Generally speaking, there are two main approaches to this problem. The first sets the actual ambient conditions as the reference state. This method allows for a realistic calculation of the exergetic performance and available energy destruction. However, this approach accounts for the "suitability" of the ambient conditions and does not quantify the performance of the system alone. For instance, a steam turbine tested in cold countries may give better exergy performances than a turbine working at lower latitudes. This may happen despite the design of the second machine is actually superior.
The second way establishes a common convention for the reference ambient conditions (e.g., 25°C and 1 atm). Although this approach allows comparison between different systems, the comparison is somewhat distorted because the real operating conditions are generally different from those of reference. Hence, the actual exergy losses may be different and the comparison may bias for one system or another.
Consequently, both these approach seem to be inappropriate for the comparison of different machines working at different operating conditions and the Second Law efficiency should give more plausible results.
By contrast, the exergy analysis is a very useful tool to perform in-depth analysis of the components. The definition of the ejector efficiency, eq. 2-23, can be easily adapted to evaluate the efficiency of the various ejector's parts, provided that a sensible partition of the system is achieved. For instance, the ejector could be divided in four parts as shown in Fig. 2.20.

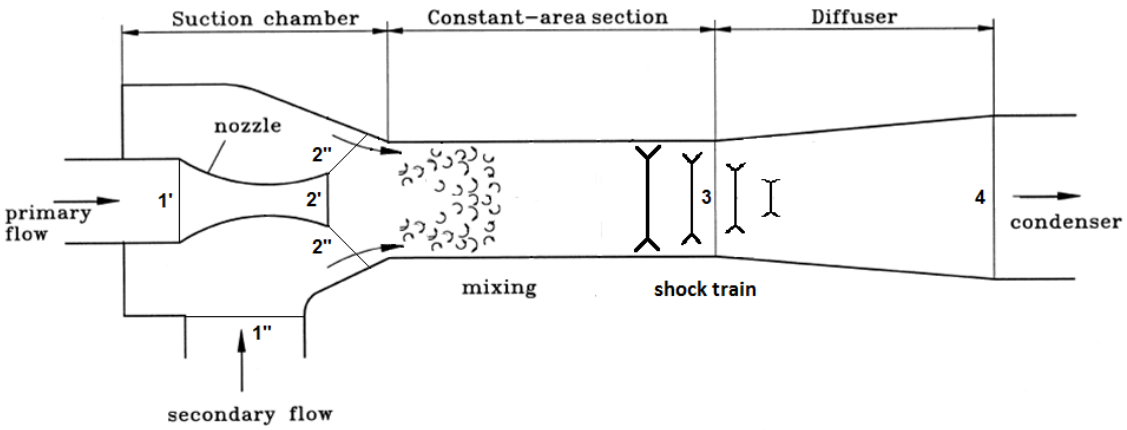

Fig. 2.20 – Schematic subdivision of the ejector regions

According to such subdivision, 4 different exergy efficiencies could be defined:

$$\eta_{primary\_nozzle} = \frac{\dot{E}x_{2'}}{\dot{E}x_{1'}} \qquad \text{eq. 2-25}$$

$$\eta_{secondary\_nozzle} = \frac{\dot{E}x_{2''}}{\dot{E}x_{1''}} \qquad \text{eq. 2-26}$$

$$\eta_{mixing} = \frac{\dot{E}x_{3}}{\dot{E}x_{2'} + \dot{E}x_{2''}} \qquad \text{eq. 2-27}$$

$$\eta_{diffuser} = \frac{\dot{E}x_{4}}{\dot{E}x_{3}} \qquad \text{eq. 2-28}$$

This type of approach highlights the regions where the losses are more intense and allows the designer to understand where the optimization is more needed.
Unfortunately, a clear distinction of the different regions may not always exist. Indeed, it is usually difficult to associate the various phenomena to as many different ejector regions. For instance, the primary expansion can proceed inside the mixing chamber or the mixing process can continue inside the diffuser. Hence, a different approach could be that of estimating the impact of the singles dissipation mechanisms on the global efficiency. This can be done by making use of the indirect formulation of the ejector efficiency:

$$\eta_{ex} = \frac{\dot{E}x_{out}}{\dot{E}x_{in}} = \frac{\dot{E}x_{in} - \dot{E}x_{lost}}{\dot{E}x_{in}} = 1 - \frac{T_0 \dot{S}_{irr}}{\dot{E}x_{in}} \qquad \text{eq. 2-29}$$

Following the course of Arbel *et al.* (2003), the various losses can be expressed by means of a linear summation:

$$\dot{S}_{irr} \approx \sum_{ejctors} \Delta\dot{S}_{irr} = \Delta\dot{S}_{irr\_shocks} + \Delta\dot{S}_{irr\_thermal} + \Delta\dot{S}_{irr\_friction} + \Delta\dot{S}_{irr\_mixing\&turbulence} \qquad \text{eq. 2-30}$$

This is clearly a first approximation, as non linear relations between factors are usually present (e.g., the interaction between surface friction and shock dissipation inside the boundary layer). However, the distinction is useful to qualitatively highlight the various form of dissipation inside a supersonic ejector.

In principle, if one could have of a good mathematical description of each term in eq. 2-30, then it would be possible to maximize the ejector efficiency by finding the design and operating parameters which makes the entropy generation a minimum. However, analytical descriptions are available just for very simplified cases that are most of the time useless in practical applications (i.e., friction factors for straight ducts, entropy generation for ideal gas across a normal shock, etc…).

Consequently, the optimization is generally accomplished by means of trial and error procedures that require exhaustive numerical and experimental investigations. Moreover, the blind maximization of the efficiency by a systematic reduction of irreversibilities may lead to a vanishing effectiveness of the component. As an example, the tendency to reduce the mixing irreversibility could induce the suppression of the mixing process itself. In practice, some available energy must be necessarily sacrificed in order to achieve the useful effect in finite time. Hence, it is clear that *thermodynamic efficiency cannot be the sole objective function of the system optimization*.

2.4 System optimization

Before taking up the optimization of any system it is indispensable to clarify the goal of the design. Without any precisely defined performance metric it is unclear in which design space to look for and the project move on by blind steps.

Typically, the objective function is different depending on the context of the research: while industries tend to minimize the total costs, thermal engineering literature is abundant of papers that aim to improve thermodynamic efficiency. However, an engineer cannot be concerned of the sole energy waste but must take into account that work or cold are needed in a certain amount of **time**.

It is known that reversible machines transform the totality of the **available energy** (exergy) from a source into work or useful output. Unfortunately, this may be achieved only when the processes are operated infinitely slow. The generation of power requires the presence of gradients of any sorts (concentration, temperature, pressure, etc…) that, when allowed to communicate, generate fluxes that reduce the gradients themselves. Hence, the production of fluxes necessarily involves losses and **no reversible power can exist**.

In order to produce a plant with both high efficiency and power output, large amount of exchanging surfaces are needed, more stages of turbines and pumps, multi level of pressure and so on… Hence, if design mistakes or misconceptions are excluded, a better plant will generally be one of larger size (Bejan *et al.*, 2011). This machine will cost more in terms of money, material and energy required for its production. Therefore, engineers always face a quite intricate puzzle because efficiency, power and costs are all inversely proportional one another. Consequently, the fundamental question of a design process is whether to look for a system that is more efficient, one that delivers more power or that minimize the total costs.

The answer to the preceding question is unclear and engineers navigate the space of all possible design alternatives without compass. Put it simple, engineers are told to project the BEST machine, but nobody knows what "best" means and how to measure it!

Many books have been written on the subject and many different schools of thought have emerged (Entropy Generation Minimization, Constructal Theory, Finite-Time Thermodynamics, Thermoeconomics, etc…). Although no definitive answer has come out (probably because *there is no* definitive answer!), many important conclusions have emerged that shed some light toward the route to take.

By considering a "Darwinian perspective", a suitable choice for the objective function would probably be the combination of thermodynamic and technological characteristics that fit at best the environmental and economic context in which the machine will operate. This is also the point of view of Constructal theory, which has born specifically as a theory for the design of open thermodynamic systems (for more details

see Bejan and Lorente, 2008). The starting point of this theory is the Constructal Law that states: "*For a finite-size system to persist in time (to live), it must evolve in such a way that it provides easier access to the imposed currents that flow through it*".

In practical terms, the law states that any system, animate or inanimate, will evolve in time changing its shape in such a way that the resistance to its internal currents (of any kind: fluid, energy, information and so on) is reduced. This means that a machine (or even living being) should evolve toward a configuration that is more efficient, being equal the power output, or that delivers more power, being equal the efficiency. The law, however, does not state in which of these two directions the system will evolve and a machine specifically designed to work at a lower power output, e.g. a machine that approach a Carnot cycle, will generally have a better efficiency than one designed for large power outputs (other conditions being equal).

As a consequence, one may ask whether there is an optimal tradeoff between the power output and the efficiency level. In other words, one may try to understand how much of the available energy should be sacrificed so that the process is completed in a finite time.

This is the question at the core of a branch of thermodynamics called Finite-Time Thermodynamics. Even though the question seems legitimate, there have been numerous controversies about the development of this theory (e.g., Moran, 1998; Gyftopolous, 1999). The major criticized point is that there is not a definite quantity of available energy that can be transformed to increase the power, as this depend on many factors (i.e. there is no relation stating that a one percent of efficiency deterioration will transform into a 1kW of additional power output). Although there might be a range of operating conditions where the power output of the system is maximized, this maximum power level, as well as the efficiency, can always be increased by improvements on the machine design, materials, reduction of internal resistances, increase of the amount of surfaces and material at disposal etc…. Consequently, the fundamental question remains and nobody knows what is the best combination of energy, time and monetary resources to choose when designing a power or refrigeration system.

The reason is probably due to the absence of principle or a quantity that can put these different resources on a same level or, in other words, a "conversion factor" that could allow the weighing of the relative worth of each resource. In the absence of such principle, the most reasonable and simple answer to the preceding question seems to be: it depends on what is needed and on the resources at disposal (e.g., if the available energy is not of concern, the design may be oriented to minimize costs or maximize power, like in renewable energy systems).

Under this perspective, the economic analysis seems to be the most suitable approach because prices represent a way to assess the worth of different types of resources (time, energy, material, etc…) by evaluating the ratio between their demand (what is needed) and supply (what is at disposal). In this regard, efforts in joining the thermodynamics and economics approaches (viz., Thermoeconomics) may constitute a promising route toward the understanding of the principles and goals of any engineering design.

Appendix A

Measurement of uncertainty

The basic ideas of measurement uncertainty are well explained by many authors (Taylor, 1997; Figliola and Beasley, 2000; Moffat, 1988). Here we follow the more specific procedure referred to as "multiple sample" or "multiple measurement" uncertainty analysis. All uncertainties are evaluated with a confidence level of 95%. Bias or systematic errors are calculated by summing up the contribution stated by the manufacturers for both the instruments and data acquisition system.

During data acquisition, each experimental point is obtained by averaging over a period longer than the longest period contained in the signal waveform. This is done in order to avoid interference errors (Figliola and Beasley, 2000). The "precision index" or "random errors" are evaluated by taking the "standard deviation of the mean" for each measured quantity. The total uncertainty for each measured quantity is thus given by:

$$U_{95\%} = \sqrt{(B)^2 + (t_{v,95}P)^2} \qquad \text{eq. 2-31}$$

where B is the total bias or systematic error for the measured quantity, P is the precision index or random error for the measured quantity, $t_{v,95}$ is the "Student's t estimator" and v are the number of acquisitions. Rigorously, v should be the number of degrees of freedom and the t estimator should be evaluated by the Student's t distribution. However, when the number of acquisitions is higher than *~60* (as in our tests) the t estimator can be considered *~2* and the difference between the degrees of freedom and the number of acquisitions can be safely neglected.

Error propagation for "derived quantities" (powers, mass flows, and enthalpies) is evaluated by square summation of the various "sensitivity indexes" (sometimes called partial uncertainties):

$$U_{95\%-derived} = \pm\sqrt{\sum_i \left(\frac{\partial R(x_i)}{\partial x_i}\cdot\delta x_i\right)} = \pm\sqrt{\sum_i (\theta_i \cdot \delta x_i)} \qquad \text{eq. 2-32}$$

where $R(x_i)$ is the "derived quantity", which is a function of several "measured quantities" x_i (e.g. temperature, pressure, etc …); θ_i is the sensitivity index, which represents the variation of the derived quantity subject to a variation δx_i of the measured quantity.

In the absence of an analytical formulation for the derived quantity (e.g., when evaluating the enthalpy of the refrigerant through NIST libraries), the sensitivity indexes are evaluated by "sequential perturbation" of the result (Moffat, 1988), that is, by numerically evaluating the sensitivity index as follows:

$$\frac{\partial R(x_i)}{\partial x_i} = \frac{1}{2}\left(\left|\frac{R(\bar{x}_i + \delta x_i) - R(\bar{x}_i)}{\delta x_i}\right| + \left|\frac{R(\bar{x}_i) - R(\bar{x}_i - \delta x_i)}{\delta x_i}\right|\right) \qquad \text{eq. 2-33}$$

where the bar over x_i indicate the average of the "measured quantity".

The experimental error obtained for derived quantities such as mass flow rates, ER and COP depend on the working conditions and are reported graphically in the results presented in chapter 2.1.

References

Abdulateef, J.M., Sopian, K., Alghoul, M.A., Sulaiman, M.Y., 2009. Review on solar-driven ejector refrigeration technologies, Renewable and Sustainable Energy Reviews 13, 1338-1349.

Al-Ansary, A.M., Jeter, S.M., 2004. Numerical and Experimental Analysis of Single-Phase and Two-Phase Flow in Ejectors, HVAC&R Research, 10:4, 521-538

Al-Khalidy, N., 1997. Experimental investigation of solar concentrators in a refrigerant ejector refrigeration machine. International Journal of Energy Research, 21, 1123–31.

Alperin, M., Wu, J.-J., 1983a. Thrust augmenting ejector, Part I. AIAA Journal 21(10), 1428–1436.

Alperin, M., Wu, J-J., 1983b. Thrust augmenting ejector, Part II. AIAA Journal 21(12), 1428–1698

Aphornratana S., Eames I.W., 1997. A small capacity steam-ejector refrigerator: experimental investigation of a system using ejector with movable primary nozzle. International Journal of Refrigeration 20, 352–8.

Aphornratana, S., Eames, I.W., 1998. Experimental investigation of a combined ejector-absorption refrigerator. International Journal of Refrigeration, 22, 195–207.

Arbel, A., Shklyar, A., Hershgal, D., Barak, M., Sokolov, M., 2003. Ejector irreversibility characteristics, Transactions of the ASME. Journal of Fluids Engineering 125, 121-129

Arora, C.P., 2003. Refrigeration and Air Conditioning, Tata-McGraw-Hill

Bartosiewicz, Y., Aidoun, Z., Desevaux, P., Mercadier, Y., 2005. Numerical and experimental investigations on supersonic ejectors, International Journal of Heat and Fluid Flow 26, 56-70.

Bejan, A., Lorente, S., 2008. Design with Constructal Theory, John Wiley & Sons, Inc., Hoboken, New Jersey

Bejan, A., Lorente, S., Yilbas, B.S., Sahin, A.Z., 2011. The effect of size on efficiency: Power plants and vascular designs, International Journal of Heat and Mass Transfer 54, 1475–1481

Bejan, A., Tsatsaronis, G., Moran, M., Thermal desing and optimization, Wiley-Interscience

Bejan, A., Vargas, J.V.C., Sokolov, M., 1995. Optimal allocation of a heat-exchanger inventory in heat driven refrigerators, International Journal of Heat and Mass Transfer 38, 2997-3004.

Bergander M.J., 2006. Refrigeration Cycle with Two-Phase Condensing Ejector, International Refrigeration and Air Conditioning Conference.

Brasz, J.J., 2003. Throttle loss power recovery in refrigeration and cryogenics, 21th IIR International Conference of Refrigeration, Washington DC, August 17-22

Cattadori, G., Galbiati, L., Mazzocchi, L., Vanini, P., 1995. A single-stage high pressure steam injector for next generation reactors: Test results and analysis International Journal of Multiphase Flow, 21(4), 591–606

Chen, L.T., 1998. A new ejector-absorber cycle to improve the COP of an absorption system. Appl Energy, 30, 37–41

Chen, X., Omer, S., Worall, M., Riffat, S.B., 2013. Recent developments in ejector refrigeration technologies. Renewable and Sustainable Energy Reviews,19, 629–651.

Chung, H., Huor M.H., Prevost, M., Bugarel, R., 1984. Domestic heating application of an absorption heat pump, directly fired heat pump. In: Proceedings International Conference University of Bristol

Chunnanond, K., Aphornratana S., 2004. Ejectors: applications in refrigeration Technology, Renewable and Sustainable Energy Reviews 8, 129–155

Disawas S., Wongwises S., 2004. Experimental investigation on the performance of the refrigeration cycle using a two-phase ejector as an expansion device, International Journal of Refrigeration, 27, 587–594

Eames, I.W., 2002. A new prescription for the design of supersonic jet-pumps: the constant rate of momentum change method. Applied Thermal Engineering, 22, 121–31

Eames, I.W., Ablwaifa, A.E., Petrenko, V., 2007. Results of an experimental study of an advanced jet-pump refrigerator operating with R245fa, Applied Thermal Engineering 27, 2833-2840.

Eames, I.W., Aphornratana, S., Da-Wen Sun, 1995. The jet-pump cycle – a low cost refrigerator option powered by waste heat. Heat Recovery Systems & CHP, 15, 711-721
Eames, I.W., Milazzo, A., Paganini, D., Livi, M., 2013. The design, manufacture and testing of a jet-pump chiller for air conditioning and industrial application. Applied Thermal Engineering 58, 234-240
Elbel, S., 2011. Historical and present developments of ejector refrigeration systems with emphasis on transcritical carbon dioxide air-conditioning applications, International Journal of Refrigeration 34, 1545-1561.
Figliola, R.S., Beasley, D.E., 2000. Theory and design for mechanical measurements, 3rd edition. John Wiley & Sons Inc., Hoboken, NJ.
Gay, N.H., Refrigerating System, 1931, US Patent No. 1,836,318
Gladstone, J., 1998. John Gorrie, The Visionary, in ASHRAE Journal: The First Century of Air Conditioning, Article 1, 29-35.
Grazzini, G., D'Albero, M., 1998. A Jet-Pump inverse cycle with water pumping column. Proceedings of Natural Working Fluids '98, June 2-5, 1998, Oslo, Norway, pp. 27-33.
Grazzini, G., Milazzo, A., Paganini, D., 2012. Design of an ejector cycle refrigeration system, Energy Conversion and Management 54, 38-46.
Grazzini, G., Milazzo, A., Piazzini, S., 2011. Prediction of condensation in steam ejector for a refrigeration system, International Journal of Refrigeration 34, 1641-1648.
Grazzini, G., Rocchetti, A., 2002. Numerical optimization of a two-stage ejector refrigeration plant, International Journal of Refrigeration 25, 621-633.
Gyftopoulos, E.P., 1999. Infinite time (reversible) versus finite time (irreversible) thermodynamics: a misconceived distinction, Energy 24, 1035–1039
Huang, B.J., Hu, S.S., Lee, S.H., 2006. Development of an ejector cooling system with thermal pumping effect, International Journal of Refrigeration 29, 476-484.
Huang, B.J., Petrenko, V.A., Samofatov, I.Y., Shchetinina, N.A., 2001. Collector selection for solar ejector cooling system. Solar Energy, 7, 269–74.
Kasperski, J., 2009. Two kinds of gravitational ejector refrigerator stimulation. Applied Thermal Engineering, 29, 3380–3385.
Keenan, J.H., Neumann, E.P., 1942. A Simple Air Ejector, Journal of Applied Mechanics 9, A75-A81.
Keenan, J.H., Neumann, E.P., Lustwerk, F., 1950. An Investigation of Ejector Design by Analysis and Experiment, Journal of Applied Mechanics 17, 299-309.
Kim, D.S., Infante Ferriera, C.A., 2014. Solar refrigeration options—a state-of-the-art review. International Journal of Refrigeration, 31, 3–15
Kneass, S.L., 1910. Practice And Theory Of The Injector, 3rd edition, John Wiley & Sons, New York
Lawrence, N., Elbel, S., 2013.Theoretical and practical comparison of two-phase ejector refrigeration cycles including First and Second Law analysis. Int J Ref, 36, 1220-232
Lemmon, E.W., Huber, M.L., McLinden, M.O., 2013. NIST Standard Reference Database 23: Reference Fluid Thermodynamic and Transport Properties-REFPROP, Version 9.1. National Institute of Standards and Technology, Standard Reference Data Program, Gaithersburg, Maryland, USA
Li, M., Wang, R.Z., 2002. A study of the effects of collector and environment parameters on the performance of a solar powered solid adsorption refrigerator. Renew Energy, 27, 369–82.
Little, A.B., Garimella, S., 2011. A Review of Ejector Technology for Refrigeration Applications. International Journal of Air-Conditioning and Refrigeration, 19, 1-15
Little, A.B., Garimella, S., 2016. A critical review linking ejector flow phenomena with component- and system-level performance, to be published
Ma, X., Zhang, W., Omer, S.A., Riffat, S.B., 2010. Experimental investigation of a novel steam ejector refrigerator suitable for solar energy applications. Applied Thermal Engineering, 30, 1320–5.

Mazzelli, F., Milazzo, A., 2015. Performance analysis of a supersonic ejector cycle working with R245fa. Int. J. Refrigeration 49, 79-92
McGovern, R.K., Narayan, G.P., Lienhard V, J.H., 2012. "Analysis of reversible ejectors and definition of an ejector efficiency", International Journal of Thermal Sciences 54, 153-166
Milazzo, A., Mazzelli, F., 2016. Ejector Chillers for Solar Cooling, in: Renewable Energy in the Service of Mankind Vol. II, Springer International Publishing Switzerland, part V, 881-891
Milazzo, A., Rocchetti, A., 2015. Modeling of ejector chillers with steam and other working fluids. International Journal of Refrigeration, 57, 277-287
Milazzo, A., Rocchetti, A., Eames, I.W., 2014. Theoretical and experimental activity on Ejector Refrigeration. Energy Procedia, 45, 1245 – 1254
Moffat, R.J., 1988. Describing the uncertainties in experimental results. Experimental Thermal and Fluid Science 1, 3-17.
Moran, M.J., 1998. On the Second-Law analysis and the failed promise of Finite-Time Thermodynamics, Energy 23(6), 517–519
Narabayashi, T., Mizumachi, W., Mori, M., 1997. Study on two-phase flow dynamics in steam injectors, Nucl. Eng. Des. 175, 147-156
Nguyen, V.M., Riffat, S.B., Doherty, P.S., 2001. Development of a solar-powered passive ejector cooling system, Applied Thermal Engineering 21, 157-168.
Papamoschou, D., 1993. Model for entropy production and pressure variation in confined turbulent mixing, AIAA journal, 31(9), 1643-1650
Power, R.B., 1993. Steam Jet Ejectors For The Process Industries, First Edition. McGraw-Hill. ISBN 0-07-050618-3.
Pridasawas, W., 2006. Solar-Driven Refrigeration Systems with Focus on the Ejector Cycle. Doctoral Thesis in Energy Technology, Royal Institute of Technology, KTH, Sweden
Riffat, S. B., 1996. International Patent PCT-GB96-00855, University of Nottingham.
Riffat, S.B., Holt A., 1998. A novel heat pipe/ejector cooler. Appl Therm Eng, 18, 93–101.
Sarkar, J., 2012. Enhanced vapor compression refrigeration and heat pump systems – A review. Renewable and Sustainable Energy Reviews, 16, 6647–6659.
Selvaraju, A., Mani, A., 2006. Experimental investigation on R134a vapor ejector refrigeration system. International Journal of Refrigeration, 29, 1160–6.
Shen, S., Qu, X., Zhang, B., Riffat, S.B., Gillott, M., 2005. Study of a gas-liquid ejector and its application to a solar-powered bi-ejector refrigeration system. Applied Thermal Engineering, 25, 2891–2902.
Sokolov, M., Hershgal, D., 1990. Enhanced ejector refrigeration cycles powered by low grade heat. Part 2. Design procedures, International Journal of Refrigeration 13, 357-363.
Srikhirin, P., Aphornratana, S., Chungpaibulpatana, S., 2001. A review of absorption refrigeration technologies. Renew Sustain Energy Rev, 5, 343–72.
Srisastra, P., Aphornratana, S., 2005. A circulating system for a steam jet refrigeration system, Applied Thermal Engineering 25, 2247-2257.
Srisastra, P., Aphornratana, S., Sriveerakul, T., 2008. Development of a circulating system for a jet refrigeration cycle, International Journal of Refrigeration 31, 921-929.
Stoecker WF. Steam-jet refrigeration. Boston, MA: McGraw-Hill; 1958.
Sözen, A., Özalp, M., 2005. Solar-driven ejector-absorption cooling system. Appl Energy, 80, 97–113.
Takeuchi, H., 2009. World's First Ejector Cycle for Mobile Refrigerators to stop Global Warming, International seminar on ejector/jet-pump technology and applications, Louvain-la-Neuve, Belgium.
Taylor, J.R., 1997. An introduction to error analysis, 2nd edition. University Science Books, Sausalito, CA.

Thevenot, R., 1979. A history of refrigeration throughout the world; translated by J.C. Fidler. International Institute of Refrigeration

Wang, J.H., Wu, J.H., Hu, S.S., Huang, B.J., 2009. Performance of ejector cooling system with thermal pumping effect using R141b and R365mfc, Applied Thermal Engineering 29, 1904-1912.

Yapici, R., Ersoy, H.K., Aktoprakoglu, A., Halkaci, H.S., Yigit,O., 2008. Experimental determination of the optimum performance of ejector refrigeration system depending on ejector area ratio. International Journal of Refrigeration, 31, 1183–9.

Yapici, R., Yetisen, C.C., 2007. Experimental study on ejector refrigeration system powered by low grade heat, Energy Conversion and Management 48, 1560-1568.

Zhang, B., Shen, S., 2002. Development of solar ejector refrigeration system. In: 1st International Conference on Sustainable Energy Technologies.

Ziapour, B.M., Abbasy, A., 2010 First and Second Laws analysis of the heat pipe/ejector refrigeration cycle. Energy, 35, 3307–14.

Part II – Single-Phase Supersonic Ejectors

Chapter's index:

The last two or three decades have seen a significant amount of work aimed at improving ejectors efficiency (see for instance, Dutton and Carroll, 1986; Grazzini and Rocchetti, 2002, 2008; Zhu et al., 2009; Cai *et al.*, 2011). A major problem in these types of studies is the definition of the goal of the optimization, as discussed in chapter 2. In any event, once a suitable objective function is identified, the optimization of the system can be performed following either a more mathematical or physical route. In the first case, theoretical or numerical models are used to systematically test different system configurations and find the one that gives the best performance. This type of approach requires the adoption of a "search or optimization algorithm" suitable for the specific type of "design space" under study (i.e. the virtual space of all the possible geometrical configurations). This approach is sometimes referred as "blind optimization" method, in that the physics of the system is important only in so far as it provides a realistic mathematical model of the system.

A different type of approach is to remove the "blind fold" and try to steer the system design by using all the information at our disposal. This method, that we could call "informed optimization", exploits the knowledge of the physics and loss mechanisms inside the system in order to orienteer the search in the configuration space. Moreover, a deeper knowledge of the ejector phenomena is also very useful in constructing accurate numerical and analytical scheme of the ejector.

With this goal in mind, chapter 3 illustrates thoroughly the physics of single-phase supersonic ejectors. The analysis is made by subdividing the ejector into three different regions of interest: the primary nozzle and secondary adduction, the mixing chamber and the diffuser regions. Special consideration is given to the description of losses mechanisms and ways through which they can be prevented.

In Chapter 4, the focus is on the modeling of ejector flow physics. Chapter 4.1 illustrates CFD results obtained for the ejector currently installed in the DIEF chiller. The discussion is corroborated by suggestions on how to perform accurate simulations. Chapter 4.2 introduces a model of the turbulent mixing inside the ejector that allows calculations of many parameters like ER, pressure and temperature trends, shear work etc…. In the following chapter, the results of the model are validated against CFD results for a constant area mixing chamber subject to adverse pressure gradients. Finally, in chapter 4.4 the model is used to suggest a possible optimization of the momentum exchange inside the mixing chamber.

3. Ejector dynamics

The global behavior of the ejector results from a combination of complex flow features including, shock diamonds, turbulent mixing layers bounded by wall regions, compressibility effects like shock-induced separations, vortex shedding, boundary layers subject to adverse pressure gradients, recirculation regions and so forth. It is because of this complexity that ejector designs and performances have thus far been difficult to characterize and optimize.
In what follows, it will be shown that the knowledge of the ejector dynamics allows the definition of many empirical rules useful to optimally design the supersonic ejector.

3.1 Primary Nozzle & Secondary adduction

In common practice, the ejector geometry is designed as a sum of straight lines neatly divided by sharp corners. In many cases, this is done for reasons of simplicity and ease of manufacturing. In addition, this simple configuration allows the definition of a discrete and limited number of variables that can be optimized by means of parametric analyses. ESDU (1986) and Pope and Goin (1978) give empirical prescriptions and optimal ranges for many of these parameters, like the nozzle throat diameter, mixing chamber length and diameter, inflection angles, etc….
However, using straight lines is clearly a restriction in the design process. ESDU manual (1986) states that it is always better to avoid sharp edges between the various parts. This is particularly true for the primary nozzle, were the high speed reached by the motive flow demand for smooth surfaces in order to reduce friction. Moreover, the presence of sharp angles or profile discontinuities may increase the risk of shock formation due to the overlapping of compression waves. With regard to these aspects, Pope and Goin (1978) remark the great importance of a smooth and gradual transition between the converging and diverging part: “experience has shown that a low tolerance in the actual coordinate of a nozzle is of considerably less importance than low tolerances on the smoothness and continuity of curvature downstream of the initial expansion at the throat”.
Once an appropriate design is obtained, friction and compressive effects may be considered negligible and the flow inside the nozzle can be described by the isentropic flow approximation. In the simplest approach, the Quasi-One-Dimensional theory can be employed to predict the flow inside the nozzle or design its profile (see for instance, Hodge and Koenig, 1995). Unfortunately, the Q1D theory can only give indications about the radial dimensions of the geometry and no information can be extracted about the longitudinal distances between the various parts.
A more accurate approach is the use of the Method Of Characteristics (MOC, see for example Zucrow, 1976). This method allows the analysis and design of any continuous internal or external geometry, as long as the governing equations are hyperbolic and the flow is isentropic (i.e. irrotational supersonic flow). To date, the MOC technique is ordinarily employed to design the nozzles of supersonic and hypersonic wind tunnels with both planar and axial symmetries (Pope and Goin, 1978). Several different MOC techniques were proposed over the years depending on the different design purposes. For instance, some of these aimed at generating the most uniform flow in the test section of a supersonic wind tunnel (Pope and Goin, 1978; Shope, 2005). Other types were intended to yield minimum length nozzles (Brown and Argrow, 1999) or optimal thrust nozzles for space propulsion applications (Hoffman *et al.*, 1972). In addition, a number of empirical techniques were developed to design the contraction of the nozzle (i.e. the subsonic part) and to control the evolution and stability of the boundary layer (Pope and Goin, 1978).
Unfortunately, the application of MOC to axially symmetric geometry requires the 3D version of the method which is really involved and requires software to be computed. Hence, before undertaking the

adoption of this technique, it is important to realize whether the MOC approach can produce results that are in line with those needed by a nozzle that operates inside a supersonic ejector.
Probably, the most obvious aspect to consider is the reduction of the internal losses due to friction. The most appropriate design in this regard should be the minimum length nozzle (Brown and Argrow, 1999), as long as the stability of the boundary layer is warranted (too short nozzles imply very large inflection angles that may lead to boundary layer separation). However, due to the general high efficiency of the primary nozzle the design should not only consider friction losses, but rather look at the processes that take place downstream. In other words, a proper nozzle should be designed to reduce the losses of the mixing process and to enhance the entrainment effect in the mixing chamber.
As stated in chapter 2.3, in order to reduce mixing irreversibilities the static state of primary and secondary flow should be the same. This allows reduction of the heat exchange between the fluids as well as the shock adaptation of the primary flow (see Fig. 2.5 in chapter 2.1). This matching of the static state may be achieved by a correct choice of the refrigerant and cycle characteristics coupled with a careful design of the primary nozzle. In a *T-s* diagram this process translates in making the end points of the primary and secondary expansion be the same (i.e. the points *2* and *3* of Fig. 3.1 should coincide). Moreover, due to the very low efficiency of the recompression process (the curve *4-5* is inclined in Fig. 3.1), the mixing pressure should be the highest possible, which means, almost equal to the secondary stagnation pressure. This is achieved by a correct design of the secondary inlet duct, which should be large enough not to accelerate the secondary stream (the path represented by the points from *2** to *5** in Fig. 3.1).

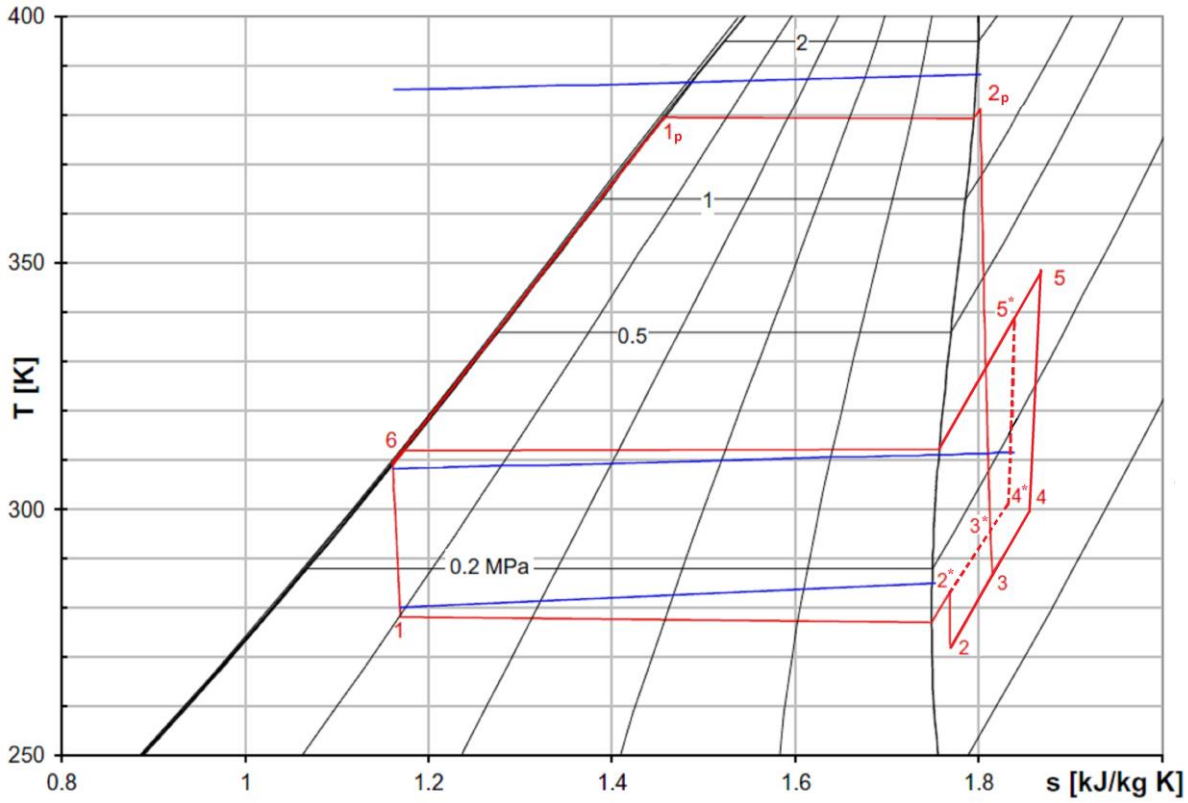

Fig. 3.1 – *T-s* diagram of a real ejector refrigeration cycle, the blue lines represent the external circuit temperatures, the dotted lines are the path followed by an ejector having no acceleration of the secondary flow

The above empirical rules serve the purpose or reducing mixing losses. However, it is not clear yet how the primary and secondary nozzle should be designed in order to enhance the entrainment effect. As an

example, increasing the secondary flow density (i.e. lower inlet temperature) or the surface of interaction between the two streams (e.g., by petal or annular nozzles) may lead to faster mixing and a reduced length of the mixing chamber. However, all these solutions can result in greater heat and friction losses. In general, one may conclude that an effective mixing requires larger gradients and velocities which, in contrast, produce greater losses; at the opposite extreme is the loss-free and indefinitely slow quasi-static mixing process. Hence, it is not easy to understand whether a proposed solution will provide benefits in terms of efficiency. The absence of any certain rule in this regard is due to a lack of knowledge in the fundamental dynamical mechanisms that occur inside the mixing chamber.

3.2 Mixing Chamber region

When the primary and secondary flow meet inside the mixing chamber, they give rise to a narrow region of strong mixing called "mixing layer". From the point of view of supersonic ejectors, the focus is on the more specific case of "compressible mixing layers", whose main problems are well illustrated in monographs like those from Smits and Dussauge (2006) and Gatsky and Bonnet (2013).

Fig. 3.2 shows the main features of a mixing layer. Outside this region the primary (motive) and secondary (suction) streams flow isentropically. Inside the mixing layer, the time-averaged velocity smoothly varies from the value of the undisturbed primary stream to that of secondary stream. The extension of the shear region is usually measured by the definition of a "shear layer thickness". This is a fundamental quantity for the analysis and prediction of the mixing process. Unfortunately, there are many ways to define this thickness that are not completely equivalent and lead to difficulties in the comparison of experimental data.

In what follows, only one of these will be considered, i.e., the "vorticity thickness", but more details are provided by Gatsky and Bonnet (2013).

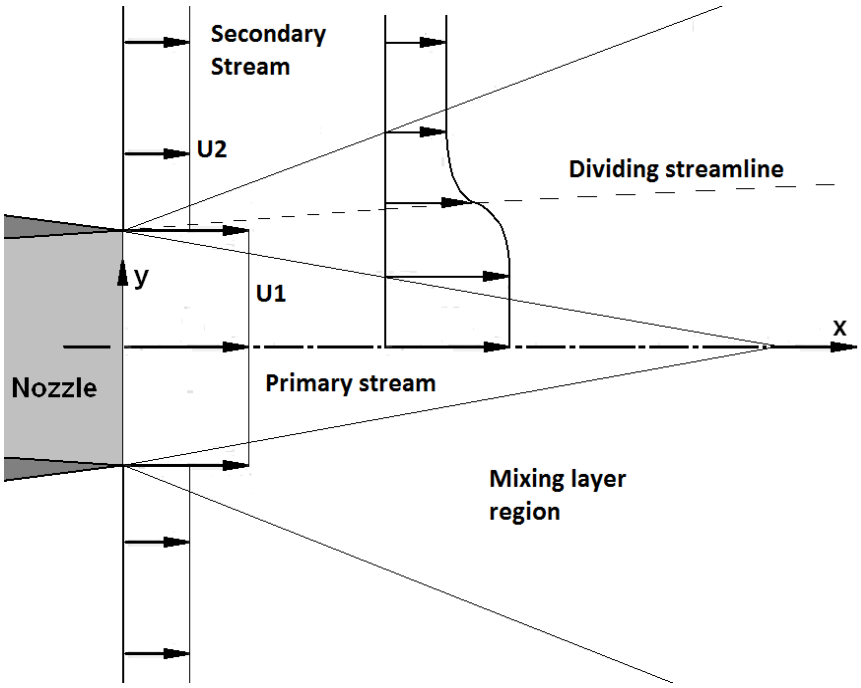

Fig. 3.2 – Mixing layer inside an ejector[11]

[11] The dividing streamline is the virtual line that separates two regions having mass flow rates equal to that of the primary and secondary mass flow rates, respectively (more details are provided in chapter 4.2)

The vorticity thickness is defined as the distance given by the velocity difference across the layer divided by the maximum slope of the velocity profile:

$$\delta_\omega = \Delta U_\infty \Big/ \left(\frac{\partial U}{\partial y} \right)_{\max} \qquad \text{eq. 3-1}$$

where ΔU_∞ is the difference between the undisturbed primary and secondary stream velocities.
This definition is mostly useful whenever the mixing layer velocity profile is approximately described by an analytical function. For instance, if the velocity profile can be described by a hyperbolic tangent (this is a recurrent choice in the literature), the knowledge of the vorticity thickness allows exact definition of the mixing layers edges. An easy way to illustrate this concept is to consider a linear velocity profile inside the mixing layer. In this case the velocity thickness becomes:

$$\delta_\omega = \Delta U_\infty \Big/ \left(\frac{\partial U}{\partial y} \right)_{\max} = \Delta U_\infty \Big/ \left(\frac{\Delta U}{\Delta y} \right)_{\infty} = \Delta y_\infty \qquad \text{eq. 3-2}$$

That is, the shear layer thickness is exactly equal to the transversal extension of the linear profile.
The shear layer thickness is not the only one important parameter in the analysis of mixing layer. A further fundamental quantity is represented by the "spreading rate" of the shear layer thickness along the longitudinal direction. This is simply defined as:

$$\delta'_\omega = \frac{d\delta_\omega}{dx} \qquad \text{eq. 3-3}$$

An interesting feature of most shear flows (jets, mixing layers, and wakes) is that the spreading rate of the shear layer, eq. 3-3, is constant, i.e. the shear region grows linearly with distance (see Fig. 3.2).
A key aspect that is of particular concern for supersonic ejector studies is that compressible mixing layers are affected by a significant reduction of the spreading rate with respect to equivalent low-speed configurations. This feature has been identified in several experimental investigations performed in the 70s (e.g., Brown and Roshko, 1974; Ikawa, 1973) and severely reduces the effectiveness of mixing inside supersonic layers. The causes of this phenomenon have been the subject of studies for more than 50 years, and yet no clear explanation has been found. Early studies tried to explain the effect by the density variations resulting from the high expansion of the motive stream. However, the experimental work of Brown and Roshko (1974) demonstrated that this was not the main cause and that the reason could be the impact of compressibility on the turbulence structure of the flow. Papamoschou and Roshko (1988) later found that the decrease of mixing layer spreading rate may be described by means of a parameter called Convective Mach number:

$$M_c = \frac{\Delta U_\infty}{a_{\infty 1} + a_{\infty 2}} \qquad \text{eq. 3-4}$$

where $a_{\infty 1}$ and $a_{\infty 2}$ are the sound speed of the primary and secondary stream outside the mixing layer.
The use of the Convective Mach number allows approximate correlation of the experimental data of compressible mixing layer spreading rates. Many type of correlation based on this parameters have been proposed (see Smits and Dussauge, 2006), but none could really reproduce the experimental data with enough confidence (the uncertainty are usually well above 20%). Among these, one of the most simple

and popular was provided by Papamoschou and Roshko (1988) and later readapted by Papamoschou (1993, 1996):

$$\delta'_{\omega} = \delta'_{\omega\_incomp} \cdot f(M_c) = 0.085 \cdot \left[\frac{(1+\eta)(1-r)}{(1+r\eta)} \right] \cdot f(M_c) \qquad \text{eq. 3-5}$$

where $\eta = \sqrt{\rho_{\infty 2}/\rho_{\infty 1}}$, $r = U_{\infty 2}/U_{\infty 1}$.

The terms inside square brackets in eq. 3-5 describe the effect of density and velocity difference across the layer, which is to increase the spreading rate for large velocity differences as well as when the density is greater on the low speed side.

The function $f(M_c)$ is called "compressibility function" and is defined as the ratio of the compressible to incompressible spreading rate. In practice, the definition of this parameter is aimed at concentrating all the effect of compressibility in a single function. In case the mixing layer is almost incompressible, the value of this function is unitary and eq. 3-5 can be used to approximately describe the spreading rate of low-speed mixing layers. When the mixing layer is highly compressible, the compressibility function is well below unity and brings about a significant reduction in the mixing layer spreading rate. From the correlation of several experimental data, $f(M_c)$ can be expressed by an exponential function, as follows (Papamoschou, 1993, 1996):

$$f(M_c) = \frac{\delta'_{\omega}}{\delta'_{\omega\_incomp}} \approx 0.25 + 0.75 e^{-3M_c^2} \qquad \text{eq. 3-6}$$

Unfortunately, eq. 3-6 shows discrepancies of the order of 20% or more with respect to experimental data (Papamoschou, 1993). This may be explained by considering that, in general, mixing layers are influenced by blockage effects, thickness and surface conditions of the splitter plate, inlet turbulence level and acoustic disturbances (Smits and Dussauge, 2006). These effects are hardly captured by the use of a single parameter like the compressibility function. A greater accuracy may be achieved by the introduction in eq. 3-5 of some additional variables accounting for these factors. Unfortunately, it is still very difficult to isolate and measure these "second order" effects with current experimental means and all previous investigations lack of information and data in this regard. It is quite easy then to understand the reasons of the failures of the last fifty years in theoretically reproduce the effect of compressible mixing layers.

However, despite the low accuracy, eq. 3-5 provides a mean to easily calculate the spreading rate by the knowledge of flow conditions in the isentropic region outside the layer. Moreover, the knowledge of the spreading rate allows deriving a fundamental equation for the maximum shear stress inside the mixing layer. By means of dimensional arguments it can be demonstrated that the maximum shear stress is approximately given by (Papamoschou, 1993):

$$\tau_{\max} \sim \rho_{avg} U_{avg} \Delta U_{\infty} \cdot \delta'_{\omega} = K \cdot \frac{1}{2} (\rho_{\infty 1} + \rho_{\infty 2}) \Delta U_{\infty}^2 \left[\frac{(1+\eta)(1+r)}{2(1+r\eta)} \right] \cdot f(M_c) \qquad \text{eq. 3-7}$$

where K is an empirical constant, obtained from subsonic constant-density experiments. Papamoschou (1993, 1996) suggests use of Wygnanski and Fiedler's value, K = 0.013 (Wygnanski and Fiedler, 1970).

The knowledge of the shear stress in some point of the mixing layer is important because it allows the calculation of the momentum balance without recurring to complex numerical procedure and turbulence models. This knowledge will be exploited in the definition of a model of the mixing layer, introduced in chapter 4.

3.3 Diffuser region

The project of the mixing chamber and diffuser regions are the most delicate and challenging. The two preeminent sources of dissipation inside supersonic ejectors generally consist of the friction losses and sonic shocks, which are both consistently present in these regions.

Despite the long tradition in wind tunnel testing, the design of supersonic or transonic diffusers is still a very complex task. Differently from supersonic nozzles, the dynamics of diffusers is not described by irrotational flow. This is due to the severe losses attending the interaction of shocks or compression waves with the boundary layer (for more detail on these aspects, the reader may refer to Smits and Dussauge, 2006). Hence, the Method Of Characteristics (which is strictly valid for irrotational flows) does not hold anymore and design is usually performed by empirical methods.

In general, the main parameters to be considered in the design of a supersonic diffuser are the total length, the inflection angles of the converging and diverging region, the size of the throat section. In order to reduce the shock intensity, the throat section needs to be reduced so that the Mach number at the throat is minimum (Zucker and Biblarz, 2002). Although this allows a reduction in shock intensity, very small throat sections may incur in start-up problems and a reduction of the range of optimal on-design conditions. Moreover, the reduction of friction losses demands for very short diffuser lengths. On the other hand, this leads to large inflection angles that impact on the stability of the boundary layer and possibly cause detachment and recirculation regions.

Due to all these problems, it is quite clear that the design of diffusers in supersonic ejectors is a very complicated issue that requires extensive trial and error design procedure, and detailed numerical analysis for the validation of the proposed design. Nevertheless, some useful design rules can be achieved by considering the behavior of shocks and boundary layers in supersonic internal flows.

The configuration and intensity of the shocks inside generic channels depends on many factors: the Mach number upstream of the shock, the geometry of the duct, the intensity and direction of the pressure gradient and, most importantly, the presence and interaction with the viscous boundary layer (Matsuo *et al.*, 1999). This is normally stable when the pressure is decreasing in the direction of the boundary layer growth, i.e., for supersonic nozzles. However, it becomes unstable and tends to separate from the wall when the pressure is increasing in the direction of growth, i.e., for diffusers (Pope and Goin, 1978).

Experimentally, it has been observed that with an increasing Mach number, the shock configuration changes from that of a single normal shock to a sequence of lambda shocks, called “shock train”, as show in Fig. 3.3.

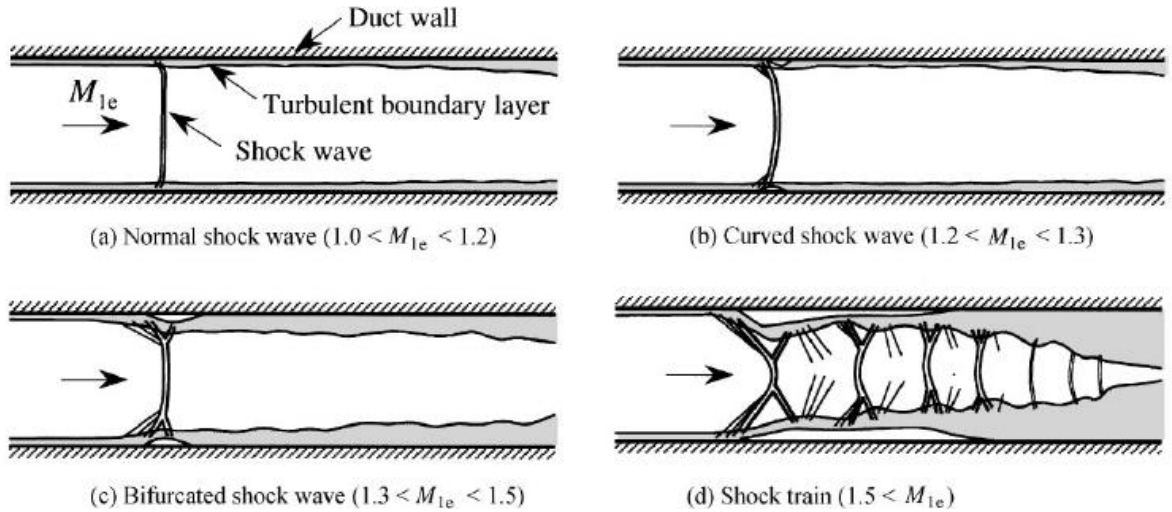

Fig. 3.3 – Sketch of shock/boundary layer interaction leading to the shock train, from Matsuo *et al.* (1999)

The causes of the formation of the shock train are to be found in the complex interaction between the shocks and the viscous boundary layer. A proof for this is given by a visual investigation at various boundary layer thicknesses (Matsuo *et al.*, 1999). The test is performed by forcing the shock to occur at different positions along the duct, where the boundary layer is at different stage of development. As shown in Fig. 3.4, a decreasing height of the boundary layer thickness reduces the formation of the pseudo shock. In the ideal case of complete absence of boundary layer, the sonic shock would be perfectly normal. This information is important in ejector design because the pseudo shock produces greater losses than an equivalent normal shock occurring at the same upstream Mach number (Matsuo *et al.* 1999). Hence, the presence of any obstacle or geometrical feature that produces an increase in the boundary layer thickness should be avoided.

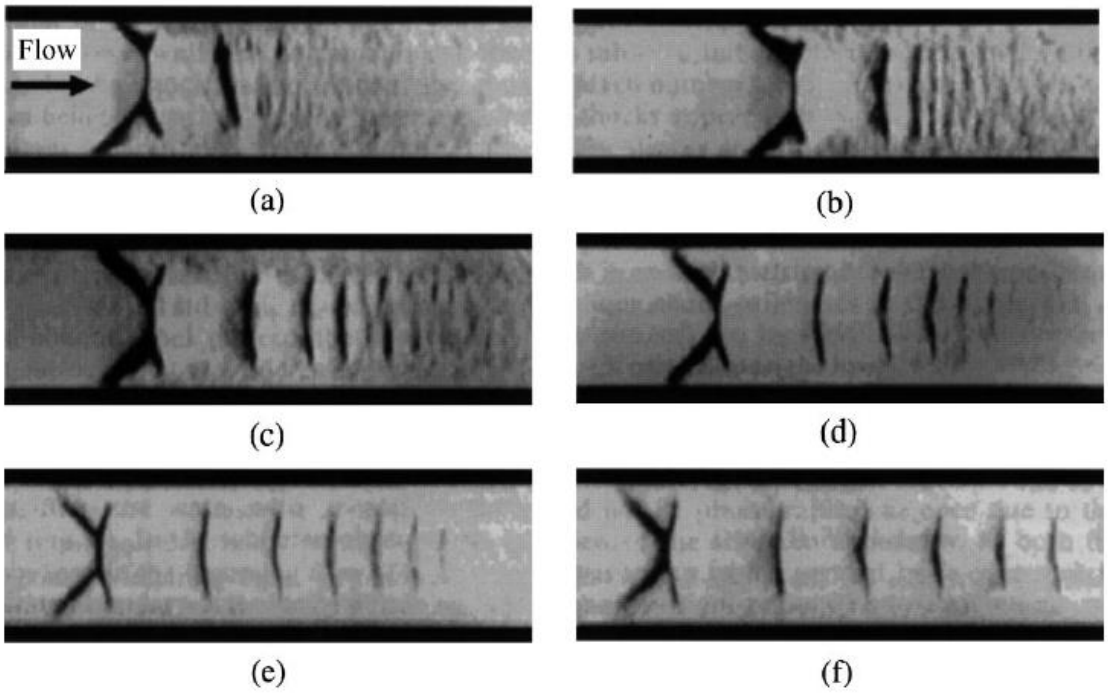

Fig. 3.4 – Pseudo shock formation at different levels of the boundary layer thickness, the upstream Mach=1.6 and is constant in all tests. The boundary layer thickness progressively increase from (a) to (f), from Matsuo *et al.* (1999)

In the case of a straight channel, downstream the region of the shock train, the central part of the duct is still occupied by supersonic flow. The mixing of the high speed core with the surrounding subsonic flow leads to an increase of the static pressure until a maximum value is reached. This is followed by a zone of decreasing pressure due to friction losses, as illustrated in Fig. 3.5. The region consisting of both the shock train and the static pressure rise is referred by Matsuo *et al.* as ‘‘pseudo-shock’’, which also list several simplified model of the pseudo shock model. Although these could be employed within an ejector model, the assumption of a normal shock generally predict the pressure rise across the shock with an uncertainty that is approximately within 6% (Johnson and Wu, 1974). Consequently, the adoption of more complicated schemes may be avoided. Furthermore, none of the proposed models takes into account the event of a non uniform velocity profile. Non uniform velocity fields, with an external region slower than the centre of the duct, frequently occur in supersonic ejector due to the possibility of an incomplete mixing process. The presence of this type of flow field could be a further cause of formation of the shock

train[12]. The length and effectiveness of the mixing process then becomes an important parameter to reduce shock losses in the diffuser: whereas longer diffusers may produce greater frictional losses, the increased uniformity of the flow could lead to lower shock losses.

A first attempt of reducing the shock intensity within the mixing chamber/diffuser is provided by the CRMC method devised by Eames (Eames, 2002; Grazzini *et al.*, 2012). By imposing a controlled rate of momentum variation to the mixed flow, the resulting profile is continuous and consists of a convergent/divergent channel. In the ideal case of a uniform flow, this design could lead to a passage to subsonic conditions without shock. In real conditions this is obviously unattainable. Nevertheless, at design conditions, the CRMC profile should reduce the irreversibility due to the normal shock.

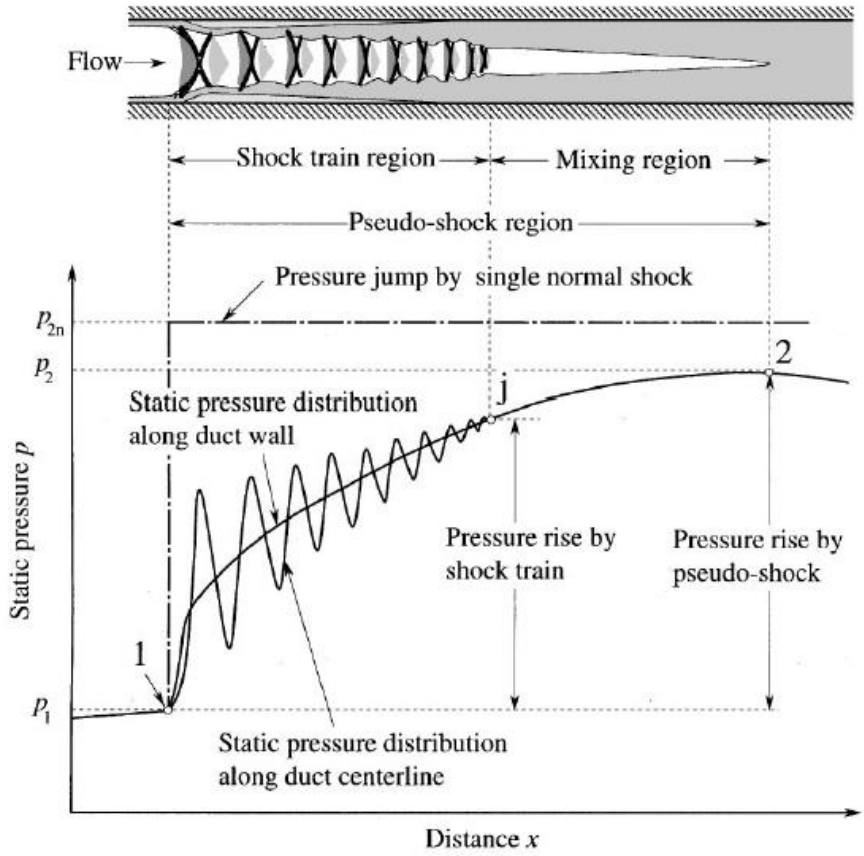

Fig. 3.5 – Schematic static pressure distribution along the duct centerline and wall surface in constant-area duct, from Matsuo *et al.* (1999)

[12] As stated before, the presence of the boundary layer may be at the origin of the shock train. However, the boundary layer itself is nothing more than a special non-uniformity in the velocity flow field.

4. Ejector modeling

In this chapter, the problem of ejector modeling is addressed both from the point of view of numerical and theoretical approaches. It will be shown that many custom approximations in ejector research must be reconsidered if an adequate level of accuracy is to be found.

4.1 CFD modeling

With the advent of modern computational techniques, new tools for analyzing the complex physics of supersonic ejectors have become available. However, to date these tools are still far from being completely reliable, making experimental validation necessary. In particular, some authors have shown that discrepancies between CFD and experiments are strongly related to operating conditions (Bartosiewicz *et al.*, 2006; Mazzelli *et al.*, 2015). From these studies, it results that the prediction of ER at off-design conditions is significantly more challenging than that at on-design regime.

Previous studies (Bartosiewicz *et al.*, 2005, 2006; Hemidi *et al.*, 2009a, 2009b) blamed this low accuracy on turbulence modeling approximations. Although this may represent a source of error, it is by no means neither the only nor the most important cause of the discrepancy with experimental data. Indeed, the fact that the prediction of mass flow rates and ER is highly accurate at on-design conditions means that the entrainment process is well captured by CFD simulations. This is mostly due to turbulence model accuracy in predicting the turbulent shear work and turbulence intensity inside the mixing layer. For the compressible shear layers some corrections are necessary, but still, the accuracy is surprisingly good (Mazzelli *et al.* 2015, Bartosiewicz *et al.*, 2006; Sriveerakul *et al.*, 2007).

In a recent paper, Mazzelli *et al.* (2015) performed numerical and experimental analyses to evaluate the impact of turbulence modeling on the accuracy of ejector flow simulations. Three series of experimental curves were compared with 2D and 3D simulations, using four different turbulence models. It was found that while differences between turbulence models were not so large (although the k–ω SST model performed slightly better than the others), the correct evaluation of the shear losses at the wall would impact significantly the accuracy of the simulations.

Indeed, the large discrepancies that are seen at off-design conditions results from the failure of the CFD models to match the transition point toward the single-choked regime (i.e., the critical pressure). The correct prediction of this process requires accurate evaluation of the total pressure losses inside the mixing chamber and upstream the diffuser shock. Due to the high levels of speed and compressibility, these losses strongly depend on **wall friction**. Hence, in order to achieve an adequate level of accuracy, it is important to properly account for the surface roughness.

For historical reasons, the commonly used roughness definition in fluid dynamics is what is called the "uniform sand-grain roughness height", K_{sg} (for details see Taylor *et al.*, 2005). This is defined as the mean diameter of the sand grains that cover the surface, as illustrated in Fig. 4.1. In general, this particular roughness definition is what must be input in CFD codes (e.g., ANSYS Fluent User's Guide, 2013). However, the "uniform sand-grain roughness height" is a quantity that is not measured by common profilometers. These latter usually return some average of the surface vertical displacement, e.g., the arithmetic average height, K_a, or the root mean square height, K_{rms}. Consequently, some conversion factors are necessary to compare measured roughness heights with values employed for numerical simulations.

Unfortunately, there is no exact conversion factor to transform a measured average roughness (arithmetic or root mean square) into an equivalent value of uniform sand-grain roughness. A recent work from Adams *et al.* (2012) estimated theoretically the conversion factors and found that these may be calculated by considering $K_{sg} \sim 3\ K_{rms}$ (also found by Zagarola and Smits, 1998) and $K_{sg} \sim 5.9\ K_a$. By comparison

with experimental data they showed that conversion factors are subject to large uncertainty and should always be regarded as indicative values. Nevertheless, they concluded that using the conversion factor is always a better approximation than to use none.

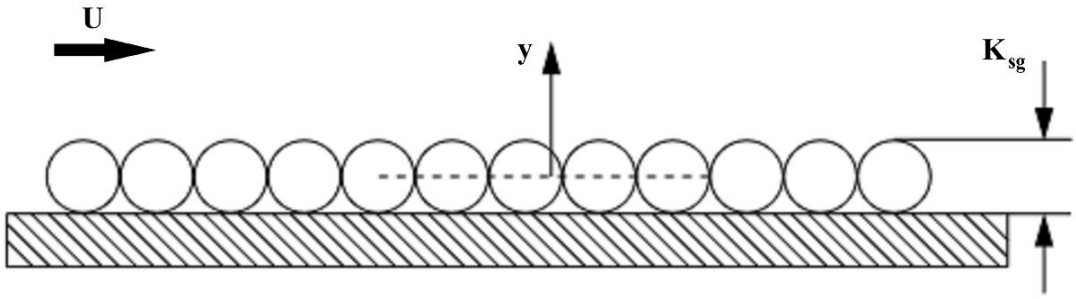

Fig. 4.1 – Sand Grain Roughness Height corresponds to the diameter of the sphere representing the sand grain (from ANSYS Fluent User's Guide, 2013)

The influence of wall roughness on numerical accuracy was investigated by Mazzelli and Milazzo (2015). The analysis that follows extends these results by further considering the impact of heat transfer across the ejector walls. It will be clear that the usual assumptions of hydrodynamically smooth and adiabatic surfaces lead in many cases to error at least comparable, if not greater, than those ascribed to turbulence models.

The numerical scheme and computational domain used for the simulations is illustrated in figure Fig. 4.2. Many features were considered in order to setup a reliable scheme, whose details and validation can be found in Mazzelli and Milazzo (2015).

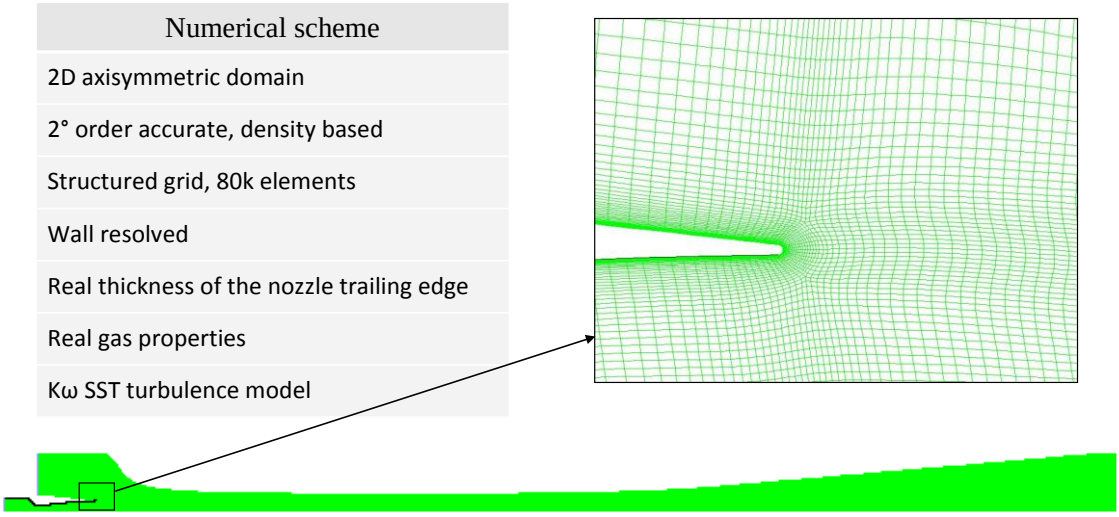

Fig. 4.2 – Numerical scheme and Mesh characteristic for the CFD simulations

The main results of this analysis are condensed in Fig. 4.3, which reports the same experimental data described in chapter 2.1. All at once, this chart shows the importance of the correct evaluation of the momentum and heat transfer at the ejector walls. In observing Fig. 4.3, the attention should be focused on the curve representing the numerical scheme with smooth and adiabatic walls (the fuchsia curve). This is the setup that is commonly adopted by most of the studies in ejector research. Notably, while this scheme correctly reproduces the ER results for the on-design regime, the same model is far from being accurate at off-design conditions.

By simply introducing a small amount of wall roughness, the results for the ER curve change dramatically. In particular, the gold and light-blue curves correspond to sand-grain roughness heights of

10µm and 20µm. Clearly, as the condenser pressure increases, higher values of friction cause the critical point to appear in advance. This result is indeed expected, as greater friction translates into larger amounts of total pressure losses, thus reducing the capability of the flow to withstand high values of back pressure.

By inspection of Fig. 4.3, it appears that the curve with 10µm roughness overestimates the critical pressure, which corresponds to about 28°C of saturation temperature. By contrast, the curve relating to 20µm roughness height seems to capture well the transition point, though it underestimates the ER at higher temperatures. The green and purple curves in Fig. 4.3 represent two numerical schemes with 20µm roughness height and two values of constant wall temperatures. These are set equal to the condenser and ambient temperature correspondingly (for this last it was considered $T_{amb} = T_{cond} - 5°C$). While imposing a constant temperature along the external wall is clearly a simplification, nonetheless, some interesting aspects can be understood by this approximate analysis[13]. In particular, Fig. 4.3 shows that the lower is the wall temperature, the higher becomes the critical pressure. Hence, it appears that a net heat loss toward the ambient produces a positive effect in terms of flow stability.

Finally, it can be noted that the presence of friction also influences the steepness and extension of the off-design regime. A higher level of roughness causes the range of "non-choked" operations to become larger. Despite this, CFD results don't seem to reproduce exactly the parabola of the off-design experimental trends. The reason for this failure may be due to the severe pressure gradient and attending recirculation regions that form at high condenser pressures, which can hardly be evaluated by numerical simulations.

In Fig. 4.4, the same results of Fig. 4.3 are reported by separating the curves related to the primary and secondary mass flows. As one could expect, the numerical discrepancy with experiments is mainly due to the prediction of the secondary flow rate while the primary nozzle flow is correctly predicted. Nonetheless, it is important to always report data of mass flow rates alone because, in many cases, the error in ER may be lowered or augmented by compensation effect that hide the real accuracy of numerical simulations (e.g. when both the primary and secondary mass flow rates are overpredicted, see Mazzelli *et al.*, 2015).

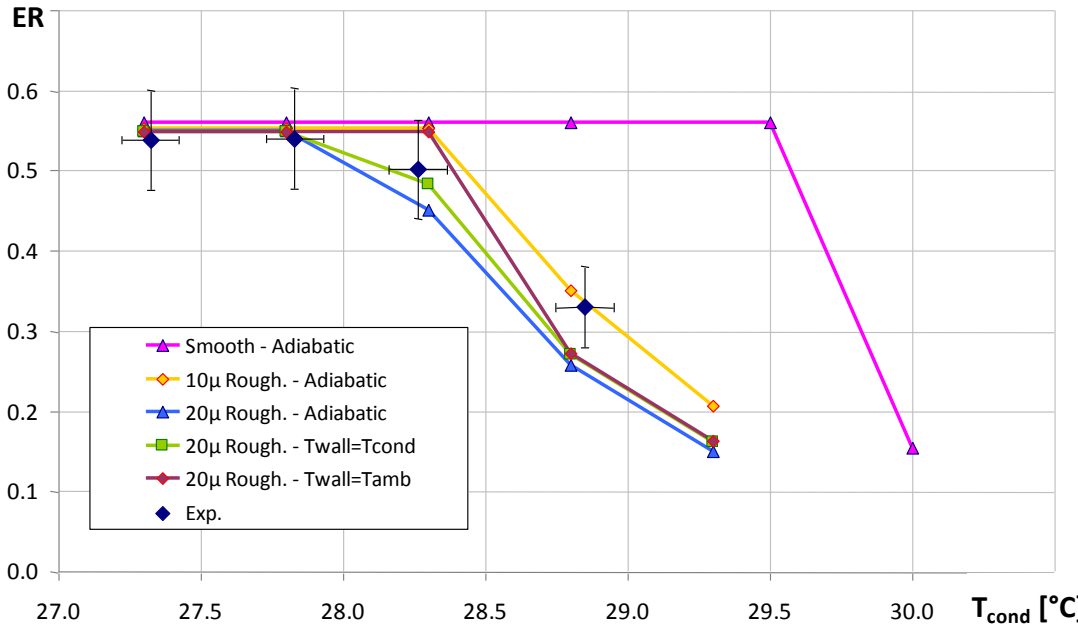

Fig. 4.3 – ER profiles for different values of wall roughness and temperature; T_{gen}=89°C, T_{eva}=5°C

[13] It should be noticed however, that the ejector's walls are made of aluminum which has high values of longitudinal conductivity. Therefore, the hypothesis of constant wall temperature may not be so approximated.

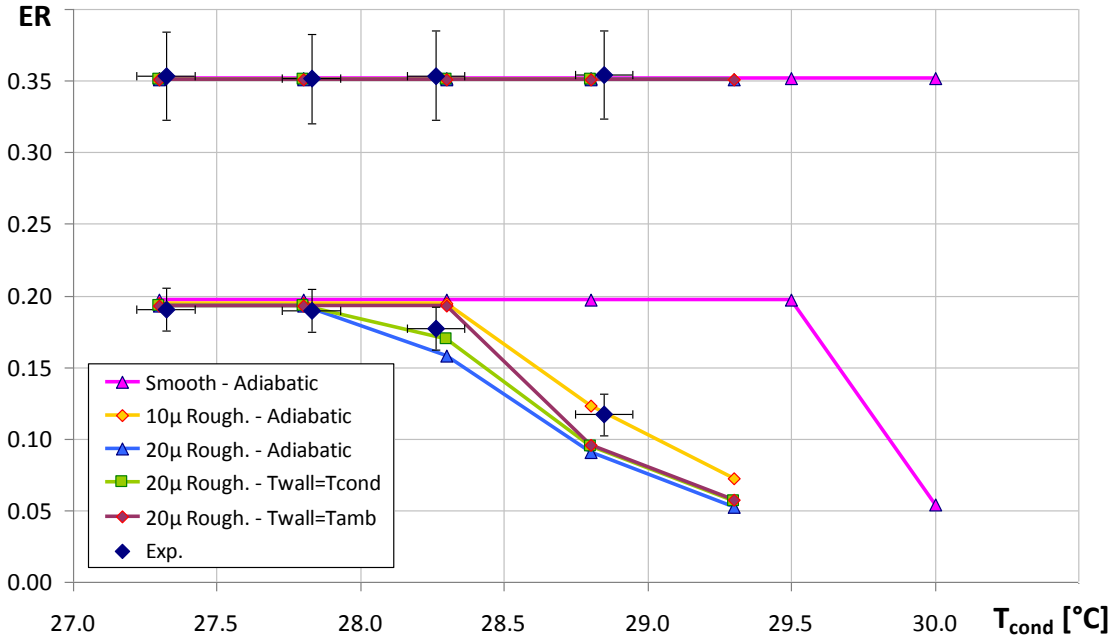

Fig. 4.4 – Primary and Secondary mass flow rates for different values of wall roughness and temperature; T_{gen}=89°C, T_{eva}=5°C

Fig. 4.5 presents the profiles of Heat Transfer Coefficient (HTC) at the ejector external wall. As expected, the heat transfer increases with increasing surface roughness. Moreover, the location of the maximum peak in HTC is always after the mixing section throat (*x~272 mm*) and downstream of the diffuser shock (which is visible by the presence of wiggles in the HTC curves). This may be due to the strong mixing occurring after any supersonic shock (Gatsky and Bonnet, 2013). In any event, it is clear that even in the most conservative case (i.e., smooth wall and wall temperature equal to the condenser temperature), the ejector surface cannot be considered adiabatic. Indeed, values like those reported in Fig. 4.5 are typical of the heat transfer of liquids in forced convection. This effect may impact somewhat the accuracy of the numerical simulations by changing the starting position and shape of the transition process, as can be seen in Fig. 4.3 or Fig. 4.4.

In addition to these numerical considerations, the heat loss toward the environment is a feature that must be taken into account for a correct sizing of the condenser. Overall, the heat loss through the ejector external wall is always between 2 and 5kW in our simulations. This can hardly be considered a negligible quantity as it represents the 2-4% of the total heat rejected at condenser.

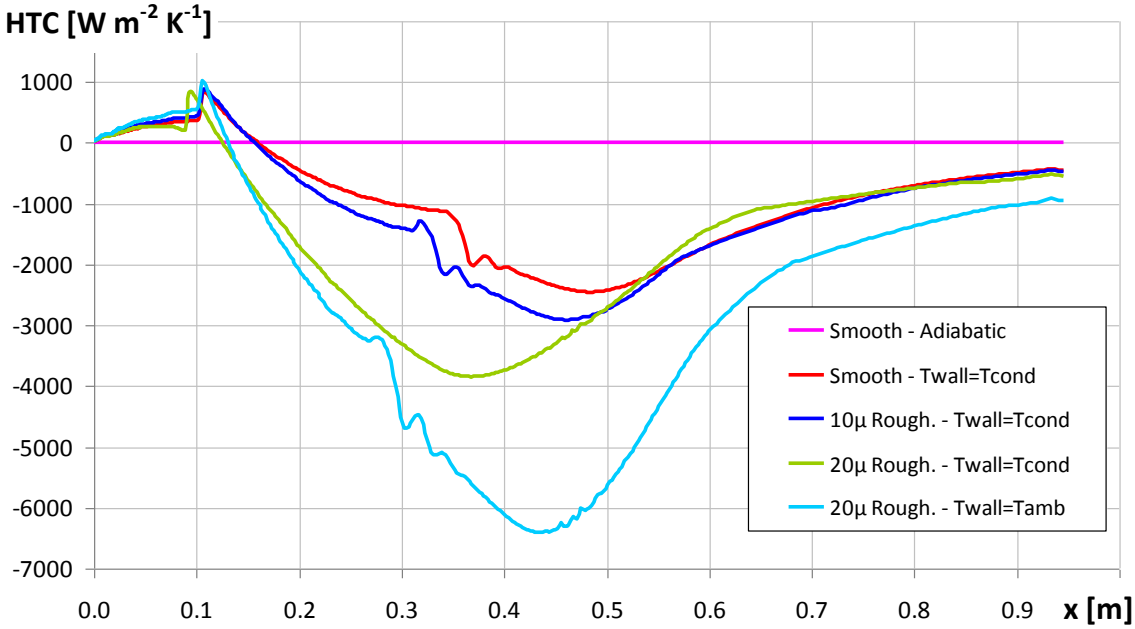

Fig. 4.5 – Heat Transfer Coefficient profiles on the mixing chamber/diffuser wall for various case with smooth and rough walls, original and adapted grids; T_{gen}=89°C, T_{eva}=5°C, T_{cond}=28.3°C

Fig. 4.6 shows the comparison between the static pressures measured along the diffuser wall and the corresponding profiles obtained by numerical simulations (the uncertainties on the pressure measurements are calculated with the same procedure described in Appendix A). Clearly, the calculated pressure profiles are highly dissimilar for different roughness heights. In particular, the curves corresponding to smooth surfaces are very distant from the experimental data (this is not true at the extremes of the curves where the pressure boundary conditions are imposed equal to the experiments).

By focusing on the case with T_{cond}=*28.3°C*, it can be noted that, in much the same way as for the ER, the curve of 20µm roughness height is the one that more closely reproduces the experimental data. In particular, the curves with lower roughness height still predict choked flow and, consequently, the presence of the shock in the diffuser (indicated by the steep rise in wall pressure).

Hence, it can be inferred that the equivalent "sand-grain roughness height" of the ejector, as predicted by numerical analysis, should be close to 20 µm. Converting this value through the aforementioned conversion factors gives an estimated arithmetic roughness height, $K_{a,}$ of around 3.5 µm. The roughness of the ejector surface was subsequently measured in different locations by means of a Mahr contact surface profilometer. Resulting values of K_a ranged from 4 to 6 microns depending on the different measurement sites.

By comparing this value with that predicted by CFD, it seems that numerical analysis underestimates somewhat the experimental datum. Although this error may be partly due to numerical and experimental approximations, one must not forget the large uncertainty connected to the definition of conversion factor between different roughness heights (Adams *et al.*, 2012).

As a concluding remark, this analysis highlights the importance of the manufacturing process on the performance of a supersonic ejector refrigerator. Friction losses are obviously neither the only, nor the greatest source of losses inside the ejector (e.g., shocks, mixing and possible recirculations). Nevertheless, with a relatively small economic outlay (i.e. by polishing the internal surfaces) significant advantage could be gained in terms of efficiency. In this respect, it is important to note the large size of the ejector under study, which is designed to produce around 40kWf of nominal cooling power. These dimensions are larger than those commonly found in the literature (see Tab. 2.4). Therefore, the impact of wall roughness on ejector efficiency should be expected to be much greater for systems with smaller size.

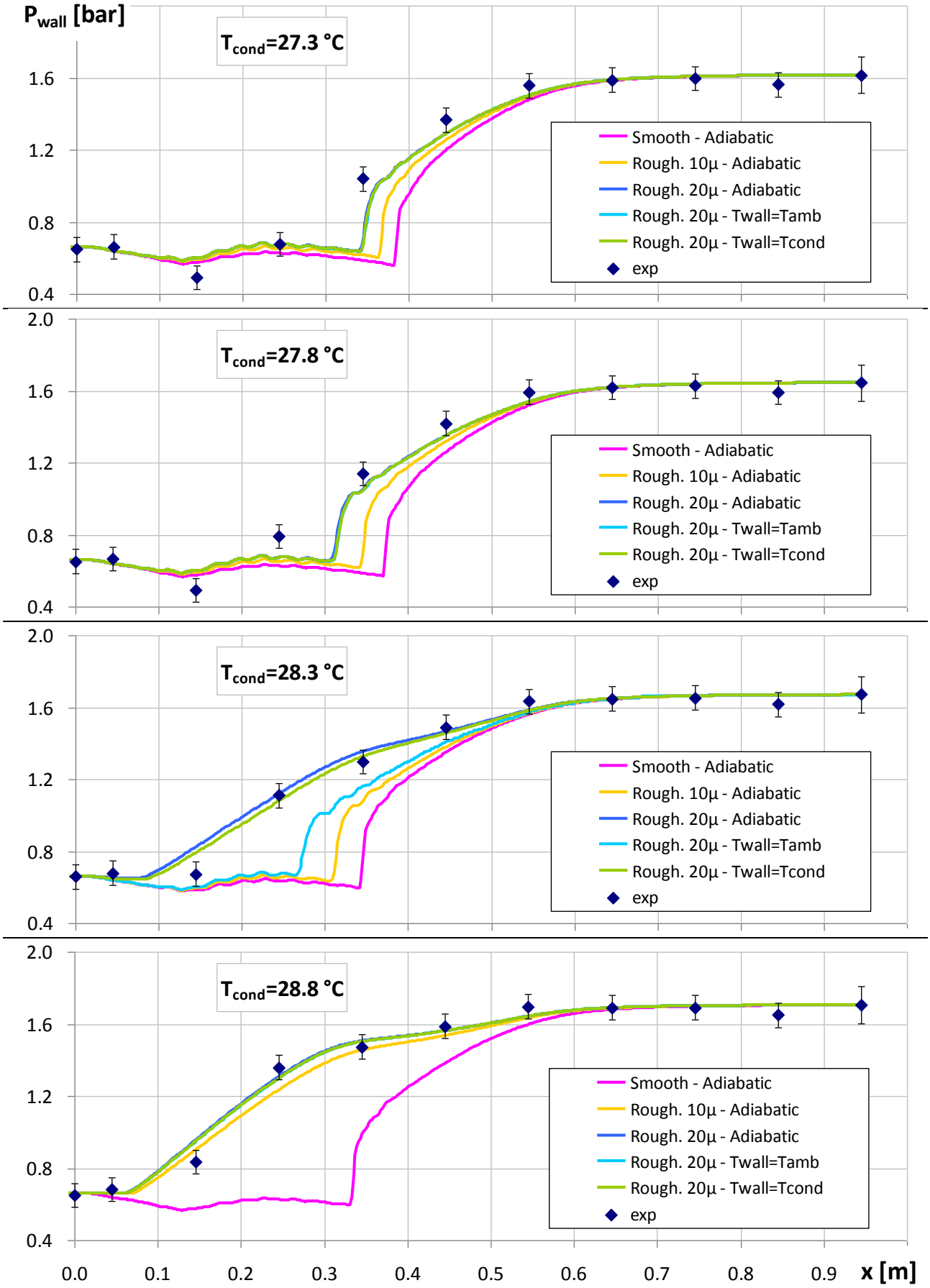

Fig. 4.6 – Pressure profiles at the mixing chamber/diffuser wall, for different values of wall roughness and temperature; T_{gen}=89°C, T_{eva}=5°C, varying T_{cond}

4.2 Analytical modeling: the Mixing Layer Model

It is custom use in ejector research to model ejector dynamics by means of the Q1D approximation (for a review of ejector modeling see for example He *et al.*, 2009). Mass, energy and momentum balances are applied in various key sections in order to exploit all the available information on the geometry and flow conditions. In many cases, the idea of a secondary flow choke section, proposed by Munday and Bagster (1977), is used to explain the blockage of the entrainment ratio with respect to a decreasing back pressure (i.e. the appearance of the plateau line). Although the concept effectively allow calculation of the maximum suction mass flow rate (Eames *et al.*, 1995; Huang *et al.*,1999), modern numerical analyses show that the choking of the secondary fluid is not a well localized phenomenon (as for primary nozzle choke), but rather a gradual acceleration of secondary fluid particles to sonic conditions due to momentum exchange (see sonic line patterns in Fig. 2.7 or in Bartosiewicz *et al.*, 2005; Al-Ansary and Jeter, 2004).

Moreover, internal losses are usually evaluated by means of simple efficiency parameters. These terms are most of the time constant values adjusted upon experimental data. This approach may produce reasonable results when dealing with analysis of specified ejectors (the ones through which the efficiencies have been calibrated) but it is inconsistent when facing design optimization, where the losses are unknown functions of the unknown geometry.

The model that is proposed next builds on a previous scheme devised by Papamoschou (1993, 1996) and is able to compute all flow properties inside an axisymmetric or planar mixing chamber with either constant or variable cross section. The amount of secondary flow entrainment, the work and heat exchange between the two streams, pressure losses and mixing efficiency are computed as a function of the system geometry and without use of any arbitrary parameter. Consequently, this model is particularly suited for a thermodynamic optimization of the ejector system and could be used as a fast tool to make preliminary explorations of the design space. To date, the model is restricted to the region of the mixing chamber, but studies are being performed to extend the same scheme to the complete ejector geometry.

The model is based on the application of the Q1D conservation equations on two control volumes that surround the primary and secondary stream separately. The two control volumes are delimited by the "dividing streamline". This is the line that separates the two fluid regions having mass flow rates correspondingly equal to those of primary and secondary streams. The division is purely virtual because the two flows actually mix inside the ejector. However, on a time-averaged basis the separation is meaningful and can be computed by the knowledge of the average density and velocity profiles along any ejector cross section (it suffices to integrate their product up the value of the primary or secondary mass flow rates). The control volumes for the primary and secondary stream are illustrated in Fig. 4.7.

Once the location of the dividing streamline is computed, the shear stress, shear work and heat transfer across it, as well as friction at wall, can be evaluated by means of experimental correlations, as will be detailed shortly. In what follows just a brief derivation of the main equations is shown, more details can be found in Grazzini *et al.* (2015).

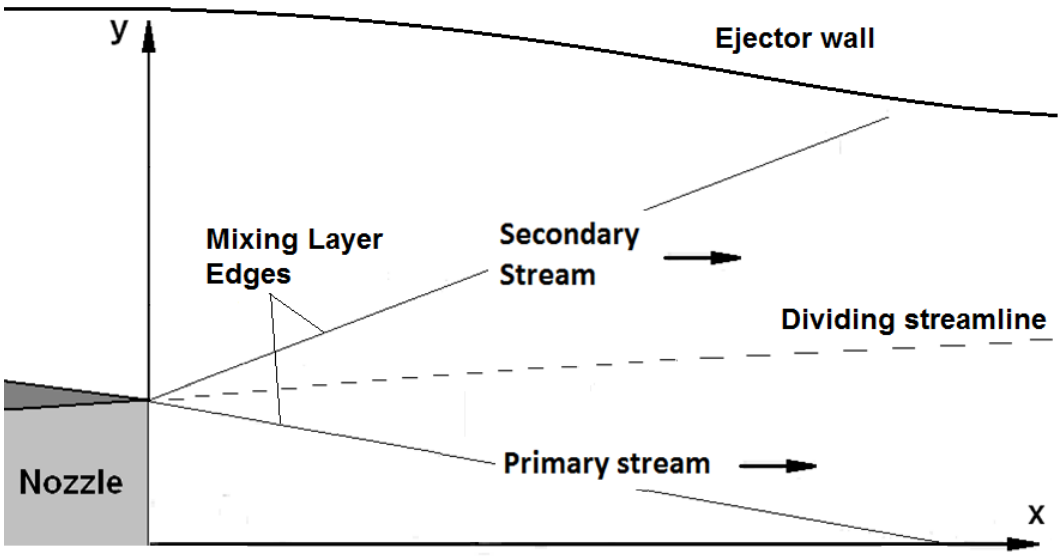

Fig. 4.7 – Illustration of the two control volumes for the Mixing Layer Model. The secondary stream is bounded by the ejector wall and dividing streamline, the primary stream is limited by the axis of symmetry and dividing streamline.

The mixing layer flow inside a supersonic ejector is well approximated by the 2D compressible boundary layer equations (Schlichting, 1979). For the planar case, it could be shown by dimensional arguments that these reduce to (Smits and Dussauge, 2006):

$$\frac{\partial \overline{\rho}\widetilde{u}}{\partial x}+\frac{\partial \overline{\rho}\widetilde{v}}{\partial y}=0$$
$$\overline{\rho}\widetilde{u}\frac{\partial \widetilde{u}}{\partial x}+\overline{\rho}\widetilde{v}\frac{\partial \widetilde{u}}{\partial y}=-\frac{\partial \overline{p}}{\partial x}+\frac{\partial \tau}{\partial y} \qquad \text{eq. 4-1}$$
$$\overline{\rho}\widetilde{u}\frac{\partial \widetilde{H}}{\partial x}+\overline{\rho}\widetilde{v}\frac{\partial \widetilde{H}}{\partial y}=\frac{\partial}{\partial y}\left[w+q\right]$$

Where the straight bars over the symbols indicate Reynolds average while the tilde implies Favre average; τ, w and q are respectively the total (i.e., viscous + turbulent) shear stress, shear work (per unit time and area) and heat transfer.

As anticipated, a system of Quasi-One-Dimensional conservation equations is applied separately to each of the two streams. Although the flow inside an ejector cannot be considered as 1D (and in general, all shear layer flows are at least two-dimensional), the 2D effects are retained by the use of two corrective parameters that will be introduced later.

The use of Q1D approximation brings about many benefits: first, it provides a set of equations that can be solved in a much easier way than the "integral methods" needed to compute the full 2D equations (see for example Hickman *et al.*, 1972; Rajaratnam, 1976); second, it allows for an easy connection with primary nozzle and diffuser equations (as these regions can legitimately be regarded as Q1D) to build a compact and coherent model of the complete ejector; last, by means of the Q1D approximation, the ejector can be seen as an equivalent "momentum exchanger" and many interesting conclusion can be drawn about the thermodynamic optimization of the system (see chapter 4.4).

In order to derive the Q1D system of equations, eq. 4-1 must be integrated over the cross sectional area. After some algebra (see Grazzini *et al.*, 2015), it can be shown that the governing equation become:

$$
\begin{aligned}
&d\left(\rho\langle u\rangle A\right)=0\\
&d\left(\rho\left\langle u^2\right\rangle A\right)+d\bar{p}=\left(\tau_e-\tau_i\right)dS\\
&d\left(\rho\left\langle u^3\right\rangle A\right)+d\left(\rho\langle u\rangle hA\right)=\left(w_e+q_e\right)dS-\left(w_i+q_i\right)dS
\end{aligned}
\qquad \text{eq. 4-2}
$$

where the subscripts *i* and *e* stand for internal and external surfaces surrounding the control volume (e.g., the wall and the dividing streamline for the secondary stream).
In the last equations all the quantities are averaged over the cross sectional area. For clarity however, all the average symbols have been dropped except those related to the average velocities. This was made because it is important to notice that two additional variables appear in eq. 4-2, namely the "averaged squared velocity" and "averaged cubed velocity". These two terms concentrates the non-uniformities or 2D effects of the mixing layer and can only be calculated if the entire velocity profile is known at each cross section.
In order to make this point clearer, two "shape coefficients" may be defined as follows:

$$
\alpha=\frac{\left\langle u^2\right\rangle}{\langle u\rangle^2}=\frac{\int_y\bar{\rho}\tilde{u}^2dy}{\int_y\bar{\rho}dy}\cdot\left[\frac{\int_y\bar{\rho}dy}{\int_y\bar{\rho}\tilde{u}dy}\right]^2
\qquad
\beta=\frac{\left\langle u^3\right\rangle}{\langle u\rangle^3}=\frac{\int_y\bar{\rho}\tilde{u}^3dy}{\int_y\bar{\rho}dy}\cdot\left[\frac{\int_y\bar{\rho}dy}{\int_y\bar{\rho}\tilde{u}dy}\right]^3
\qquad \text{eq. 4-3}
$$

In the simple case of a uniform velocity profile, i.e. for 1D flow, the average velocity is constant and can be taken out of the integrals. Hence, the shape coefficients become equal to one and the number of variable in eq. 4-2 diminishes by two. This is because the "averaged squared velocity" and "averaged cubed velocity" becomes equal to the "averaged velocity" squared and cubed.
Unfortunately, this approximation is only valid in certain kind of flow, most importantly for fully developed turbulent flow inside constant section channels (as long as the small non uniformities due to the boundary layer are neglected) or in channels with slow area variations (e.g. Q1D flows). The approximation is no longer valid in case of large non uniformity of the velocity profiles due to the presence of shear flows like mixing layers, jets and wakes. In these cases the flow is actually 2D and the two abovementioned additional variables do not allow closure of the system of equations.
Nevertheless, the problem may be worked around by the use of the two "shape coefficients". After introducing these parameters, the governing equations, complemented by the perfect gas equation of state, become:

$$
\begin{aligned}
&d\rho uA=0\\
&d\left(\alpha\rho u^2A\right)+dp=\left(\tau_e-\tau_i\right)dS\\
&d\left(\beta\rho u^3A+\rho uAh\right)=\left(w_e+q_e\right)dS-\left(w_i+q_i\right)dS\\
&dp=d\rho+dT
\end{aligned}
\qquad \text{eq. 4-4}
$$

In order to integrate eq. 4-4 the shape coefficients as well as the shear stress, shear work and heat transfer must be known on each surface surrounding the primary and secondary streams. The ways to calculate these quantities are analyzed one by one below.
Following Papamoschou (1993), the shear stress at wall is computed is computed as follows:

$$\tau_w = c_f \frac{1}{2} \rho_\infty U_\infty^2 \qquad \text{eq. 4-5}$$

where c_f is the skin friction coefficient that is computed through Van Driest correlation for compressible boundary layer on smooth walls (Schlichting, 1979):

$$0.242 \sqrt{\frac{1-\lambda^2}{c_f}} \frac{\sin^{-1}(\lambda)}{\lambda} = \log_{10}\left(\mathrm{Re}_x c_f\right) + 1.26 \log_{10}\left(1-\lambda^2\right)$$
$$1-\lambda^2 = \left(1 + \frac{\gamma-1}{2} M_\infty^2\right)^{-1} \qquad \text{eq. 4-6}$$

where Re_x is the Reynolds number based on streamwise distance x.
The shear stress on the dividing streamline is computed by means of the maximum shear stress formulation, eq. 3-7. This is possible because Townsend (1976) showed that the maximum shear stress inside a constant pressure mixing layer occurs approximately on the dividing streamline.
In order to compute the heat transfer across the dividing streamline, the turbulent Prandtl number is introduced as follows:

$$P_t = \frac{\mu_t C_p}{k_t} \qquad \text{eq. 4-7}$$

where μ_t and k_t are the turbulent dynamic viscosity and conductivity. C_p is the specific heat capacity at constant pressure.
A major simplification is obtained by considering that the turbulent Prandtl number is unity. This is known as Strong Reynolds Analogy (SRA) and amounts to say that the heat and momentum transfer by turbulent fluctuations are driven by the same transport mechanisms. In case of mixing layers, a better approximation is to consider $P_t \approx 0.77$ (Smits and Dussauge, 2006; Schlichting, 1979) [14]. The use of the Reynolds Analogy allows computing the heat transfer by the knowledge of the turbulent shear stress on the dividing streamline:

$$q_t = \frac{\mu_t C_p}{P_t} \frac{\partial \tilde{T}}{\partial y} = \frac{C_p}{0.77} \frac{\partial \tilde{T}}{\partial y} \frac{\partial y}{\partial \tilde{u}} \tau_t \approx \frac{C_p}{0.77} \frac{\Delta T_\infty}{\Delta U_\infty} \tau_t \qquad \text{eq. 4-8}$$

The only terms missing are now the shear work and the shape coefficients. These quantities may be computed once a profile is assumed for the density and velocity inside the mixing layer.
Some experiments have shown that in fully developed mixing layers the shape of the velocity profile is virtually unaffected by compressibility (Smits and Dussauge, 2006; Gatsky and Bonnet, 2013). This means that compressibility affects the spreading rate of the layer while maintaining the velocity distribution unaltered. Therefore, it is possible to use fitting curve derived for incompressible flows in order to describe the velocity distribution of the compressible case. Unfortunately, there are many different possibilities depending on the type of fitting curve (e.g. error function or hyperbolic tangent) and thickness definitions (e.g. vorticity thickness, velocity thickness, etc…). Barone *et al.* (2006) make a clear

[14] This approximation is valid regardless of the nature of the fluid, because the turbulent Prandtl number depends solely on the structure and characteristic of turbulence.

comparison of many of these different solutions. One of these exploits a hyperbolic tangent distribution based on the vorticity thickness:

$$U = U_{\infty 2} + \frac{U_{\infty 1} - U_{\infty 2}}{2}\left[1 + \tanh\left(2.002 \cdot \frac{y - y_0}{\delta_\omega}\right)\right] \qquad \text{eq. 4-9}$$

Where y_0 is the mixing layer centerline, i.e., the location where the velocity is equal to the average of the two external isentropic velocities.
In order to reach workable formulations for the shear work and shape coefficients, we make a further simplification and consider a linear approximation of the hyperbolic tangent profile (this corresponds to the first order truncation of the Taylor expansion):

$$U_{sl} \approx U_{\infty 2} + \frac{\Delta U_\infty}{2}\left(1 + 2.002 \cdot \frac{y - y_0}{\delta_\omega}\right) \approx U_{\infty\_ave} + \frac{\Delta U_\infty}{\delta_\omega} y \qquad \text{eq. 4-10}$$

where it is assumed that the origin of the coordinate system is on the mixing layer centerline and that the primary flow lies below the longitudinal axis.
For a linear profile, the derivates of the axial velocity along the mixing layer is constant and the vorticity thickness immediately gives an estimation of the shear layer thickness:

$$\delta_\omega = \Delta U_\infty \Big/ \left(\frac{\partial U}{\partial y}\right)_{\max} \approx \Delta Y_{sl} \qquad \text{eq. 4-11}$$

By further assuming that the layer spread symmetrically with respect to the position of the dividing streamline, the edges of the mixing layer are found by adding and subtracting one half of the vorticity thickness to the dividing streamline location (Papamoschou, 1996). Moreover, the velocity at the dividing streamline can be easily computed and the shear work becomes:

$$w_t = \tilde{u}_{dsl}\tau_t \approx U_{\infty\_avg}\tau_t = \frac{U_{\infty 1} + U_{\infty 2}}{2}\tau_t \qquad \text{eq. 4-12}$$

Finally, in order to calculate the shape coefficients, eq. 4-3, the velocity and density profiles must be computed at each cross section. A major simplification is obtained by assuming that the density variation inside the mixing layer is negligible with respect to the velocity variation. Under this condition, the density can be eliminated in eq. 4-3 and a closed form expression for the shape coefficients can be found. For the planar configuration these are given by:

$$\alpha_x = \frac{\langle U_x^2 \rangle}{\langle U_x \rangle^2} = \frac{4}{3}\delta_{tot\_x}\frac{\left[3U_{\infty\_x}^2\left(\delta_{tot\_x} - \delta_{sl\_x}\right) + \left(U_{dsl}^2 + U_{\infty\_x}U_{dsl} + U_{\infty\_x}^2\right)\delta_{sl\_x}\right]}{\left[2U_{\infty\_x}\left(\delta_{tot\_x} - \delta_{sl\_x}\right) + \left(U_{dsl} + U_{\infty\_x}\right)\delta_{sl\_x}\right]^2}$$

$$\beta_x = \frac{\langle U_x^3 \rangle}{\langle U_x \rangle^3} = 2\delta_{tot\_x}^2\frac{\left[4U_{\infty\_x}^3\left(\delta_{tot\_x} - \delta_{sl\_x}\right) + \left(U_{dsl}^3 + U_{dsl}^2U_{\infty\_x} + U_{dsl}U_{\infty\_x}^2 + U_{\infty\_x}^3\right)\delta_{sl\_x}\right]}{\left[2U_{\infty\_x}\left(\delta_{tot\_x} - \delta_{sl\_x}\right) + \left(U_{dsl} + U_{\infty\_x}\right)\delta_{sl\_x}\right]^3} \qquad \text{eq. 4-13}$$

Where x can be either 1 or 2, meaning the primary or secondary flow; δ_{sl} is the part of the shear layer thickness related to the primary or secondary stream; δ_{tot} represents the total thickness of the primary or secondary flow (isentropic plus shear region).
At the beginning of this chapter, it was mentioned that a basic assumption for the model is that the mixing occurs at constant pressure. This condition is required by many of the correlation presented and is needed to find the position of the dividing streamline (see Grazzini *et al.*, 2015, Papamoschou 1993, 1996). By further assuming that the density of the two streams is approximately equal, we are implicitly imposing the same inlet static state for the primary and secondary streams. However, this restriction should not be regarded as a mere simplifying assumption, but rather as an optimal operating condition. The only energy exchange that is useful for the purpose of an ejector chiller is the mechanical energy transfer between the primary and secondary stream. By imposing the same static conditions, the entropy generation due to heat transfer mechanism and shock adaptations are reduced to a minimum.
In conclusion, it is important to point out that the need for a shape coefficient derives from the attempt of applying a Q1D model to a flow that is actually 2D. This kind of flow may be solved by use of "integral methods" as long as the profiles of the velocity and of the other quantities are known (Hickman *et al.*, 1972; Rajaratnam, 1976). The method illustrated here can be considered to lie somewhere between a pure Q1D scheme and a 2D integral method. Information on the calculation procedure can be found in Grazzini *et al.* (2015).

4.3 Model validation

Comparison with CFD simulations are performed for a constant area axisymmetric mixing chamber of 0.4 meter length, with a radius of 54 mm. The working fluid is air. The length of the chamber was selected in order to model the sole region of free mixing layer, i.e., the region where the shear layer has reached neither the axis of symmetry nor the mixing chamber wall. In the first case, the primary isentropic region ceases to exist and a "jet type" of flow begins. In the second case, the secondary isentropic region ends and a new flow regime, that we may call "confined mixing layer", begins. In both cases the Q1D model is unable to compute the shear stress on the dividing streamline (because the isentropic velocities and densities are undefined) and the program stops. Future work will be directed to extend the calculations to these types of flows in order to realize a complete model of the ejector.
Simulations are performed using the commercial CFD package ANSYS Fluent v15, which is based on a finite volume approach. The details of the numerical scheme, as well as its validation, are described thoroughly in (Mazzelli and Milazzo, 2015). In brief, the main characteristics of the scheme are as follows:

- density-based implicit solver, second order accurate,
- structured grid of around 45k elements
- y+ <1 at the mixing chamber wall
- kω SST turbulence model with Enhanced Wall Treatment,
- ideal gas equation of state and adiabatic walls

In addition, a slip wall conditions was imposed at the primary nozzle walls. This is done in order to focus the comparison on the sole mixing zone (as such, both Q1D and CFD primary nozzle expansion are considered completely isentropic). On the contrary, the wall friction along the mixing chamber is evaluated through low Reynolds models for the CFD and by means of eq. 4-6 for the Q1D model.

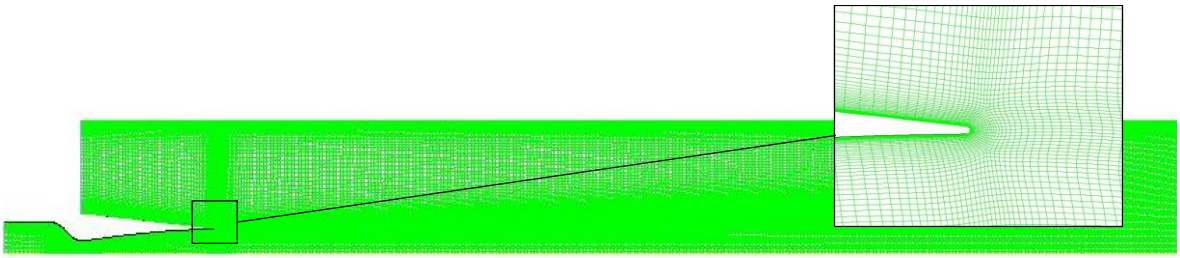

Fig. 4.8 – Computational domain for the validation of the Mixing Layer Model

Tab. 4.1 shows the boundary conditions of the 4 cases tested. These were selected in order to guarantee the matching of the static state between the primary and secondary stream. The value of outlet pressure is raised from one case to another in order to test the model with increasingly challenging conditions. In order to correctly compare the results of the Q1D model with those from CFD calculations, a macro was built that extracts the local CFD data for several cross sections. These data are processed to compute the same average quantities that are calculated by the Q1D model.

	Unit	Case 1	Case 2	Case 3	Case 4
T_{01} – inlet	*°C*	*360*	*385*	*410*	*440*
T_{02} – inlet	*°C*	*0*	*0*	*0*	*0*
P_{01} – inlet	*kPa*	*1285*	*1435*	*1642*	*1900*
P_{02} – inlet	*kPa*	*66,2*	*66,2*	*66,2*	*66,2*
P – outlet	*kPa*	*44*	*50*	*58*	*66*

Tab. 4.1: Boundary conditions for the 4 tested cases

The results in terms of mass flow rates for the four cases are reproduced in Tab. 4.2. In general, results for the first three cases show a good agreement, with errors that grows with increasing pressure gradient. In particular, Q1D results for the last case appear to be completely in error with respect to CFD data. The reason for this discrepancy is the formation of a recirculation region near the ejector exit that considerably reduces the secondary stream mass flow rate and alters the pressure trends.

		Case 1			Case 2			Case 3			Case 4		
Variable	**Unit**	**Q1D**	**CFD**	**%Err.**	**Q1D**	**CFD**	**%Err.**	**Q1D**	**CFD**	**%Err.**	**Q1D**	**CFD**	**%Err.**
m_1	*kg/s*	*0.168*	*0.168*	*0.4*	*0.184*	*0.184*	*0.3*	*0.207*	*0.206*	*0.3*	*0.234*	*0.234*	*0.3*
m_2	*kg/s*	*1.395*	*1.359*	*2.7*	*1.318*	*1.283*	*2.8*	*1.135*	*1.068*	*6.3*	*0.851*	*0.475*	*79.1*
ER	-	*8.3*	*8.1*	*2.3*	*7.2*	*7.0*	*2.4*	*5.5*	*5.2*	*5.9*	*3.6*	*2.0*	*78.6*

Tab. 4.2: Comparison of theoretical and numerical final results for the various cases

Fig. 4.9 shows the dividing streamline and shear layer edges for case 1. The edges for CFD results are calculated by the same method as explained for the Q1D in the previous chapter. Although the agreement appear to be quite satisfactory, it is important to point out that the illustrated trends represent a rough approximation of the real shear layer. In particular, the assumption of a linear velocity profile causes an underestimation of the actual shear layer thickness. A better estimation can be obtained by means of different thickness definitions or by releasing the linear approximation in favor of a more appropriate hyperbolic tangent velocity profile.

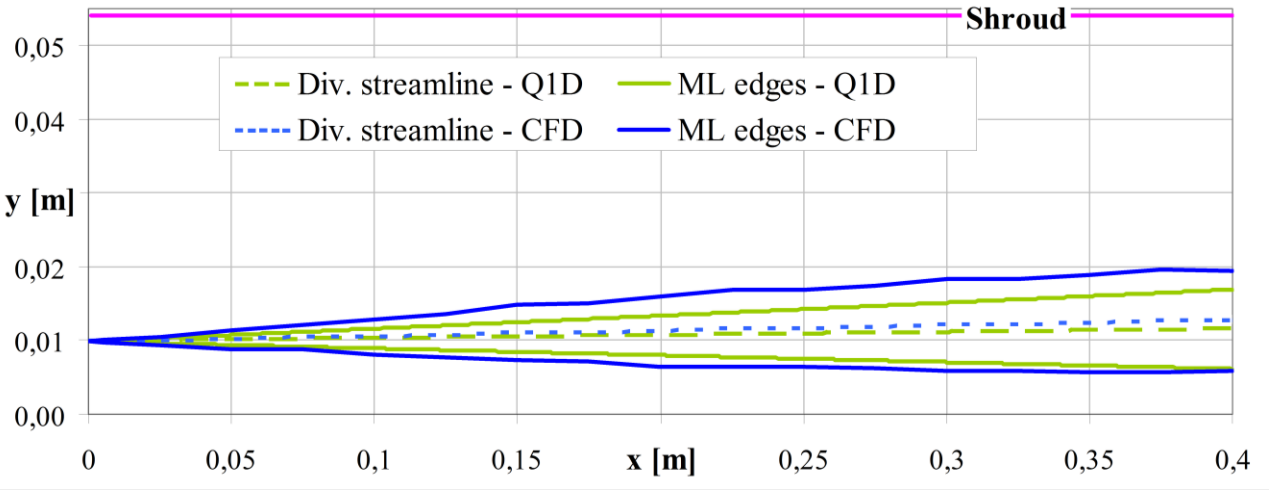

Fig. 4.9: Mixing layer edges and dividing streamline for case 1

Fig. 4.10 from *a* to *c* show the results in terms of Mach, velocity, temperature and density variations. The oscillations of the CFD results for the primary streams are due to the presence of subsequent trains of expansions and shocks of the supersonic primary stream. These come from small residual pressure gradients due to an imperfect matching of the pressure conditions. Although in principles these could be reduced, in practice it is impossible to perfectly match the pressure conditions as gradients are produced internally by the strong shear exchange (this is also the cause of the turbulence production which allows for intense mixing between the two streams). Fig. 4.10*c* shows that the density is approximately constant and equal for the two streams, partly validating the hypothesis made in the previous chapter for the calculations of the shape profiles. The greatest departure between the two methods is seen for the results related to the primary stream Mach number, where the data for Q1D model are quite above those from CFD results. The reason for this error becomes clear by looking at Fig. 4.11, which shows the variation of the shear stress at wall and on the dividing streamline.

The Q1D model underestimates the shear stress by around 30% with respect to CFD data. This causes a lower momentum transport from the primary to the secondary stream. Moreover, being the primary mass flow rate much lower than that of secondary flow, this error impacts almost exclusively the primary velocity. Conversely, results for the shear stress at wall show an excellent agreement with CFD results. This is important in that it demonstrates that the main source of error comes almost exclusively from the modeling of the momentum exchange along the dividing streamline.

In particular, the lower shear stress predicted by the Q1D model is most likely due to excessive turbulence suppression by the compressibility correction, eq. 3-6. Although this could be calibrated to better match the numerical data, nevertheless, it is important to note that CFD turbulence models are themselves unable to correctly predict the impact of compressibility on the shear layer turbulence. In particular, the shear stress in conventional CFD schemes are also calculated by means of ad-hoc corrections of the turbulence model equations. Barone *et al.* (2006) compared several of these corrections and found that the one proposed by Wilcox (1992), and used in this work, gave the best results, but the error was still around 12%. Therefore, a more reliable comparison and calibration of the model should be carried out by comparing the Q1D results directly with experimental data.

Finally, Fig. 4.11 shows that the numerical shear stress at the entrance of the mixing chamber is almost zero. This is due to the presence of a developing region of the mixing layer. After a distance of around 5 mm the shear layer turbulence has grown to its fully turbulent state and viscous effects becomes negligible. This phenomenon cannot be captured by the Q1D as the correlation for the shear stress, eq. 3-7, is valid only in the region of fully developed turbulent mixing layer.

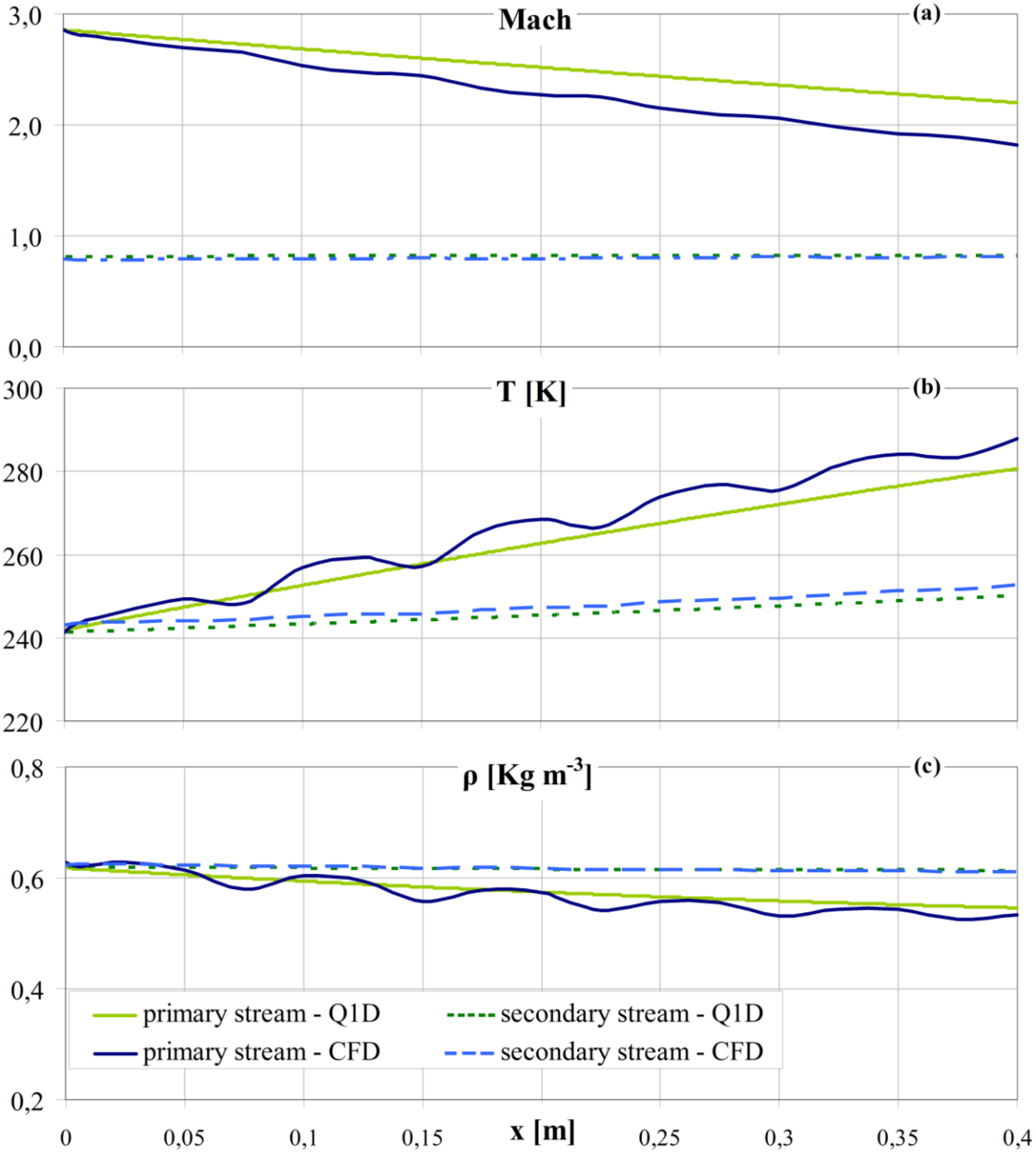

Fig. 4.10: Mach (a), temperature (b) and density profiles (c) along the mixing chamber for case 1

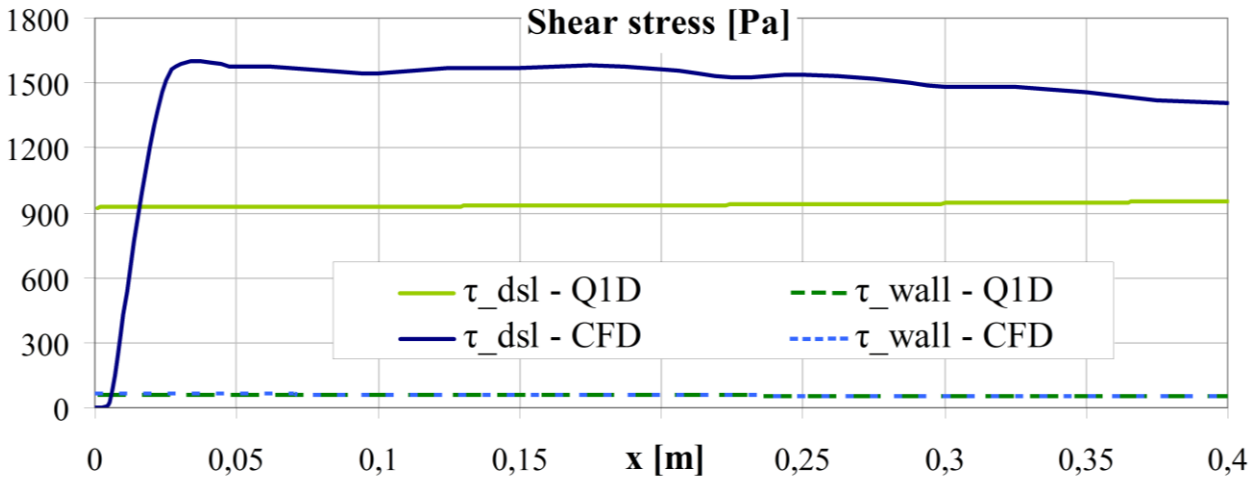

Fig. 4.11: Shear stress on the dividing streamline (left axis) and at wall (right axis) for case 1

4.4 Mixing Optimization

In order to optimize the mixing inside a supersonic ejector, the momentum exchange must be maximized while reducing irreversibilities. Sources of losses inside the mixing chamber include heat exchange between the two streams, supersonic shocks, friction and heat losses at wall, turbulence production and dissipation. As already discussed in previous sections, the first two sources can be minimized by matching the inlet static states of the two streams. As for friction losses, benefits can be achieved by reducing the wall roughness and by decreasing the mixing chamber length. In turn, short mixing chambers can be obtained by increasing the mixing effectiveness, i.e., by increasing the mixing layer spreading rate and shear stress.

There have been a number of attempts to increase the mixing rate by methods of mixing enhancement such as vortex generators, tripped boundary layers, swirlers and cross blowing (Smits and Dussauge, 2006). However, in many cases it is unclear whether the benefits are worth the additional pressure losses. Looking back at the equation defining the spreading rate, eq. 3-5, larger values of this quantity can be achieved by:

1. increasing the free stream density ratio (this means having the secondary stream density *greater* than the primary stream density, $\rho_{\infty 2} > \rho_{\infty 1}$),
2. decreasing the free stream velocity ratio (this means having the secondary stream velocity *lower* than that of the primary flow, $u_{\infty 2} << u_{\infty 1}$),
3. decreasing the convective Mach number.

In case of constant pressure mixing of a pure gas, increasing the density ratio would translate in larger temperature difference, thus resulting in heat transfer losses. As for the velocity ratio, the speed of the secondary stream should always be the least possible (see chapter 3.1). This can be achieved by controlling the pressure along the mixing chamber, which must be as close as possible to the secondary stream total pressure (the Q1D model could be exploited for this purpose as it permits quick calculations of many different mixing chamber profiles).

The problem becomes more complicated for the primary stream velocity, as will be detailed below.

In the simplified case of constant pressure and temperature mixing of a single gas, the speed of sound of the two streams are approximately the same (this is true just at the beginning of the mixing region while at farther distances temperatures will change due to the slow down or acceleration of the streams, see figure Fig. 4.10*b*). In this case, the convective Mach number becomes:

$$M_c = \frac{\Delta U_\infty}{a_{\infty 1} + a_{\infty 2}} \approx \frac{M_{\infty 1} - M_{\infty 2}}{2}$$ **eq. 4-14**

If we further assume that secondary stream velocity is negligible with respect to primary speed, the shear layer spreading rate, eq. 3-5, simplifies to:

$$\delta'_\omega = 0.085 \cdot \left[0.25 + 0.75 e^{-0.75 M_{\infty 1}^2}\right]$$ **eq. 4-15**

which is a monotonically decreasing function of the primary stream Mach number.
Therefore, increasing the primary stream speed necessarily causes a reduction of the spreading rate. A reduction of the primary stream Mach number may be obtained by decreasing the inlet primary total pressure. However, if the primary total pressure is lowered, the amount of mechanical energy entering the ejector decreases and the critical pressure and refrigeration load are abated. This can be avoided by increasing the primary mass flow rate. In turn, this leads to a reduction of contact surface per unit volume of the primary flow that again reduces the mixing effectiveness inside the mixing chamber.
One way to overcome these limitations is represented by the optimization of the shear surfaces between primary and secondary streams by considering, for instance, new design configurations of the primary nozzle, e.g., annular primary nozzle (Kim *et al.* 2006), petal nozzles (Srikrishnan *et al.*, 1996) and multiple nozzles (Chandrasekhara *et al.* 1991). This last solution basically consists in a partition of the primary mass flow rate that is deviated among many smaller nozzles, whose sizes and positions must be carefully designed.
In order to demonstrate these concepts, a simple optimization was tried for a planar mixing chamber of 0.4x0.4x0.2m length, height and width respectively. By keeping the boundary conditions fixed, the primary stream was allowed to flow through an increasing number of primary nozzles (1, 2 and 4), uniformly spaced along the vertical direction. The boundary conditions are the same as those presented in Tab. 4.1, except that the outlet pressure is 60 kPa.
Tab. 4.3 shows the global results of the optimization. The secondary flow increases by 12% from the single to the 2 nozzles design. The growth of secondary flow is even larger when splitting the primary stream into 4 nozzles, with 28% difference with respect to the original configuration. Moreover, the Mach number of the primary stream decreases while that of secondary flow increases. This is a clear indication of greater mixing.
The main reason for these improvements is to be found in the significant increase in contact surface between the two streams. Although the shear layer of the single nozzle is greater than those of other configurations, the splitting of the primary stream increase the number of mixing layers, i.e., the total shear surface inside the mixing chamber. Fig. 4.12 illustrates this concept by showing all together the shear regions for the 3 cases.

Variable	**Unit**	**Single nozzle**	**2 nozzles**	**4 nozzles**
m_1	*Kg/s*	*8.24*	*8.24*	*8.24*
m_2	*Kg/s*	*7.86*	*8.80*	*10.07*
ER	-	*0.95*	*1.07*	*1.22*
P – inlet	*kPa*	*56,7*	*53,2*	*44,7*
P – outlet	*kPa*	*60*	*60*	*60*
Ma_1 – outlet	-	*2.5*	*2.4*	*2.2*
Ma_2 – outlet	-	*0.47*	*0.53*	*0.64*

δ_ω – outlet	*m*	*1x0.013*	*2x0.013*	*4x0.012*

Tab. 4.3: Global results of the planar mixing chamber optimization

The calculation presented above is only one example among many other possible applications. Indeed, by means of a simple mixing model like that presented here, an optimization may be performed in order to find the best design in terms of sizes and number of primary nozzles, distance between the nozzles and from the external surface, length of the mixing chamber. In practice, the use of the Q1D approximation allows regarding the ejector as an equivalent "momentum exchanger" between two coflowing streams. Consequently, many of the design concepts that were developed for the optimization of heat exchangers (Bejan and Lorente, 2008) may be applied.

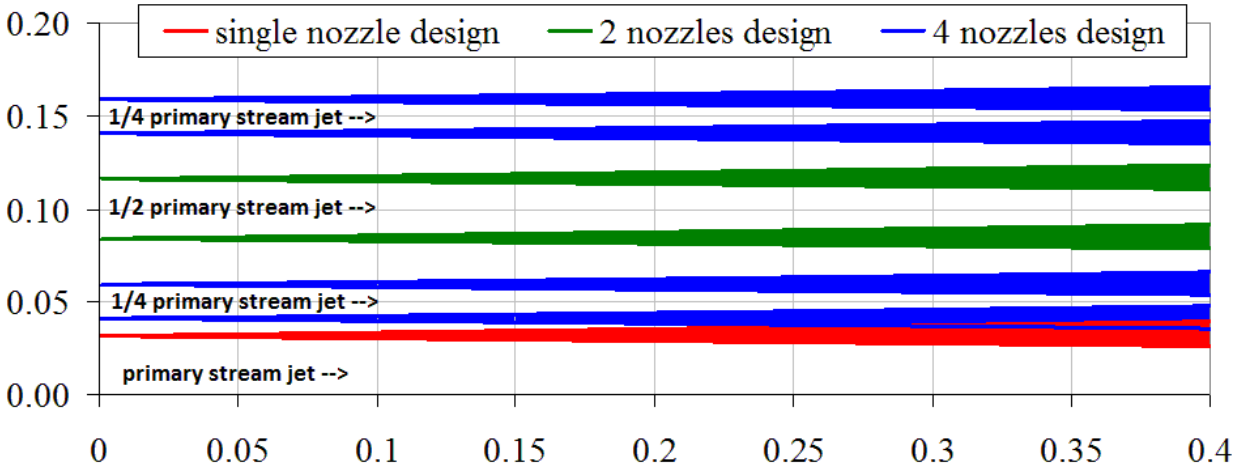

Fig. 4.12: Half section of the planar mixing chamber; colored regions represent the shear layers

References

Adams, T., Grant, C., Watson, H., 2012. A Simple Algorithm to Relate Measured Surface Roughness to Equivalent Sand-grain Roughness. Int. J. Mech. Eng. and Mechatron. 1, 66-71

Al-Ansary, A.M., Jeter, S.M., 2004. Numerical and Experimental Analysis of Single-Phase and Two-Phase Flow in Ejectors, HVAC&R Research, 10:4, 521-538

ANSYS Fluent User's Guide, release 15.0, 2013, ANSYS Inc., Canonsburg, PA

Barone, M.F., Oberkampf, W.L., Blottner, F.G., 2006. Validation case study: Prediction of compressible turbulent mixing layer growth rate, AIAA Journal, 44(7), 1488–1497

Bartosiewicz, Y. , Aidoun, Z., Mercadier, Y., 2006. Numerical assessment of ejector operation for refrigeration applications based on CFD. Applied Thermal Engineering, 26, 604–612

Bartosiewicz, Y., Aidoun, Z., Desevaux, P., Mercadier, Y., 2005. Numerical and experimental investigations on supersonic ejectors, International Journal of Heat and Fluid Flow 26, 56-70.

Bejan, A., Lorente, S., 2008. Design with Constructal Theory, John Wiley & Sons, Inc., Hoboken, New Jersey

Brown, B.P., Argrow, B.M., 1999. Calculation of supersonic minimum length nozzle for equilibrium flow, inverse problem in engineering, 7, 66-95

Brown, G. L., Roshko, A., 1974. On density effects and large structure in turbulent mixing layers, Journal of Fluid Mechanics, 64(4), 775–816

Cai, L., Zheng, H.T., Li, Y.J., Li, Z.M., 2011. Computational fluid dynamics simulation of the supersonic steam ejector. Part 2. Optimal design of geometry and the effect of operating conditions on the ejector, Proceedings of the Institution of Mechanical Engineers, Part C: Journal of Mechanical Engineering Science, 226, 715-723

Chandrasekhara, M.S., Krothapalli, A., Baganoff, D., 1991. Performance characteristics of an underexpanded multiple jet ejector, Journal of Propulsion and Power, 7(3), 462-464

Dutton, J.C., Carroll, B.F., 1986. Optimal supersonic ejector design, Transaction of the ASME, 108, 414-420

Eames, I.W., 2002. A new prescription for the design of supersonic jet-pumps: the constant rate of momentum change method. Applied Thermal Engineering, 22, 121–31

Eames, I.W., Aphornratana, S., Da-Wen Sun, 1995. The jet-pump cycle – a low cost refrigerator option powered by waste heat. Heat Recovery Systems & CHP, 15, 711-721

ESDU, 1986. Ejectors and jet pumps, Data item 86030, ESDU International Ltd, London, UK, 1986.

Gatsky, T.B., Bonnet, J.-P., 2013. Compressibility, Turbulence and High Speed Flow. 2nd edition, Academic Press, Oxford, UK

Grazzini G., Mazzelli, F., Milazzo, A., 2015. Constructal design of the mixing zone inside a supersonic ejector, Constructal Law & Second Law Conference 18-19 may, Parma, Italy

Grazzini, G., Milazzo, A., Paganini, D., 2012. Design of an ejector cycle refrigeration system, Energy Conversion and Management 54, 38–46

Grazzini, G., Rocchetti, A., 2008. Influence of the objective function on the optimisation of a steam ejector cycle, International Journal of Refrigeration, 31, 510 – 515

He, S., Li, Y., Wang, R.Z., 2009. Progress of mathematical modeling on ejectors, Renewable and Sustainable Energy Reviews 13, 1760–1780

Hemidi, A., Henry, F., Leclaire, S., Seynhaeve, J.-M., Bartosiewicz, Y., 2009a. CFD analysis of a supersonic air ejector. Part I: Experimental validation of single-phase and two-phase operation, Applied Thermal Engineering 29, 1523-1531.

Hemidi, A., Henry, F., Leclaire, S., Seynhaeve, J.-M., Bartosiewicz, Y., 2009b. CFD analysis of a supersonic air ejector. Part II: Relation between global operation and local flow features, Applied Thermal Engineering 29, 2990-2998.

Hickman, K.E., Hill, P.G., Gilbert, G.B., 1972. Analysis and testing of compressible flow ejectors with variable area mixing tubes, Journal of basic engineering, Trans. ASME, 407-416
Hodge, B.K., Koenig, K., 1995. Compressible Fluid Dynamics: With Personal Computer Applications, Prentice Hall College Div
Hoffman, J.D., Scofield, M.P., Thompson, H.D., 1972. Thrust nozzle optimization including boundary layer effects, Journal of optimization theory and applications, 10
Huang B.J., Chang J.M., Wang C.P., Petrenko V.A., 1999. A 1D analysis of ejector performance, International Journal of Refrigeration, 22, 354–64.
Ikawa, H., 1973. Turbulent mixing layer experiments in supersonic flow, Ph.D. Thesis, California Institute of Technology, Pasadena, CA
Johnson III, J.A., Wu, B.J.C., 1974. Pressure recovery and related properties in supersonic diffusers: a review, National Technical Information Service
Kim, S., Jin, J., Kwon, S., 2006. Experimental Investigation of an Annular Injection Supersonic Ejector, AIAA Journal, 44(8), 1905–1908
Matsuo, K., Miyazato, Y., Kim, H.D., 1999. Shock train and pseudo-shock phenomena in internal gas flows, Progress in Aerospace Sciences 35, 33-100
Mazzelli, F., Little, A.B., Garimella, S., Bartosiewicz, Y., 2015. Computational and Experimental Analysis of Supersonic Air Ejector: Turbulence Modeling and Assessment of 3D Effects, International Journal of Heat and Fluid Flow, 56, 305–316.
Mazzelli, F., Milazzo, A., 2015. Performance analysis of a supersonic ejector cycle working with R245fa, International Journal of Refrigeration, 49(0), 79-92
Munday, J. T., Bagster, D. F., 1977. A new ejector theory applied to steam jet refrigeration, Ind. Eng. Chem. Proc. Des. Dev. 164, 442-449
Papamoschou, D., 1993. Model for entropy production and pressure variation in confined turbulent mixing, AIAA journal, 31(9), 1643-1650
Papamoschou, D., 1996. Analysis of partially mixed supersonic ejector, Journal of propulsion and power, 12(4), 736-741
Papamoschou, D., Roshko, A., 1988. The compressible turbulent shear layer: An experimental study, Journal of Fluid Mechanics, 197, 453–477
Pope, A., Goin , K.L., 1978. “High-Speed Wind Tunnel Testing”, Wiley
Rajaratnam, N., 1976. Turbulent Jets, Elsevier scientific publishing company
Schlichting, H., 1979. Boundary-Layer Theory, 7th edition, McGraw-Hill
Shope, F.L., 2006. Contour Design Techniques for Super/Hypersonic Wind Tunnel Nozzles, 24th applied Aerodynamics Conference 5 - 8 June, San Francisco, California, AIAA 2006-3665
Smits, A.J., Dussauge, J., 2006. Turbulent Shear Layers in Supersonic Flow, Second Edition, Springer Science+Business Media Inc.
Srikrishnan, A.R., Kurian, J., Sriramulu, V., 1996. Experimental study on mixing enhancement by petal nozzle in supersonic flow, Journal of Propulsion and Power, 12(1), 165-169
Taylor, J.B., Carrano, A.L., Kandlikar, S.G., 2006. Characterization of the effect of surface roughness and texture on fluid flow—past, present, and future. International Journal of Thermal Sciences, 45, 962–968
Townsend, A.A., 1976. The Structure of Turbulent Shear Flow, 2nd edition, Cambridge University Press
Wilcox, D.C., 1992. Dilatation-dissipation corrections for advanced turbulence models, AIAA Journal, 30(11), 2639-2646
Wygnanski, I., Fiedler, H.E., 1970. The two-dimensional mixing region, Journal of Fluid Mechanics, 41, 327–362
Zagarola, M.V., Smits, A.J., 1998. Mean-flow scaling of turbulent pipe flow. J. Fluid Mech. 373, 33-79.
Zhu, Y., Cai, W., Wen, C., Li, Y., 2009. Numerical investigation of geometry parameters for design of high performance ejectors, Applied Thermal Engineering, 29 (5–6), 898–905

Zucker, R.D., Biblarz, O., 2002. Fundamentals of gas dynamics, 2nd edition, John Wiley & Sons, Inc., Hoboken, New Jersey
Zucrow, M. J., 1976. Gas Dynamics, John Wiley & Sons, Inc.

Part III – Two-Phase Supersonic Ejectors

Chapter's index:

Phase change phenomena inside supersonic ejectors can occur in different ways depending on the application. In standard Supersonic Ejector Cycles, condensation or freezing may occur due to the expansion of a "wet refrigerant" inside the two-phase dome (see chapter 2.1). Conversely, throttling loss recovery in Ejector Expansion Cycles requires the expansion of a saturated liquid or supercritical fluid that lead to evaporation of a substantial fraction of the primary flow (see chapter 1.3).

Although the physical mechanisms involved are similar, the theory behind these phase-change phenomena has historically evolved in distinct directions due to the different context of applications. In particular, for condensing high-speed flows, much of the work has been carried out in the context of steam turbine research. Low pressure steam turbines are affected by problems of droplets formation that lead to thermodynamic losses and blade erosion (Gyarmathy, 1962). Advances in this field have been mostly pioneered by the prominent work of Aurel Stodola at the beginning of the twentieth century (Stodola, 1927).

By contrast, the idea of using ejectors to recover expansion losses in standard and transcritical refrigerator has only recently drawn significant attention of the industrial and scientific community. Although the idea behind the Ejector Expansion Cycle is simple, the underlining physics is very complex (e.g., non-equilibrium flashing or cavitation, atomization of droplets and formation of liquid ligaments, interaction between turbulence, shocks and droplets, etc…). One of the main problems is the lack of reliable experimental results that impedes the development of accurate theoretical and numerical tools for the analysis of the ejector. Consequently, due to the absence of a consolidated knowledge, the subject will not be covered in this work.

In chapter 5 the theory of high-speed condensation is thoroughly detailed while chapter 6 investigates the problems connected to the CFD modeling of condensing supersonic nozzles and ejectors.

5. High-speed condensation

In general, condensation phenomena inside supersonic ejectors are significantly more complex than in standard devices such as condensers. The high levels of speed, compressibility and turbulence notably complicate the study that, in most cases, must rely on empiricism and experimental data.
In the ideal case of a reversible transformation, the condensation process follows a path of equilibrium states, and no losses occur. Inside supersonic ejectors however, the very limited residence time and high cooling rates lead to a substantial departure from the equilibrium process. As the primary flow rapidly expands inside the motive nozzle, thermodynamic equilibrium is not maintained and, at a certain degree of expansion, the vapor state collapses and condensation takes place abruptly as a shock-like disturbance. This is generally called the "**condensation shock**". This sudden change of state of aggregation leads to an instantaneous and localized heat release (heat of vaporization). The heat release alters the thermodynamic conditions along the motive nozzle by increasing pressure and temperature as well as reducing the Mach number. More than this, the condensation shock implies large gradients between the phases and, consequently, large irreversibilities.
Downstream the condensation shock, the flow contains a considerable number of tiny liquid droplets (of the order of $10^{19}/dm^3$) that affect the turbulence levels and the subsequent shear layer development in the mixing chamber (Crowe et al., 2012). Therefore, in addition to a reduction of the nozzle efficiency, condensation can also have consequences on the suction flow entrainment.
In studying the condensation inside a supersonic nozzle, it is important to distinguish between two different stages of the process: the droplet formation stage or **nucleation** and the **droplet growth**.
Although in high speed condensation these two processes occur almost simultaneously, the division is important because of the different tools that can be employed for the analysis: while the study of droplet growth can be handled by the familiar means of classical thermodynamics, the **prediction** of the nucleation process must consider the microscopic behavior of the fluid. At this scale, the usual continuum hypothesis does not hold, and the study must rely upon statistical mechanics or kinetic theory concepts. The statistical mechanics treatise will not be covered in this context, as the mathematical tools behind this theory are usually not within the reach of engineering curricula. A precise review of this approach is given by Ford (2004).
By contrast, the kinetic approach is at the base of the "classical nucleation theory", which still today represents the most common approach to predict droplet formation, at least for engineering purposes. However, before going into details of the kinetic of nucleation, it is necessary to revert to thermodynamics in order to understand the conditions under which a vapor departs from the gaseous state. This is the subject of the next chapter.

5.1 Phase Stability

Classical thermodynamics assumes that phase transition occurs immediately at the saturation line. In real systems however, phase change usually takes place under non-equilibrium conditions (Carey, 1992). Anytime the fluid crosses the saturation line without incurring in a phase transition, the system is said to be in a "metastable state". Under these conditions, the system is not thermodynamically stable, meaning that a perturbation can drive the system far from the initial conditions, i.e., to a different state of aggregation.
From a macroscopic point of view, these non-equilibrium conditions can be reached following an infinite numbers of different paths. Among these, two of the most common are the isothermal increase of pressure above the saturation line, i.e. the vapor **supersaturation**, and the isobaric cooling below the saturation temperature, viz., the vapor **supercooling**.

These two different paths allow the definitions of parameters that quantify the "degree of meta-stability" of the system, respectively called the "degree of supersaturation" and the "degree of supercooling":

$$\varphi_{ss} = \frac{p_v}{p_{sat}(T_v)} \qquad \varphi_{sc} = T_{sat}(p_v) - T_v \qquad \text{eq. 5-1}$$

where both parameters are >1 in metastable conditions and the subscript *v*, which stands for *vapor*, represents the local static state of the fluid.
It is important to note, that these two reference transformations do not describe the isentropic expansion of a vapor inside a supersonic nozzle, as shown in Fig. 5.1. In practice however, it doesn't matter how the system reached the metastable condition (as this represents a well defined thermodynamic state) and both parameters can be equally used to locate the metastable state in the phase space[15].

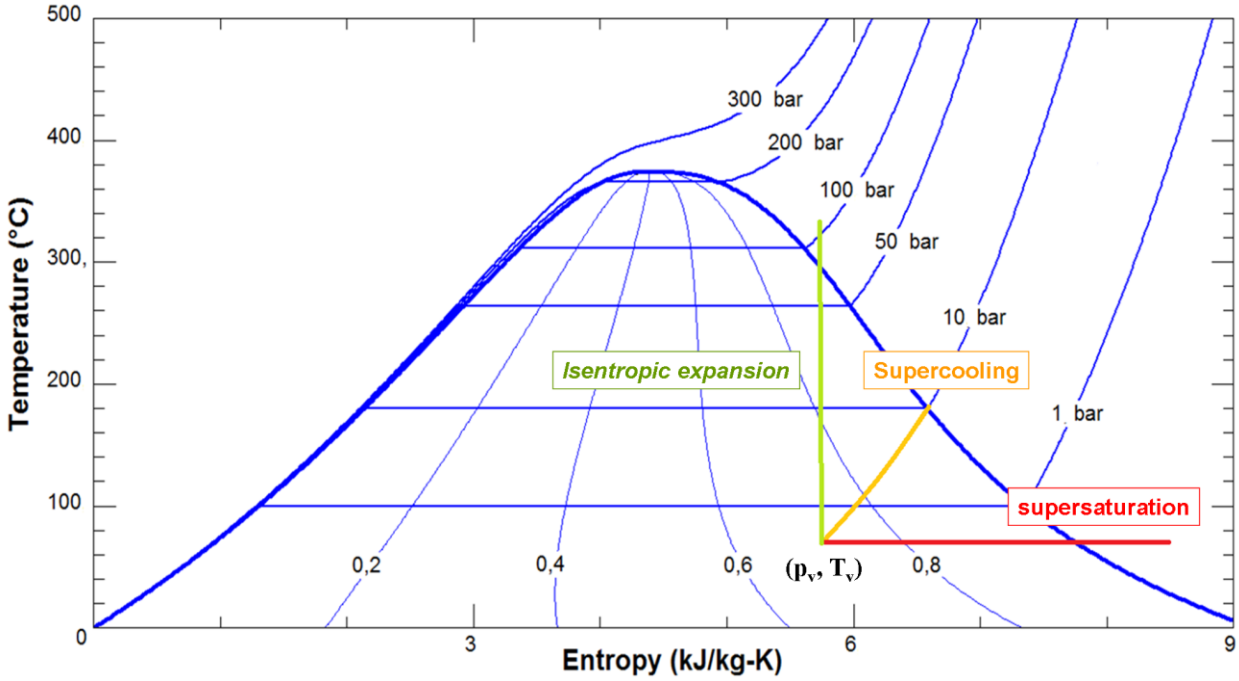

Fig. 5.1 – T-s diagram for steam, showing the various processes that can lead to a metastable state

From a microscopic point of view, the metastable condition is characterized by the continuous formation of liquid nuclei due to the random movement of the vapor molecules. The molecular fluctuations that create the liquid nuclei constitute a probabilistic phenomenon that must be studied by statistical concepts. The knowledge of the rate and magnitude of these density fluctuations is crucial for the prediction of the conditions under which condensation starts. We will return to this aspect in the next chapter.
Once a liquid nucleus is formed, this can either collapse, grow or stay in equilibrium with the surrounding vapor. In order to understand which one of these routes the nucleus will take it is necessary to study its stability, i.e., we must ask if equilibrium is possible and whether this is stable or not.
Generally speaking, the stability of any liquid or vapor in metastable conditions can be analyzed by at least two different thermodynamic approaches. The first of these methods ignores the microscopic behavior of the fluid (i.e., the continuous formation of nuclei) and studies the thermal and mechanical

[15] In the same way, one could define two "super-expansion" parameters: $\varphi_{se\_p} = \frac{p_v}{p_{sat}(s_v)}$ and $\varphi_{se\_T} = T_{sat}(s_v) - T_v$

stability of a pure, single-phase fluid. The analysis shows that there is a well defined limit beyond which no metastability is possible and the system must undergo phase transition. This is called the "spinodal limit". Details of this approach can be found in Grazzini *et al.* (2011) or Carey (1992).
The second approach focuses on a two-phase system composed of a droplet surrounded by an infinite mass of pure vapor. The conditions for the growth or collapse of the droplet are investigated by a thermodynamic approach that involves the study of the Gibbs free-energy of the system. This second approach is crucial for the prediction of the nucleation process and will be illustrated next.
In the analysis, we refer to the droplet as the "system", while the infinite mass of surrounding vapor will be referred to as the "environment" or simply the "surrounding". The surrounding is assumed to be at a well defined state with constant pressure, p_v, and temperature, T_v (this may represents a "frozen" state condition of the isentropic expansion inside the nozzle). Under these constraints, the establishment of thermodynamic (stable) equilibrium requires the "system" to reach a minimum of the total Gibbs free energy, G. This is briefly demonstrated in Appendix B.
The above statement is the equivalent of the maximum entropy statement for an isolated system. Depending on the system constraints and surrounding conditions, the spontaneity of a process and its equilibrium state are described by different thermodynamic functions[16] like entropy or the Helmholtz free energy, F. Some of these conditions are visually summarized in Tab. 5.1, a highly recommended discussion about these concepts can be found in Ford (2013).

System constraints	**Surrounding conditions**	**Spontaneous Process**	**Equilibrium state**
Isolated system no mass, work or heat exchange	/	$dS \geq 0$	Maximum S
Closed system no mass or work exchange	Constant T	$dF \leq 0$	Minimum F
Closed system no mass exchange	Constant P and T	$dG \leq 0$	Minimum G

Tab. 5.1 – Conditions for the occurrence of a spontaneous process and equilibrium state for different kinds of systems and surroundings

The stability of the droplet under fixed pressure and temperature can thus be analyzed by computing the variation of the system Gibbs energy from the initial condition of pure vapor to the state where the droplet has formed.
Following Bakhtar *et al.* (2005), the process of droplet formation can be conveniently subdivided into three main stages: a first isothermal expansion of the vapor down to the pressure of saturation, the formation of the liquid interface, the recompression of the liquid to the local value of pressure. It is important to note that this is by no means the sequence that is really followed by the system; however, being G a state function, it is irrelevant what path is selected, as long as the initial and final states coincide.
The total Gibbs free energy variation is thus given by:

$$\Delta G_{vapour \rightarrow droplet} = \Delta G_{vapour\_expansion} + \Delta G_{droplet\_formation} + \Delta G_{liquid\_compression} \qquad \text{eq. 5-2}$$

Where G is the free energy of the total mass involved in the condensation, m_l.
By assuming ideal gas behavior of the vapor phase, the first term is calculated as follows:

[16] In analogy with Mechanics, these are called thermodynamic potentials in view of their use in describing the direction of spontaneous process and the conditions for equilibrium of the system

$$\Delta G_{vapour\_expansion} = m_l RT_v \int_{p_v}^{p_{sat}(T_v)} \frac{1}{p} dp = -\frac{4}{3}\pi r^3 \rho_l RT_v \ln \varphi_{ss} \qquad \text{eq. 5-3}$$

The second term depends on the sole surface tension is given by[17]:

$$\Delta G_{droplet\_formation} = 4\pi r^2 \sigma(T_v) \qquad \text{eq. 5-4}$$

Finally, the last term can be computed as follows:

$$\Delta G_{liquid\_compression} = \frac{m_l}{\rho_l} \cdot \int_{p_{sat}(T_v)}^{p_v} dp = \frac{4}{3}\pi r^3 \left(p_v - p_{sat}(T_v)\right) \qquad \text{eq. 5-5}$$

where it was assumed a constant density for the liquid phase. This last term is usually small and can be neglected without incurring in significant approximations (Bakhtar *et al.*, 2005).
Summing up the various contributions, the total free energy variation is given by:

$$\Delta G_{vapour \to droplet} = 4\pi r^2 \sigma(T_v) - \frac{4}{3}\pi r^3 \rho_l RT_v \ln \varphi_{ss} \qquad \text{eq. 5-6}$$

The above expression, is one of the fundamental equations that constitute the classical nucleation theory.
In order to understand whether equilibrium can exist, we must compute the derivative of eq. 5-6 as a function of the radius[18], and impose it equal to zero:

$$\frac{dG}{dr} = 4\pi r\sigma - 4\pi r^2 \rho_l RT_v \ln \varphi_{ss} = 0 \qquad \text{eq. 5-7}$$

Solving for the radius gives:

$$r_c = \frac{2\sigma}{\rho_l RT_v \ln \varphi_{ss}} \qquad \text{eq. 5-8}$$

The above expression describes the radius for which the droplet is in equilibrium with the surrounding vapor. This is usually called the **critical radius**. The most important aspect that must be noticed in eq. 5-8 is that the critical radius becomes smaller as the degree of supersaturation increases. We will come back to this aspect later in this chapter.
Solving eq. 5-8 for the denominator and inserting the resulting expression in eq. 5-6 returns a very compact equation for the Gibbs free energy required to form a droplet having precisely the critical radius:

$$\Delta G_c = \frac{4}{3}\pi r_c^2 \sigma = \frac{1}{3} S_c \sigma \qquad \text{eq. 5-9}$$

where S_c is the surface area of the equilibrium droplet.

[17] this is by definition the energy required to form an interface of unit area (Carey, 1992)
[18] We are analyzing a fixed state of the droplet-vapor system having pressure and temperature equal to T_v and p_v. Hence, the free energy variation depends solely on the droplet radius.

The final step of the analysis consists in determining whether this equilibrium is stable or not. In order to discover this, the Gibbs free energy expression, eq. 5-6, can be plotted to study its behavior as the radius vary. This is shown in Fig. 5.2.

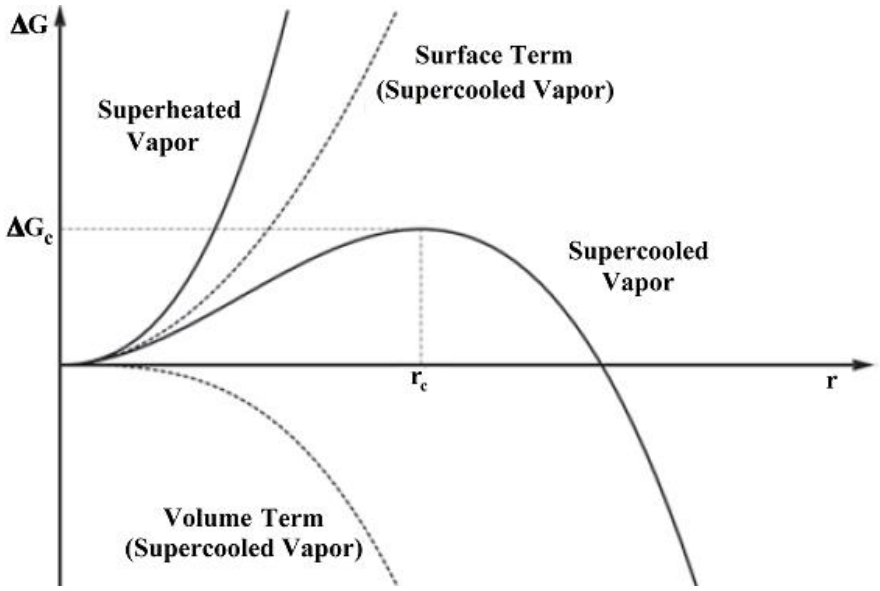

Fig. 5.2 – Gibbs free energy variation for the process of droplet formation in the case of superheated and supercooled vapor state, from Bakhtar *et al.* (2005)

As a first remark, eq. 5-6 is composed by a surface and a volume terms: while the first term is always positive, the sign of the second term depends on the supersaturation ratio. In the case of superheated vapor (i.e., $0 < \varphi_{ss} < 1$), the volume term is positive and ΔG becomes a monotonically increasing function of the radius. This means that whenever a nucleus is formed inside a superheated vapor, this will spontaneously tend to collapse (the minimum of the Gibbs free energy is for a radius equal to zero).

By contrast, when the vapor is in metastable conditions, the two terms have opposite signs. Due to the different exponents, the surface term dominates for small radius, while the opposite is true for larger radius. Consequently, the Gibbs free energy increases up to a maximum occurring at the critical radius and then decreases down to negative values. The presence of this maximum indicates that the equilibrium is **unstable**: nuclei smaller than the critical size must collapse while those with radii greater than the critical have the tendency to grow.

However, the formation of any of these nuclei is against the natural tendency of the system. This is because ΔG can be considered like an energy barrier. From a microscopic point of view, this can be understood by considering that the formation of a droplet requires the enclosure of a large number of molecules into a very small and confined region (i.e. the liquid embryo). Due to the repulsive forces between molecules a potential barrier form and the establishment of the nucleus requires some work to be done on the system. This work must be provided by the kinetic energy of the same molecules constituting the surrounding vapor.

From a macroscopic point of view, the potential barrier can be correctly interpreted by investigating further the significance of the Gibbs free energy.

By assuming constant pressure and temperature of the surrounding vapor, the droplet formation can be approximately regarded as an isothermal and isobaric process. Under these constraints, the Gibbs free energy variation between the initial (pure vapor) and final state (liquid droplet) of the system becomes equivalent to its exergy variation[19]:

[19] Rigorously, this is the availability of the system, see Ford (2013)

$$\Delta G = \Delta U + p_v \Delta V - T_v \Delta S = \Delta Ex \qquad \text{eq. 5-10}$$

where it is assumed that the reference state for exergy is at T_v and p_v [20].
Therefore, in the ideal case of a reversible process, the Gibbs free energy variation corresponds to the *maximum reversible work* that can be extracted from the system. In the opposite perspective, we can equally say that eq. 5-10 represents the *minimum reversible work* required to create the droplet (the aforementioned energy barrier):

$$\Delta G_{rev} = \Delta U + p_v \Delta V = W_{\min} \qquad \text{eq. 5-11}$$

Inserting eq. 5-8 into eq. 5-9 returns the minimum work required to form a critical cluster as a function of the flow parameters:

$$\Delta G_c = \frac{16}{3} \frac{\pi \sigma^3}{\left(\rho_l R T_v \ln \varphi_{ss}\right)^2} = W_c \qquad \text{eq. 5-12}$$

In eq. 5-12 it is interesting to note the strong influence of the surface tension. This, in turn, depends on the system temperature and is equal to zero at the fluid critical point. Therefore, lower values of supersaturation should be expected for flow conditions that are close to the critical point. Moreover, as the supersaturation increases, the W_{eq_min} decreases but the barrier never disappears completely (Bakhtar *et al.*, 2005). In other words, a metastable state becomes increasingly less stable as the degree of supersaturation (or supercooling) grows.
Although these information are essential to model the phase transition, the correct prediction of the nucleation stage requires also the knowledge of how many "critical sized" nuclei form in the vapor stream. This is a probabilistic calculation that can be handled by means of statistical mechanics (see Ford, 2004) or kinetic theory concepts. This last approach is illustrated in the next chapter.

5.2 Nucleation

In the preceding chapter it was shown that the condensation of a supersaturated vapor requires the formation of droplets with radius greater than r_c.
There are two main mechanisms through which critical clusters can form. The first is due to the presence of foreign particles within the vapor or surface vacancies at the solid walls containing the flow. Qualitatively speaking, these impurities and surface imperfections constitute the primordial sites where the molecules aggregate to form an embryo. This process is called **heterogeneous nucleation** and is typical of phase transitions inside conventional condenser (Carey, 1992). The second mechanism is called **homogeneous nucleation** and originates from random density fluctuations due to thermal agitation of the vapor molecules[21]. Although it can be observed in any system, this type of nucleation is the primary mechanism through which droplets form inside high-speed nozzles (Wegener and Mack, 1956).
The homogeneous nucleation is thus a stochastic phenomenon that must be addressed by means of statistical and probabilistic evaluations. As it might be guessed, the probability that a cluster forms

[20] In practice, the reference environment for the exergy definition is the surrounding vapor itself. This unusual reference state makes sense if one considers that the energy to create the droplet is provided by the vapor itself. Nevertheless, the definition of the reference state becomes superfluous if one considers the system availability instead of its exergy.
[21] The reason for these two names comes from the fact that in the first case nucleation occur at will defined spots whose location is not uniformly distributed while the second occur homogeneously all over the volume of fluid.

depends on the ratio between the potential barrier and the average kinetic energy of the vapor molecules. This ratio defines a dimensionless parameter called the Gibbs number:

$$Gb = \frac{\Delta G}{kT_v} \qquad \text{eq. 5-13}$$

where k is the Boltzmann constant, ΔG is given by eq. 5-6 and is a function of the embryo size.
In the classic approach of homogeneous nucleation theory, the nucleation of clusters is described through the so-called **nucleation rate**, J, defined as the number of nucleation events occurring in a unit volume per unit time (Brennen, 2013). Many formulations exist for J, but almost all of them assume the general form:

$$J = J_0 e^{-Gb} \qquad \text{eq. 5-14}$$

where J_0 is some factor of proportionality that will be described next.
The presence of the exponential in eq. 5-14 is indicative of the shock-like nature of the homogeneous condensation phenomenon. We will come back to this aspect later on.
Over the years, a great number of different expressions and corrections have been devised for both J_0 and the argument of the exponential. Many of these are carefully reviewed by Bakhtar *et al.* (2005) and will not be detailed here. Herein, the focus will be only on the classical formulation and its demonstration, which is useful in understanding the main assumptions and concepts that lie behind theory. In deriving the explicit expression for J, we will follow a procedure similar to that outlined by Bakhtar *et al.* (2005), but an analogous derivation can be found in Carey (1992).
Before to begin, it is important to stress the fact that the analysis will not deal with the probability of formation of individual clusters, but rather on the time evolution of their **size distribution**:

$$\frac{dn_2}{dt}, \frac{dn_3}{dt}, \frac{dn_4}{dt}, \ldots\ldots \frac{dn_x}{dt} \qquad \text{eq. 5-15}$$

where n_x represents the number of clusters composed of "x-molecules" that are found every instant in a unit volume of gas.
The analysis considers a metastable vapor in supersaturation conditions ($\varphi_{ss}>1$). Due to the thermal agitation of the molecules, clusters are continuously formed and disrupted within the volume of fluid (Bakhtar *et al.* 2005). Therefore, the identities and position of the individual clusters change instantaneously within the vapor volume. Despite this, due to the large numbers involved, the average population of each cluster group is more stable in time.
In order to find a simple mathematical expression for the evolution of the size distribution it is assumed that the passage of a cluster from one size to another occurs only by the acquisition or loss of single molecules. From a simple molecules balance, it follows that the population of the "x-sized" cluster group, n_x, depends solely on the rate of condensation and evaporation from the groups of smaller and larger sizes:

$$\frac{dn_x}{dt} = \left(\dot{C}_{x-1} n_{x-1} - \dot{E}_x n_x\right) - \left(\dot{C}_x n_x - \dot{E}_{x+1} n_{x+1}\right) = \dot{I}_{(x-1)\leftrightarrow x} - \dot{I}_{x\leftrightarrow(x+1)} \qquad \text{eq. 5-16}$$

where $\dot{E}$ and $\dot{C}$ represent here the average evaporation and condensation rates of an entire cluster group, measured in [n. molecules/s] .

The variable $\dot{I}$ represents the so-called **nucleation current**, i.e. the number of clusters that move from one size group to another in the unit of time and volume. Its definition is essential for an easy closure of the homogeneous nucleation model, as explained below.
In general, liquid embryos can form in several different ways. For instance an embryo composed of x molecules may form by the aggregation of two smaller clusters, by the disruption of a larger cluster or even by the collision of x single molecules. Hence, the correct evaluation of the nucleation rate, J, would require the calculation of the probability connected to each of this possible way of cluster formation. The assumption of the existence of a simple nucleation current greatly simplifies the calculation. In practice, this assumption implies that the **nucleation rate** is equal to the **nucleation current**: $J=I$. Fig. 5.3 represents schematically the concept of the nucleation current assumption.

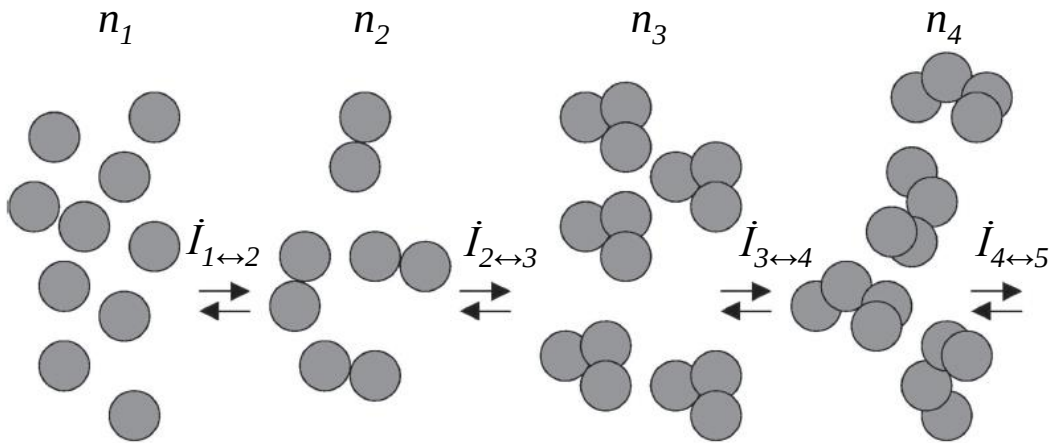

Fig. 5.3 – Scheme of the nucleation current, adapted from Ford (2004)

The goal of the analysis is now simplified to the simple evaluation of the nucleation current of the "critical-sized" clusters:

$$J_c = \dot{I}_{c\leftrightarrow(c+1)} \qquad \text{eq. 5-17}$$

In order to simplify the calculations for J_c, it is further assumed that the size distribution inside the vapor volume is steady:

$$\frac{dn_x}{dt} = 0 \qquad \text{eq. 5-18}$$

This assumption is reasonable because it is known that n_x reaches a steady distribution in few μs, whereas the active nucleation period in a nozzle flow lasts typically 10 to 50 μs (Bakhtar *et al.*, 2005). Based on this, the transient stage is usually ignored and it is assumed that the steady distribution is attained instantaneously. Inserting eq. 5-18 into eq. 5-16 leads to:

$$\dot{I}_{(x-1)\leftrightarrow x} = \dot{I}_{x\leftrightarrow(x+1)} = \dot{I} \qquad \text{eq. 5-19}$$

This means that that the nucleation current is equal for each size group and, in particular, we need to focus on the nucleation current of the critical-sized group of clusters. Now, this is simply given by:

$$J_c = \dot{I} = \dot{C}_x n_x - \dot{E}_{x+1} n_{x+1} \qquad \text{eq. 5-20}$$

In order to find J_c, we must find expressions for the average evaporation and condensation rates in eq. 5-20. The kinetic theory of gases serves this purpose. In practice, $\dot{E}$ and $\dot{C}$ can be obtained by calculating the rate at which vapor and liquid molecules impact the cluster surface from both sides. By assuming ideal gas behavior and spherical droplets, the evaporation and condensation rates are given by:

$$\dot{C}_x = q_C \frac{S_x}{m} \frac{p_v}{\sqrt{2\pi R T_v}}$$
$$\dot{E}_x = q_E \frac{S_x}{m} \frac{p_l}{\sqrt{2\pi R T_l}} \qquad \text{eq. 5-21}$$

where S_x is the cluster surface, m is the mass of one molecule[22] and q_C, q_E are the so-called **accommodation coefficients**.
These are defined as the ratio between the number of molecules that actually cross the interface and the total number of those impacting the surface. In practice, these coefficients quantify the fraction of impacts that, from both sides, concretely results in a condensation or evaporation of molecules.
Unfortunately, the simple substitution of eq. 5-21 into eq. 5-20 does not lead to an as much simple solution. In the original derivation, a different approach is used that requires considering the hypothetical situation of an equilibrium cluster distribution given by:

$$n'_x = n_v e^{-Gb_x} = n_v \exp\left(-\frac{\Delta G_x}{kT_v}\right) \qquad \text{eq. 5-22}$$

where n'_x is the equilibrium population of the "critical-sized" cluster group.
This distribution (which is known as Boltzmann distribution) actually represents the condition of a superheated gas ($\varphi_{ss}<1$). Due to the monotonically increasing trend of Gibbs free energy (see Fig. 5.2), droplet growth in a superheated gas is prohibited but cluster formation is nevertheless active. In this condition, the cluster distribution reaches a steady distribution where, for each size group, the number of created clusters is equal to those destroyed. Hence, under these hypotheses, the nucleation current is zero:

$$\dot{I} = 0 \quad \Rightarrow \quad \dot{C}_x n'_x = \dot{E}_{x+1} n'_{x+1} \qquad \text{eq. 5-23}$$

Inserting eq. 5-23 into eq. 5-20 to eliminate $\dot{E}_{c+1}$, results in:

$$J_c = \dot{C}_x n'_x \left(\frac{n_x}{n'_x} - \frac{n_{x+1}}{n'_{x+1}}\right) \qquad \text{eq. 5-24}$$

This expression can be rearranged in differential form to give:

[22] The molecular mass or weight, m [kg/molecule] is not to be confused with the molar mass, M [kg/kmol]. The mass of one molecule is found by dividing the molar mass by the Avogadro number: $m=M/N_A$.
In Carey (1992) M is mistakenly reported as the molecular weight.

$$J_c = \dot{C}_x n_x \frac{\partial(n/n')}{\partial x}$$ **eq. 5-25**

Inserting eq. 5-22 and eq. 5-21 into eq. 5-25 and integrating the resulting expression over the whole range of *x*-groups finally returns the classical formulation for the critical nucleation rate (details of the integration passages can be found in appendix 3 of Bakhtar *et al.*, 2005):

$$J_c = q_C \frac{\rho_v^2}{\rho_l}\left(\frac{2\sigma}{\pi m^3}\right)^{1/2} \exp(-Gb_c)$$ **eq. 5-26**

where J_c is measured in [n. molecules/m^{3}s].
To develop further eq. 5-26, Gb_c can be equally expressed as a function of the critical radius or the thermodynamic state of the system by respectively making use of eq. 5-9 and eq. 5-12:

$$Gb_c = \frac{\Delta G_c}{kT_v} = \frac{4\pi r_c^2 \sigma(T_v)}{kT_v} = \frac{16}{3}\frac{\pi\sigma(T_v)^3}{kT_v^3(\rho_l R \ln\varphi_{ss}(T_v))^2}$$ **eq. 5-27**

In particular, the last expression is of practical use for thermodynamic calculations.
Although eq. 5-27 was developed by considering an isothermal compression of the vapor, its use is not limited to this process because all the quantities in the expression are state variables. For instance, Fig. 5.4 shows a comparison of nucleation trends for different types of processes. These were selected so to have the final state in common (T_v*=300 K*, p_v*=35000 Pa*), as qualitatively represented in Fig. 5.1.
By considering the simple case of the supersaturation process (i.e., isothermal compression) all the parameters in eq. 5-27 remain constant except for the supersaturation ratio, which steadily increases. Therefore, eq. 5-26 can be written as follows:

$$J_c = J_0 \exp\left(-\frac{\alpha}{(\ln\varphi_{ss})^2}\right)$$ **eq. 5-28**

where both J_0 and α are constants that depend on T_v.
The growth of φ_{ss} brings about the rapid increase of the exponential term in eq. 5-26 and, at a certain time, the condensation takes place abruptly. By looking at Fig. 5.4, it is clear that a similar trend occurs also for the supercooling and isentropic expansion processes, though in these cases the simultaneous variation of all the parameters in eq. 5-27 and eq. 5-26 do not allow for a simple demonstration.
In passing, it is interesting to note that the isentropic expansion have the steepest trend among the three types of process. Indeed, we will see in later chapters that during the rapid expansion inside De Laval nozzles condensation takes the semblance of a dynamic shock.
Finally, despite the nucleation rate equation can be used for any of the illustrated transformations in Fig. 5.1, the rapidity of the process may influence in many subtle ways its accuracy and validity. This issue is analyzed in the next chapter.

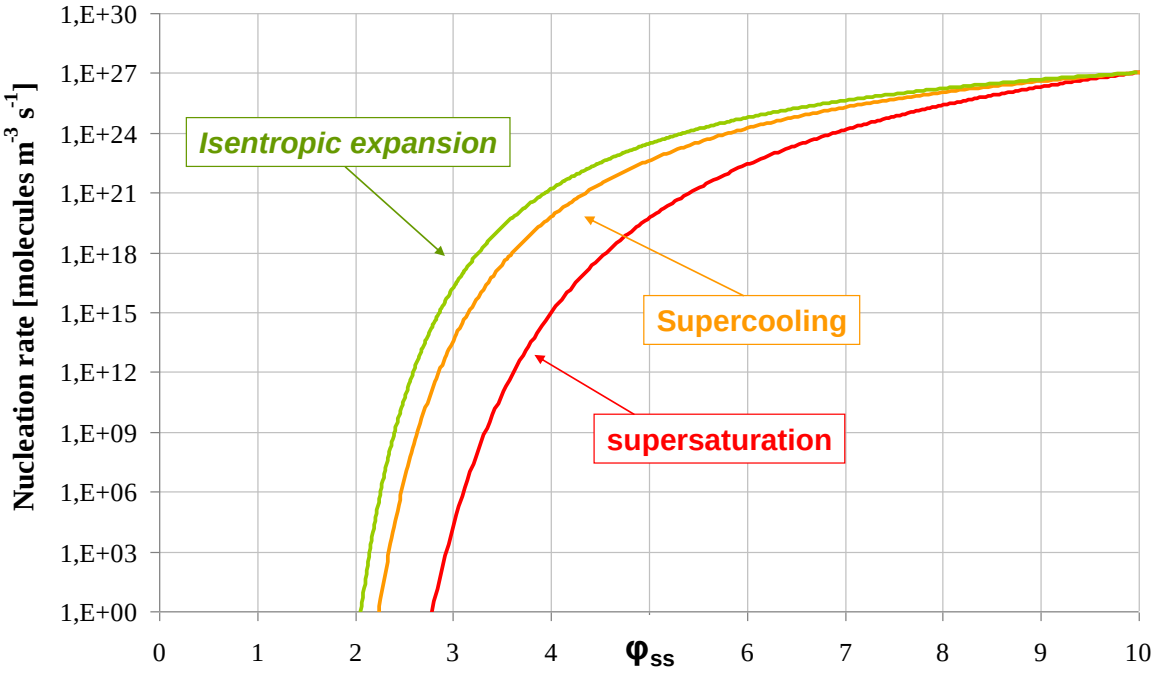

Fig. 5.4 – Comparison of nucleation rates for different processes, as a function of the supersaturation ratio

5.3 Onset of nucleation

The classical nucleation theory is remarkable in the way it provides for a very simple analytic expression for the nucleation rate. However, many assumptions were needed in order to achieve a simple closed solution, which may compromise the accuracy as well as the physical correspondence with the real phenomenon. Therefore, before passing on to the next stage of the condensation process, namely the droplet growth, it is worth to spend some time on this important expression to discuss some of its implications and related assumptions.

First of all, it should be noted that the hypothesis of the existence of a fictitious nucleation current is partly in contrast with the physical interpretation of the process. While a kinetic view envisages the formation of critical clusters as the outcome of random molecular fluctuations (which may or may not occur), the nucleation current model implies, for any condition of supersaturation, the existence of a critical cluster nucleation rate, no matter how small. In order to assess the validity of the nucleation current hypothesis, the results from the theory must be checked against experimental data on the onset of the nucleation process.

For clarity, let's first assume that the nucleation process begins as soon as the first critical cluster is formed. By a simple rearrangement, the nucleation rate equation, eq. 5-26, can provide for an estimate of the time required for the formation of this first critical embryo; we may call this quantity the **nucleation time**, Δt_n.

By considering $1m^3$ of vapor, Δt_n is simply given by the inverse of the nucleation rate:

$$J_c = \frac{n.\ critical\ \ clusters}{\Delta t \cdot Volume} \qquad \Rightarrow \qquad \Delta t\big|_{1cluster,1m^3} = \Delta t_n = \frac{1}{J_c} \qquad \text{eq. 5-29}$$

In the homogeneous nucleation literature however, it is customary to consider a volume of fluid of $1cm^3$ which implicates that eq. 5-29 be scaled by a factor of 10^6. The trends of Δt_n for this case are illustrated in Fig. 5.5.

As can be clearly seen from the figure, the time required for the nucleation of the first cluster changes dramatically with the degree of supersaturation. In particular, it is observed that for low values of φ_{ss} the nucleation time increases exponentially and the substance can stay almost indefinitely in the metastable state (Carey, 1992). In theory however, if we wait long enough, there will always be a perturbation such that a cluster with radius greater than r_c forms and lead the system to the phase transition. This situation is that contemplated by equilibrium thermodynamics, which postulates infinitely slow transformations and where no metastable state can exist.

The blue line highlighted in Fig. 5.5 represents a nucleation time of *1s* and its intersection with the three curves result in J_c=*1cluster* cm^{-3} s^{-1}. The supersaturation ratio that produces this particular value of J_c is customary termed the **critical supersaturation**, φ_{ss_c} [23] (Hill, 1966).

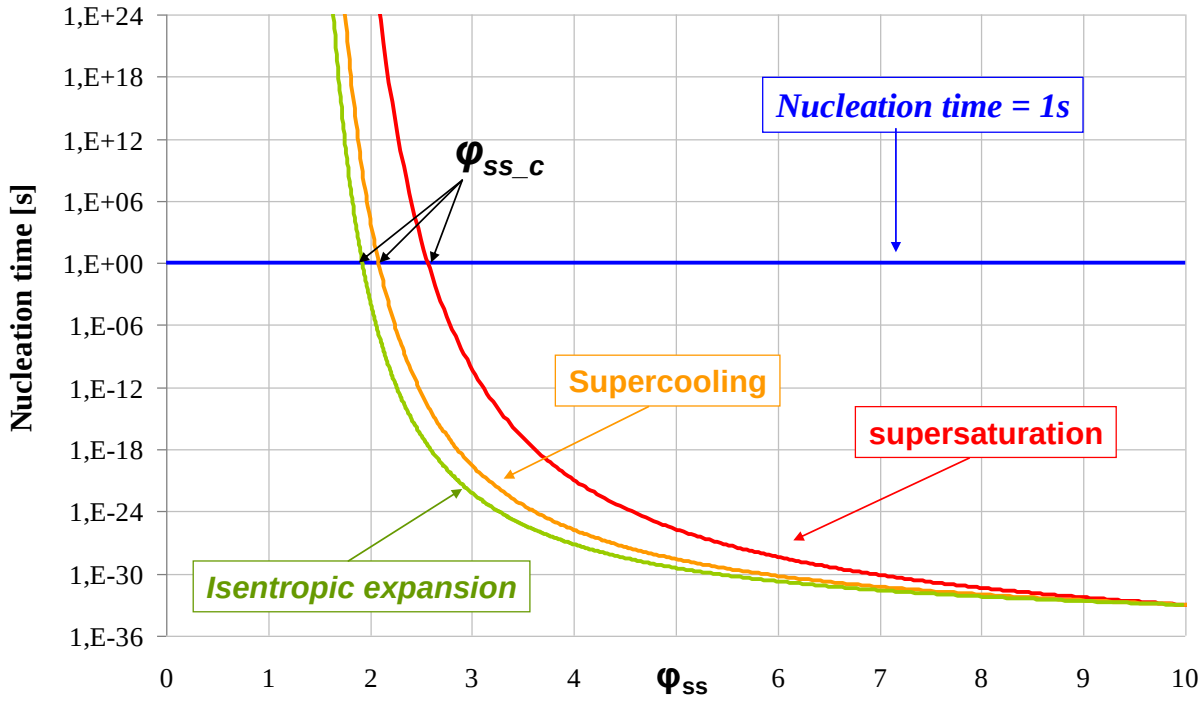

Fig. 5.5 – Comparison of nucleation times (viz. the time to form *1* critical cluster in *1* cm^3 of vapor) for different types of processes, as a function of the supersaturation ratio

Comparisons of theoretical results with many experiments in expansion chambers seem to support the choice of this arbitrary value as the indicator of the onset of nucleation. Indeed, the results obtained by various authors for different types of organic fluids indicate that the nucleation starts at a supersaturation ratio very close to φ_{ss_c} (see Carey, 1992, chapter 5.6). Unfortunately, this does not hold true for experimental data in supersonic nozzles, which show considerable scatter when compared with theoretical values for the critical supersaturation. The fact that diffusion chamber experiments agree better with theoretical results may not be a simple coincidence. In fact, this may depend on the longer characteristic time scales of the experiments, as explained below.

During the derivation of J_c, a steady nucleation current was assumed based on the evidence that the transient stage is short compared to the time needed by the vapor to flow through the nucleation zone. However, the time scale associated with the rapid expansion inside a supersonic nozzle may be well comparable with the time required to establish the steady size distribution postulated for the derivation of

[23] Admittedly, there are far too many "critical" quantities all along the nucleation theory (e.g., the fluid critical point, the critical cluster size, the critical supersaturation, etc…). However, the reader should try not to confuse them.

J_c, thus invalidating the assumption made in the model (Carey, 1992). Hence, it is not surprising that experimental data for such devices scatter significantly from predicted theoretical results.
The rapidity of the process may influence the validity of the nucleation rate in one further respect. Although it was not mentioned, the classical nucleation rate assumes that thermal equilibrium exists between the vapor and the growing cluster (the liquid density and surface tension in eq. 5-26 and eq. 5-27 were always calculated assuming a liquid temperature equal to T_v). However, the attainment of thermal equilibrium requires either slow transformations or a very effective transport of heat from the cluster to the surrounding vapor. In the absence of any of these conditions, the temperature in the cluster increases to value greater than T_v due to the release of the latent heat of condensation. This localized heat release makes the molecules of the liquid cluster more energized, thus enhancing the rate at which they evaporate from the cluster surface. Therefore, the net rate of condensation on each cluster is reduced and, consequently, the critical nucleation rate J_c is partially suppressed.
In order to account for this effect Kantrovitz (1951) calculated a correction factor for the critical nucleation rate:

$$J_{c\_NISO} = \frac{J_c}{1+\xi} \qquad \textbf{eq. 5-30}$$

where J_c is the classical nucleation rate from eq. 5-26, and ξ is given by:

$$\xi = q_C \frac{2(\gamma-1)}{(\gamma+1)} \frac{h_{lv}}{RT_v} \left(\frac{h_{lv}}{RT_v} - \frac{1}{2} \right) \qquad \textbf{eq. 5-31}$$

where γ is the specific heat ratio, h_{lv} is the latent heat of condensation and it was assumed that nucleation occurs under conditions that are not too close to the critical point. Typically, Kantrowitz' correction reduces the critical nucleation rate for water by a factor of 50–100 (Bakhtar *et al.*, 2005).
In addition to a reduction of the nucleation rate, the uncertainty connected to the liquid phase temperature directly impacts the value of the surface tension which, in turn, can significantly affect the critical nucleation rate (σ is present in eq. 5-26 both in the pre-exponential factor than in the exponential argument, where it is elevated at the third power!).
The surface tension is generally a linearly decreasing function of temperature. For instance, a semi-empirical expression from Eötvös and Ramsay-Shields gives the "flat-film surface tension" as a function of the fluid critical temperature (Wegener and Mack, 1958):

$$\sigma_\infty = c\upsilon_l (T_c - T_v) \qquad \textbf{eq. 5-32}$$

where υ_l is the liquid cinematic viscosity and c is a constant which for many liquids is equal to *2,12*.
Unfortunately, the uncertainty on the liquid temperature is not the only source of potential error for σ. Apart from the effect of surface impurities[24], the surface tension is generally believed to depend on the curvature of the cluster surface. At the very high supersaturation ratios achieved in condensing nozzle flows, a critical droplet is composed of 10–50 molecules (Bakhtar *et al.*,2005). At these very small curvature radii the value of surface tension may depart consistently from the conventional flat-film value.

[24] Although these dramatically change the value of surface tension, they should not be present inside a freshly formed droplet by vapor condensation. By contrast, this is a big issue in droplet nucleation and cavitation phenomena (see Carey, 1992; Brennen, 2013)

For instance, Tolman arrived by thermodynamic methods at a first approximation for the surface tension of a drop of radius *r* (Wegener and Mack, 1958):

$$\sigma(r) = \sigma_\infty \frac{r}{r + 2\delta} \qquad \text{eq. 5-33}$$

where δ is a constant of the order of the free molecular path.
Although the surface tension is generally believed to diminish with the radius of curvature (like in eq. 5-33), many other theories have been developed which are in marked contrast between each others, even on the sign of the variation (Bakhtar *et al.*, 2005). Consequently, despite the large uncertainty that this may introduce, the surface tension is in many cases calculated by considering the conventional flat-film value.
In conclusion of this chapter, it may be worth to spend some words on the expression for pre-exponential factor in the critical nucleation rate equation, namely:

$$J_0 = q_C \frac{\rho_v^2}{\rho_l} \left(\frac{2\sigma}{\pi m^3} \right)^{1/2} \qquad \text{eq. 5-34}$$

Although the effect of an error in J_0 may be small compared with the effect on the exponent, nevertheless, a seemingly never-ending debate on the accommodation factor has accompanied the research on nucleation theory since perhaps its beginning.
In general, it is believed that q_C is of the order of the unity (by definition, the accommodation factor can't be greater than one, see chapter 5.2). However, it should be noted that for very small clusters, no reliable way to measure the accommodation factors has been devised which, ultimately, are empirically tuned to make the theoretical trends coincide with experimental data (see for instance Young, 1982). However, whenever the Kantrowitz non-isothermal correction is adopted, this has the fortuitous effect of making J_c almost insensitive to the accommodation factor, at least for values in the range 0,1–1,0 (Bakhtar *et al.*, 2005).

5.4 Droplet growth

In high-speed condensations, the mass of the critical-sized nucleus is very much smaller than the mass of liquid that condenses upon it (Hill 1966). Indeed it is the growth of the droplets that produces the macroscopic changes on the nozzle and ejector dynamics. Consequently, it is very important to accurately calculate this final stage of the condensation process in order to determine the trends of the mixture flow variables (Mach, temperature, pressure and entropy).
In general, the growth of a droplet can be evaluated by computing the fluxes of mass, momentum and energy that cross its surface:

$$\begin{aligned} \frac{dm_d}{dt} &= \Phi_{m\_in} - \Phi_{m\_out} \\ \frac{dm_d \vec{u}}{dt} &= \Phi_{mu\_in} - \Phi_{mu\_out} \\ \frac{dm_d h}{dt} &= \Phi_{h\_in} - \Phi_{h\_out} \end{aligned} \qquad \text{eq. 5-35}$$

where Φ_m,Φ_{mu} and Φ_{mh} are respectively the mass, momentum and energy fluxes entering or leaving the drop surface. Although some authors have proposed general formulation valid for any *Kn* (see Young, 1991), in common practice, these fluxes are calculated differently depending on the size of the droplet.
In particular, the analysis is generally subdivided in three main regimes that depend on the ratio between the droplet radius and the molecular mean free path, i.e., the average distance that a molecule or cluster can travel without incurring in collision with gas particles. This ratio defines a non-dimensional parameter called the Knudsen number:

$$Kn = \frac{\ell}{r_d} \qquad \text{eq. 5-36}$$

During the initial phase of the droplet growth, the liquid embryo is generally much smaller than the mean free path, viz., $Kn>>1$. Under these conditions, the continuum hypothesis does not hold and the calculation of the droplet growth is better achieved by means of kinetic theory concepts. At the other extreme is the situation where $Kn<<1$. In this case the droplet is large enough to apply the macroscopic balances of heat, mass and momentum. The situation in the middle, i.e. $Kn\sim1$, is what is called the transition regime and is the more difficult to analyze[25].
In the case of the free molecular regime ($Kn>>1$) the mass transfer is calculated by evaluating the rate of molecules collision with the drop surface. Thus, the mass conservation equation follows from the balance between the evaporation and condensation rates:

$$\frac{dm_d}{dt} = 4\pi r^2 \frac{dr}{dt} = m\left(\dot{C} - \dot{E}\right) \qquad \text{eq. 5-37}$$

where *m* is the mass of one molecule and *r* is the droplet radius.
Substitution of eq. 5-21 into eq. 5-42 leads to an expression for the time derivative of the droplet radius, which is the quantity of interest:

$$\rho_l \frac{dr}{dt} = \left(q_C \frac{p_v}{\sqrt{2\pi R T_v}} - q_E \frac{p_s(T_l)}{\sqrt{2\pi R T_l}} \right) \qquad \text{eq. 5-38}$$

where the assumption was made that the droplet pressure is equal to the saturation pressure at the droplet temperature (Hill, 1966).
In the case of nozzle flows, it was recognized by many authors (e.g., Wegener and Mack, 1958) that, to a very good approximation, the droplet velocity can be considered equal to that of the surrounding vapor. This is particularly true in the free molecular regime, where the dimensions of the droplets are so small that their inertia can be considered negligible. Consequently, the momentum equation needs not to be calculated for this regime.
The energy balance can be derived by considering the energy transport of each of the molecules condensing or evaporating from the droplet surface (see for example Hill, 1966). Young (1982) provides for a simple expression of the energy balance:

[25] More rigorously Gyarmathy defines two intermediate regimes named the “transitions regime” and “slip regime”, see Gyarmathy (1962) for more details.

$$\rho_l h_{lv} \frac{dr}{dt} = \frac{p_v}{\sqrt{2\pi R T_v}} \frac{c_p + c_v}{2} \cdot \left(T_l - T_v\right) \qquad \text{eq. 5-39}$$

If the vapor conditions temperature and pressure variations are known, eq. 5-38 and eq. 5-39 constitute a set of two equations that can be integrated numerically to give the two unknowns of the system, namely T_l and r. However, in order to reduce further the computational requirements, the prescriptions of a formulation for the droplet temperature, T_l, dispenses from the resolution of the mass conservation equation. We will come back again to this aspect in chapter 6.1.

For the continuum regime, $Kn<<1$, a similar set of equations can be found by considering the conservation of mass, momentum energy of the vapor surrounding the droplet (Young, 1991). By considering a local reference system of spherical coordinates at the center of the droplet, the only non-zero velocity component is the radial velocity and the conservation equations, eq. 5-35, reduce to[26]:

$$\begin{aligned} &\frac{d}{dr}\left(r^2 \rho u\right) = 0 \\ &\left(r^2 \rho u\right)\frac{du}{dr} = r^2 \frac{dp}{dr} \\ &\left(r^2 \rho u\right)\frac{d\left(h + u^2\right)}{dr} = \frac{d}{dr}\left(r^2 k \frac{dT}{dr}\right) \end{aligned} \qquad \text{eq. 5-40}$$

where k is the thermal conductivity of the liquid and it was assumed a steady condensation process.. Integration of the above equation from the droplet surface to the far-field leads to equivalent expressions of eq. 5-38 and eq. 5-39 in the continuum regime (Young, 1982, 1991):

$$\begin{aligned} &\rho_l \frac{dr}{dt} = \sqrt{2\rho_l \left(p_v - p_d\right)} \\ &\rho_l h_{lv} \frac{dr}{dt} = k \frac{dT}{dr} \approx \frac{k}{r}\left(T_l - T_v\right) \end{aligned} \qquad \text{eq. 5-41}$$

where it was assumed a linear temperature variation and p_d is the pressure at the droplet surface.

Things get really involved when Kn approaches unity because none of the two limiting situations described before can be applied without incurring in significant errors. Many interpolations formulae have been proposed to cover this range of conditions (see for example Young, 1982), but their accuracy have never been assessed rigorously (Young, 1991).

Nevertheless, it should be noticed, that in most nozzle experiments the average drop size is usually smaller than one mean free path so that it is possible to use the results of the kinetic theory for predicting mass and energy fluxes to and from the drop surface (Hill, 1966). This however may not be true for simulations of complete ejectors, as will be analyzed in the next chapter.

[26] The complete set of conservation equation in spherical coordinates can be found in appendix B of Bird *et al.*, 2002

Appendix B

Spontaneity of an isothermal and isobaric process

By definition, the specific Gibbs free energy is given by:

$$g = u + pv - Ts \qquad \text{eq. 5-42}$$

For a generic transformation, its variation is computed as follows:

$$dg = du + vdp + pdv - sdT - Tds \qquad \text{eq. 5-43}$$

In the case of isothermal and isobaric transformation, the equation simplifies to:

$$dg = du + pdv - Tds \qquad \text{eq. 5-44}$$

By using the first and second law, it is easy to show that the quantity on the RHS must be either minor or equal to zero:

$$dg = du + pdv - Tds \leq 0 \qquad \text{eq. 5-45}$$

where the equal sign is strictly valid for reversible transformations.

Therefore, under the current settings, a reversible transformation leaves the Gibbs free energy of the system unaltered. If the transformation is not reversible *dg* must diminish. According to this, a spontaneous (irreversible) process that occurs **inside** the system is always accompanied by a decrease in Gibbs free energy.

Hence, the minimum of the Gibbs free energy corresponds to a situation where no other internal transformations are allowed, i.e., to an equilibrium state.

6. Condensing ejector modeling

As a part of the research directed toward the development of "environmentally-safe" refrigeration cycles, a further activity of the doctoral study was aimed at designing a new prototype of steam ejector chiller.
In general, design techniques for ejectors are still a matter of discussion. Ideal gas models are usually employed to easily obtain a first set of basic dimensions (e.g., Eames *et al.*, 1995; Huang *et al.*,1999). However, in the case of steam ejectors, the ideal gas behavior is far from being physically consistent. In order to produce a more refined design, some studies have attempted to include real fluid behavior inside thermodynamic, 1D model of the ejector (e.g. Cardemil and Colle, 2012). However, this was made by postulating thermodynamic equilibrium conditions, which implies overlooking of all the non-equilibrium effects, especially the condensation shock. As a consequence, the design is ultimately conducted by making use of empirical prescriptions or correlations of experimental data (e.g. ESDU, 1986).
Although this method can provide for suitable sizing of the main ejector dimensions, its empirical nature does not permit optimization of the ejector performances. Consequently, the activity of the last part of the doctoral period was aimed at testing existing CFD codes to numerically evaluate steam ejector dynamics and to refine first-attempt designs obtained by approximated techniques.
The work in this context has yielded two important and contrasting conclusions: on the one hand, the theories of nucleation and droplet growth has proved to accurately reproduce results from steam nozzle experiments, on the other hand, the restrictions inherent in the wet steam model (at least the one tested in this study) drastically limit its use for steam ejector applications.

6.1 Wet Steam Model

Wet steam models are available in various commercial CFD softwares. In particular, the present work was aimed at testing the accuracy and reliability of the wet steam model build in the code ANSYS Fluent v.15. Although the model is well described in many references (e.g., Zori and Kelecy, 2005; Yang and Shen, 2009; ANSYS Fluent Theory Guide, 2013), it is useful to briefly describe its main features in order to highlight its main assumptions and restrictions.
The method is based on a fully-eulerian, homogeneous approach. In practice, due to the small size and large number of liquid droplets, the liquid phase is considered to be uniformly dispersed within the vapor volume. Consequently, it is allowed to write the conservation equation for the whole mixture instead of describing the behavior of each separated phase. The properties of the mixture are described by means of mass weighted averages of the corresponding properties of each separated phase:

$$\zeta_m = \beta\zeta_l + (1-\beta)\zeta_v \qquad \text{eq. 6-1}$$

where ζ_m represents any of the mixture thermodynamic properties (e.g. enthalpy, entropy, specific heat, dynamic viscosity or thermal conductivity) and β is the liquid mass fraction defined as:

$$\beta = \frac{m_l}{m_{v+l}} = \frac{\rho_l V_l}{\rho_l V_l + \rho_v V_v} \qquad \text{eq. 6-2}$$

By assuming that the mass fraction during the condensation is small and, specifically, no greater than 0.1, it is easy to show that the expression for the mixture density simplifies to:

$$\rho_m = \frac{\rho_v}{(1-\beta)} \qquad \text{eq. 6-3}$$

The conservation equations for mass, momentum and energy are then written based on the mixture density and are identical to the conventional Navier-Stokes equations for compressible flows (see for example Wilcox, 2006).
Modeling phase change in wet steam flow involves the solution of two additional conservation equations representing the transport of both the number of droplets and their total mass fraction:

$$\begin{aligned} &\frac{\partial \rho_m \beta}{\partial t} + \nabla\left(\rho_m \vec{u} \beta\right) = \Gamma \\ &\frac{\partial \rho_m \eta}{\partial t} + \nabla\left(\rho_m \vec{u} \eta\right) = \rho_m J \end{aligned} \qquad \text{eq. 6-4}$$

where Γ and J are the source terms for the liquid mass fraction and the number of droplets per unit volume, which is defined as:

$$\eta = \frac{\beta}{(1-\beta) V_d \left(\rho_l / \rho_v \right)} \qquad \text{eq. 6-5}$$

where V_d is the average volume of a droplet.
The two source terms in eq. 6-4 describe the two mechanisms of nucleation and droplet growth. In particular, the source term of the η equation is the nucleation rate described in chapter 5.2, which is implemented here in the modified form that accounts for the Kantrowitz' non isothermal correction, eq. 5-30. For clarity, we report the equations below:

$$J_{c\_NISO} = \frac{J_c}{1+\xi} \qquad \text{eq. 6-6}$$

where J_c is the classical nucleation rate and ξ is the non isothermal corrections given by:

$$\begin{aligned} J_c &= q_C \frac{\rho_v^2}{\rho_l} \left(\frac{2\sigma}{\pi m^3} \right)^{1/2} \exp\left(-\frac{16}{3} \frac{\pi \sigma (T_v)^3}{k T_v^3 \left(\rho_l R \ln \varphi_{ss}(T_v) \right)^2} \right) \\ \xi &= q_C \frac{2(\gamma-1)}{(\gamma+1)} \frac{h_{lv}}{R T_v} \left(\frac{h_{lv}}{R T_v} - \frac{1}{2} \right) \end{aligned} \qquad \text{eq. 6-7}$$

The source term for the liquid mass fraction in eq. 6-4 is composed by two terms and is given by:

$$\Gamma = \frac{4}{3} \pi r_c^3 \rho_l J + 4\pi \bar{r}^2 \eta \frac{d\bar{r}}{dt} \qquad \text{eq. 6-8}$$

where the overbar on r indicates the average on the droplet population, calculated by assuming spherical shapes and by using eq. 6-5.

The first of the two addenda in eq. 6-8 represents the mass fraction of the newly generated droplets. This term is significant only in the first stages of the condensation process and it gets rapidly overtaken by the second addendum, i.e., the droplet growth term[27]. This last term requires the definition of the droplet radius time derivative. In chapter 5.4 it was discussed that these expression take different forms depending on the droplet dimension (viz., depending on *Kn*). In practice nozzle flow however, the free molecular path is large due to the very low values of pressure, and *Kn* remain generally well below the value of unity before reaching the nozzle exit (Hill, 1966). Under these hypotheses, it is permissible to retain only the molecular formulations for the droplet growth, eq. 5-38 and eq. 5-39. In addition to this, in chapter 5.4 it was anticipated that in order to reduce further the computational requirements, the prescriptions of a formulation for the droplet temperature, T_l, dispenses from the resolution of the mass conservation equation eq. 5-38.
Within the ANSYS Fluent wet steam model the liquid temperature is assumed to be at the saturation conditions corresponding to the vapor pressure, i.e. $T_l = T_s(p_v)$ (Zori and Kelecy, 2005; Yang and Shen, 2009). Consequently, by inserting this hypothesis into eq. 5-39, the time derivative for the droplet radius is simply given by:

$$\frac{dr}{dt} = \frac{p_v}{\rho_l h_{lv} \sqrt{2\pi R T_v}} \frac{c_p + c_v}{2} \cdot \left(T_s\left(p_v\right) - T_v\right) \qquad \text{eq. 6-9}$$

where all the properties are only function of the vapor thermodynamic conditions.
By making use of eq. 6-6 to eq. 6-9 the two additional transport equations for β and η (eq. 6-4) becomes fully determined. These can be solved together with the mixture conservation equations as long as expressions for the vapor and liquid equation of state, as well as the description of the thermodynamic and dynamic fluid properties (e.g., specific heats, viscosity, etc…), are provided.
Generally speaking, performing non-equilibrium two-phase calculation requires the description of the fluid properties in metastable conditions, meaning that common tabulated properties cannot be used to this purpose. In ANSYS Fluent wet steam model, the steam properties are calculated based on a Virial equation of state truncated at the third term of the expansion:

$$p = \rho_v R T_v \cdot \left(1 + B\rho_v + C\rho_v^2\right) \qquad \text{eq. 6-10}$$

where *B* and *C* are the second and third Virial coefficients. These are function of the sole temperature and are given by two empirical correlations calibrated to match steam data in the range between 273.16 and 1073 K. Moreover, expressions for the enthalpy, entropy and specific heats are derived from the Virial equations based on a procedure described by Young (1988).
In order to perform wet steam calculations, the Virial equation of state must be extrapolated below the saturation curve. Unfortunately, there is a serious lack of experimental data for the properties of steam in supercooled conditions. This is regularly testified by reports of the International Association for the Properties of Water and Steam (IAPWS Certified Research Needs, 2011): "*in the early 90s, the "IAPWS Task Group on Metastable-State Water" (Chairman: H. Sato), performed an extensive investigation on the status and problems in this region. In contrast, to the supercooled and superheated water regions, no experimental data for metastable steam were found. Apparently, no data for metastable steam have appeared since then. Consequently, the present IAPWS recommendation for computation of thermophysical properties of metastable steam is based on extrapolation from the stable region*".

[27] Bakhtar *et al.*(2005) concisely explain this concept by stating that "nucleation supplies the number and droplet growth supplies the mass".

Due to the aforementioned lack of experimental data, the accuracy of the Virial equation could not be evaluated in this region. Nevertheless, Young (1988) states that within the range of conditions commonly attained in low pressure steam turbines, the equations remain well behaved and no anomalies should be expected[28]. Finally, all the other properties (viz., saturated liquid and vapor line, liquid density and specific heats, vapor and liquid dynamic properties) are found by various empirical correlations which are function of the sole temperature (ANSYS Fluent theory guide, 2013).
Before passing on to practical applications, it is useful to repeat and summarize the major assumptions of the model and discuss some of their implications. In doing so, we will focus on those assumptions that seem particularly restrictive with respect to applications in steam ejectors flows, namely:

1. low liquid mass fraction, ($\beta<1$),
2. vapor and liquid temperature above the water triple point temperature (T_v, $T_l>273.16K$),
3. droplet temperature equal to the saturation temperature at the vapor pressure ($T_l=T_s(p_v)$),
4. free molecular regime for droplet growth ($Kn>>1$),

In discussing these aspects, we will proceed in reverse order.
The hypothesis that condensation occurs in the free molecular regime (assumption 4) basically implies the presence of very small droplets in the whole flow domain. Although this may be hold true for most nozzle experiments, in supersonic ejectors it could occur that *Kn* reach values lower than one. This is particularly true in highly underexpanded nozzle, where the expansion of the primary flow carries on well after the nozzle exit plane. By contrast, overexpanded nozzles present an oblique shock that starts right at NXP. The presence of the shock can vaporize most of the droplets or reduce their dimensions (Wegener and Mack, 1956).
As for assumption number 3, the imposition of $T_l = T_s(p_v)$ necessarily implies the equality between the vapor and liquid pressures, $p_l = p_v$. In turn, this implicates that the only driving potential for the droplet growth is the temperature difference between the vapor and liquid phase, which, in this simplified model, coincides with the degree of vapor supercooling, φ_{sc} (see eq. 5-1). In general this is a crude simplification because the droplet growth depends both on thermal gradient as well as on the pressure difference between the two phases[29].
Finally, the most critical restrictions are probably those connected to the ice formation (i.e., $T>273,16\ K$) and to the assumption of low values of liquid mass fraction.
This is particularly true for supersonic ejector applications where efficiency considerations impose the use of low or no level of superheating at the inlet of steam ejectors. Consequently, the motive flow can reach very low levels of temperature and pressure and the aforementioned limits are commonly exceeded[30].
In particular, reaching vapor temperatures below 273 K can lead at least to two problems: first the vapor properties may not be well described or show anomalous trends, second, ice may form inside the ejector. In this last case, no numerical solution can exist. However, the temperature of the droplet is generally well above that of the vapor so that enough margin should generally exist before ice starts to form[31].

[28] Young (1988) further states that accuracy may deteriorate approaching the critical point, in particular, the equations should not be trusted for entropy values lower than 5.8 [kJ/kgK]
[29] This is clearly demonstrated by Young (1991) who, by means of irreversible thermodynamics, derives a general formulation for the droplet growth which account for both pressure and temperature gradient valid for all *Kn* numbers.
[30] Some design procedure tend to design underexpanded ejectors by considering that secondary flow is accelerated by a virtual fluid dynamic nozzle created by the expansion of the primary jet. Consequently, this effect is even more exacerbated for these ejectors
[31] Moreover, even for the liquid phase some degree of supercooling usually exists, this is because ice crystal formation, in much the same way as droplet formation, is fundamentally a time dependent phenomenon

Finally, the limit related to the maximum liquid mass fraction is mainly connected to numerical stability aspects: high values of liquid mass fractions imply large source terms in the energy equations, and significant density variations that cause numerical instability. Unfortunately, as will be explained in chapter 6.3, supersonic ejector in steam ejector chillers operate most of the times in range of liquid mass fraction well above the limit of 0,1 (i.e., qualities below 0.9). Therefore, the overcoming of this last assumption basically requires the development of a new, improved numerical scheme.

6.2 Nozzle flow

In general there are two ways of testing nucleation and droplet growth theories, the first, more appropriate for fundamental physics investigations, involves condensation in cloud and expansion chambers; the second, which is more suited for engineering studies, deals with supersonic expansions in De Laval nozzles. As it was shown by many authors (e.g., Wegener and Mack, 1956; Hill, 1966), the converging/diverging nozzle is a remarkable test bench for wet steam model theories. The advantages of this type of experiment are numerous: first of all, the "simplicity" of the steady isentropic flow, which can be easily reproduced by Q1D calculations. In turn, this allows marking the effects of condensation by simple pressure measurements, as will be illustrated shortly. Moreover, it has been shown by Stodola (1927, see also Hill, 1966)) that for this type of expansion the effects of dust particles are entirely insignificant, meaning that the condensation is of the homogeneous type. The only drawback of nozzle experiments is that nucleation and droplet growth are tightly coupled and is hard to validate the theories separately (Bakhtar *et al.*, 2005).

Among the many nozzle experiments that can be found in the literature, that of Moore *et al.* (1973) appears to be one of the most popular test case for validating wet steam models (e.g., Gerber, 2002; Bakhtar et al, 2005; Simpson and White, 2005; and many others). Moreover, the same geometry has been used several times for testing the ANSYS Fluent version of the model (e.g., Zori and Kelecy, 2005; Yang and Shen, 2009; Sharifi *et al.*, 2013; Ariafar *et al.*, 2014).

In what follows, the ANSYS Fluent wet steam model is tested by comparison with a different, though still classical, nozzle experiment: that of Moses and Stein (1978). In their paper, the authors performed numerous tests over a wide range of starting conditions and the condensation was documented with both static pressure and light scattering measurements.

In order to test the wet steam model, the numerical results are compared with experimental data for the axial profiles of static pressure and liquid mass fraction. The numerical scheme adopted for these tests is described in Fig. 6.1. The grid dependence was checked by comparison of three different meshes of respectively 6k, 12k and 24k quad elements. The independent solution was found for the intermediate mesh, which was retained for all subsequent calculations.

Numerical scheme
2D axisymmetric domain
2nd order accurate, density based solver
Structured grid, 12k quads, wall resolved
k-ω SST turbulence model

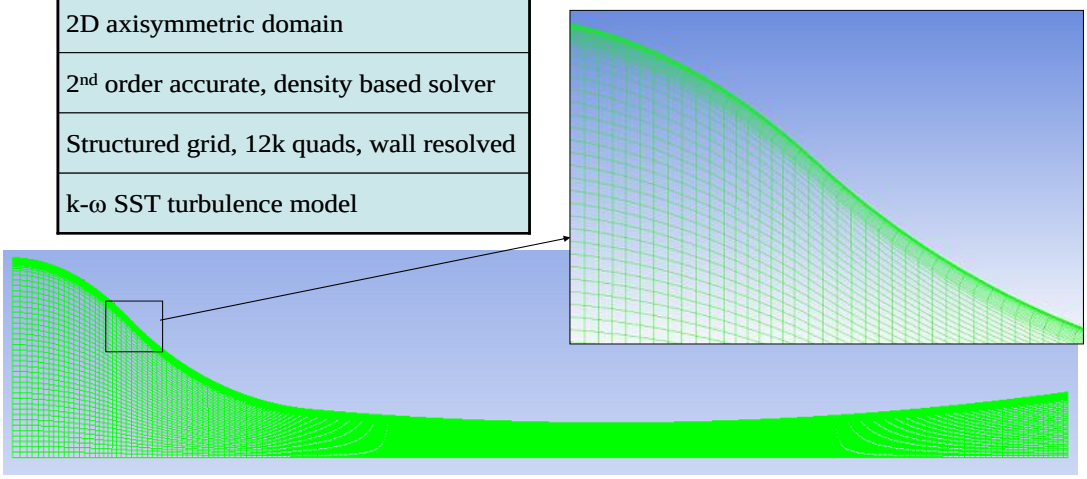

Fig. 6.1 – Numerical scheme and computational domain for the Moses and Stein (1978) test case

Although Moses and Stein (1978) performed tests for a great number of different conditions, only for few experiments did the authors reported data for the pressure profiles along the nozzle axis.
In particular, Fig. 6.2 and Fig. 6.3 show the results for two set of experiments performed by keeping fixed the inlet pressure while varying the inlet temperature (Fig. 6.2) and vice versa (Fig. 6.3). As can be seen, for all the tested cases the agreement is excellent both in terms of condensation starting position and asymptotic pressure trend.
The two sets of curves also show the main features and effects caused by the non-equilibrium condensation. Due to the concentrated heat release, the pressure curves deviate significantly from the hypothetical dry isentropic trend (the dotted curve on each figure). This brings about many undesirable effects. First of all, the non-equilibrium heat transfer between the two phases causes the entropy to increase, thus producing losses and reducing the nozzle efficiency. Secondly, the trends of pressure and Mach number are altered. This has consequences on the subsequent development of the mixing layer because increasing the nozzle exit pressure impacts on the correct expansion of the primary flow. In practice, if the primary nozzle of a supersonic ejector is designed to be perfectly expanded under a specific set of conditions, the pressure increase would cause the primary jet to become underexpanded. Consequently, in addition to direct losses caused by the heat transfer, condensation can cause indirect losses due the increase of the shock diamonds intensity in the mixing chamber.

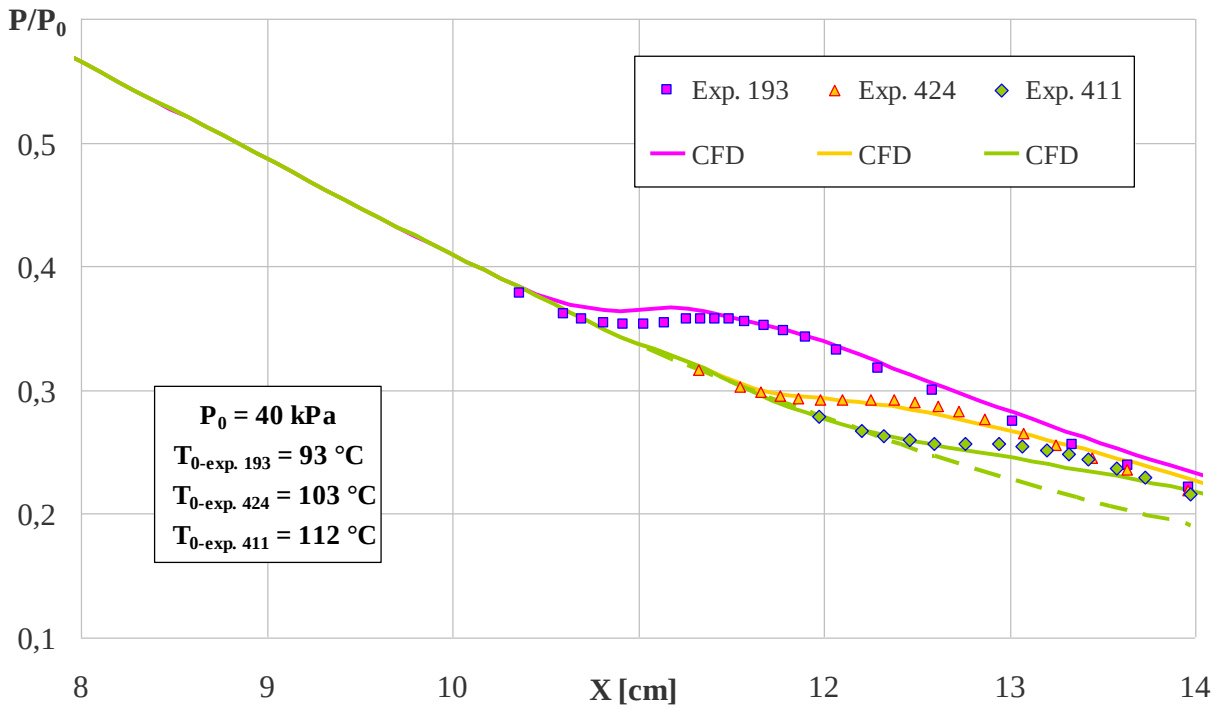

Fig. 6.2 – Axial trends of static pressure for three experiments with increasing inlet temperature

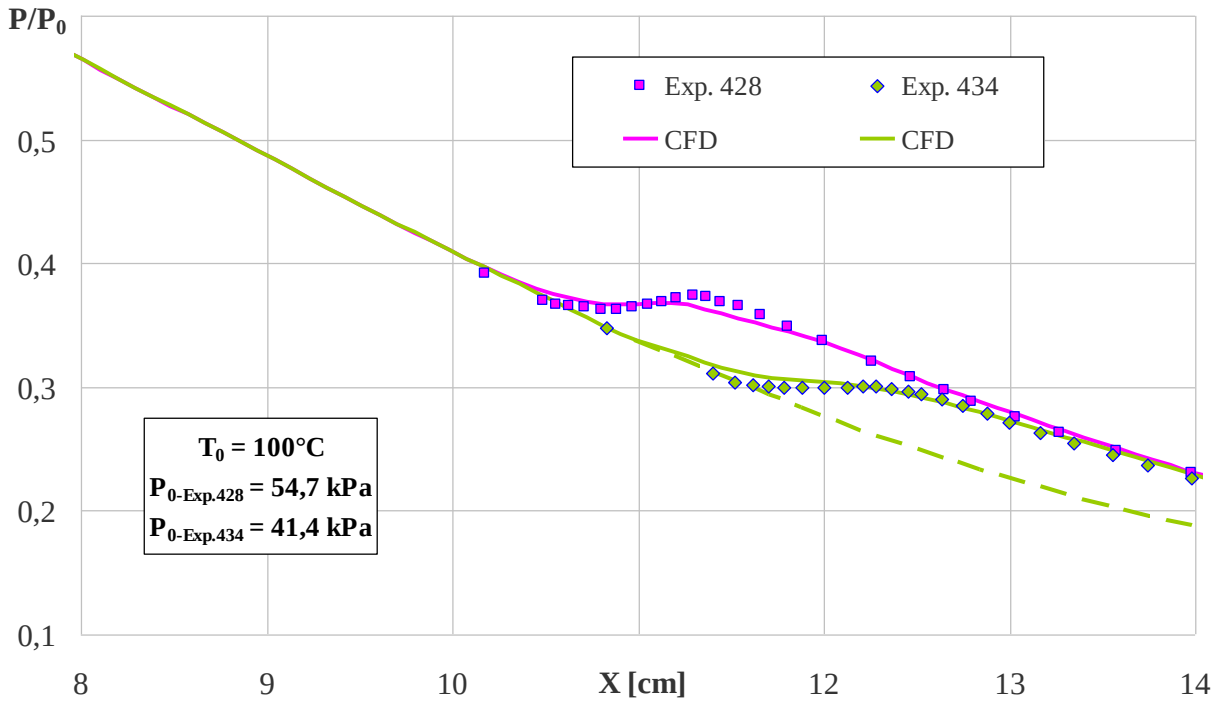

Fig. 6.3 – Axial trends of static pressure for two experiments with decreasing inlet pressure

The agreement that is seen at condensation onset mostly depends on the accuracy of the nucleation rate equation. In particular, the point at which the pressure differs from the isentropic value by 1 percent is commonly referred as the "onset of condensation". In their paper, Moses and Stein report data for this quantity in a wide range of conditions. In order to further test the accuracy of the wet steam model, and in particular of the nucleation rate equation, additional simulations were performed to compare results for the onset of condensation.

Tab. 6.1 shows a summary of the comparison. From inspection of the different cases, it can be seen that the difference between the experimental and numerical results is always around 1%. Moreover, it is interesting to note that the accurate matching holds even for experiments where the minimum vapor temperature was below 0°C[32].

	T_0 [°C]	P_0 [Pa]	T_{onset} [°C]	P_{onset}[Pa]	φ_{ss_onset}	x_{Exp} [cm]	x_{CFD} [cm]	Error
Exp. 191	96,1	17812	-15,8	3906	21,7	13,26	13,37	*-0,8%*
Exp. 193	92,9	43023	12,8	15252	10,3	10,74	10,56	*1,7%*
Exp. 234	97,9	34957	6,4	11012	-	11,49	11,64	*-1,3%*
Exp. 244	110,4	26944	-6,0	6199	-	13,18	13,37	*-1,4%*
Exp. 248	108,8	19492	-17,5	3840	-	14,1	14,2	*-0,7%*
Exp. 252	101,2	40050	9,6	12292	10,3	11,5	11,47	*0,3%*

Tab. 6.1 – Onset conditions for various experiments, comparison between numerical and experimental data (in blue are the vapor onset temperature below 0°C)

In order to check the accuracy of the droplet growth formulation, the numerical trend for the liquid mass fraction can be compared with those obtained by light scattering measurement. Unfortunately, Moses and Stein report only one of such profiles. Nevertheless, even for this one case the agreement between theory and experiments is remarkable, as shown in Fig. 6.4.

Despite the surprisingly good agreement of all presented trends, it should be noted that the comparison are made only on global macroscopic variables, whereas a better assessment of the theory should be done by comparing the results on the population of droplets and their size distributions. In this case, the agreement is much more difficult to achieve and different combinations of theoretical models and calibrating parameters can give comparable levels of agreement with experiments (see Bakhtar *et al.*, 2005).

[32] Temperatures below zero do not necessarily lead to ice formation. As was detailed in chapter 5.4, the droplet temperature is always much higher than that of the vapor and close to the liquid saturation temperature.

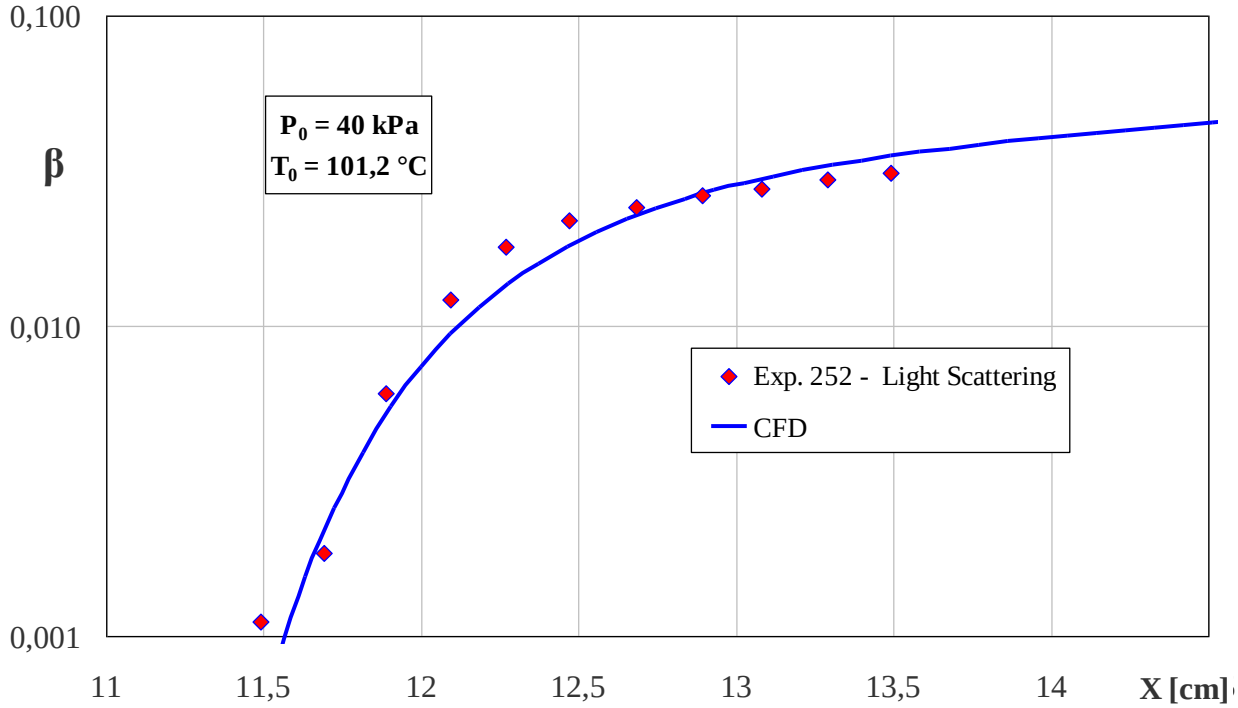

Fig. 6.4 – Axial trends of liquid mass fraction, comparison of experimental and numerical trends

6.3 Steam ejectors

Although a good level of accuracy is generally achieved for nozzle flows, the same may not hold true in supersonic ejector applications where the presence of liquid droplets may induce many unpredictable effects. First of all, the interaction between droplets and turbulent vortical structures can change the turbulence intensity levels (Crowe *et al.*, 2012). In turn, variation of the turbulence intensity can impact the mixing layer development and, consequently, the attending entrainment effect (where higher turbulence levels cause higher entrainment and vice versa). Moreover, the heat release due to the condensation shock can suppress the boundary layer development and change the position and intensity of dynamic shocks inside the ejector (Wegener and Mack, 1956). Finally, whenever a wet flow crosses a compressive shock, the different inertia between vapor and liquid droplets induces a velocity mismatch that generates drag and friction losses (d'Agostino, 2015). These and many other subtle effects can hardly be captured by simple RANS simulations. Therefore, it is reasonable to expect a poorer agreement between numerical simulations and experiments in case of supersonic ejector flows.

In order to accurately test the accuracy of the wet steam model on ejector applications, the comparison with experimental data should be made by considering both global and local parameters. Unfortunately, articles reporting both these type of data appears to be very few. In particular, the only one work that the author could find is the study of Chunnanond and Aphornratana (2004) and the subsequent work of Sriveerakul *et al.* (2007). In this last paper Sriveerakul *et al.* presented detailed investigations of both mass flow rates and pressure profiles along the ejector external walls. Moreover, the authors performed CFD simulations using the ideal gas approximation which, however, showed some discrepancies with experimental data. In order to compare with wet steam model simulations, the geometry investigated by Sriveerakul *et al.* (2007) was precisely reproduced. Fig. 6.5 shows the resulting computational domain and the numerical scheme used for all the CFD computations.

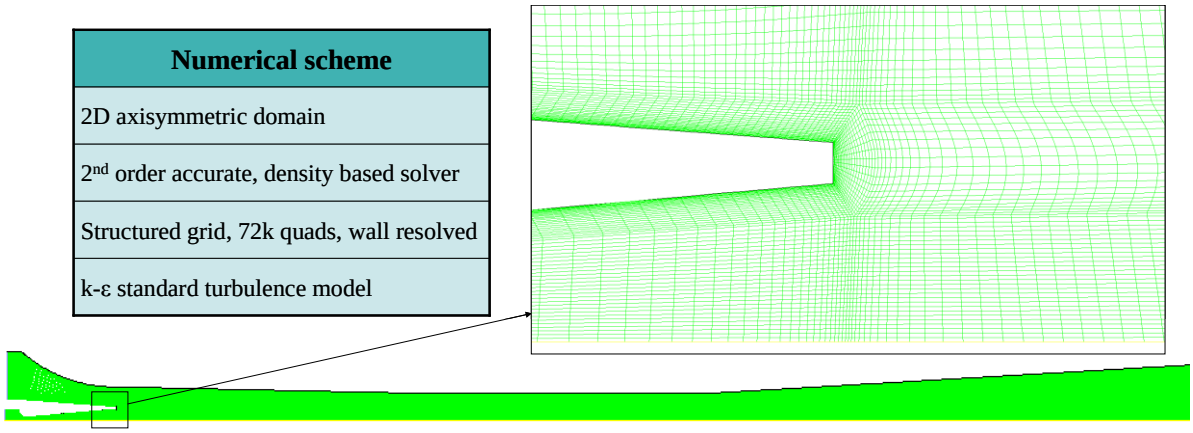

Fig. 6.5 – Numerical scheme and computational domain used to reproduce experimental data from Sriveerakul *et al.* (2007)

Unfortunately, in all the experiments of the paper no superheating is imposed at the nozzle inlet and the motive steam expands well into the two phase region, as shown in Fig. 6.6. As a consequence the value of the mass fraction largely surpasses the 0.1 limit discussed in chapter 6.1. This caused the impossibility of performing any stable simulation in the conditions tested by the authors. Therefore, a large value of overheat was imposed at the nozzle inlet in order to reduce the final quality of the vapor. The first converged solution was found for an overheat level of around 480°C (minimum quality of around 0.98). Subsequently, in the attempt to reach more realistic conditions a slow temperature descent was imposed at the motive inlet. Unfortunately, due to numerical instabilities it was not possible to go below an overheating of 420°, as shown in Fig. 6.6 (meaning a final minimum quality of around 0.95). Many other trials were made which confirmed the impossibility of reaching liquid mass fraction even close to the 0.1 limit.

Nevertheless, even for these unrealistic operating conditions, the liquid mass fraction and all other typical "two-phase quantities" present interesting trends that is worth investigating. In particular, we will limit our analysis to the trends along the axis of the ejector, because this is the region where most of the two-phase phenomena occur.

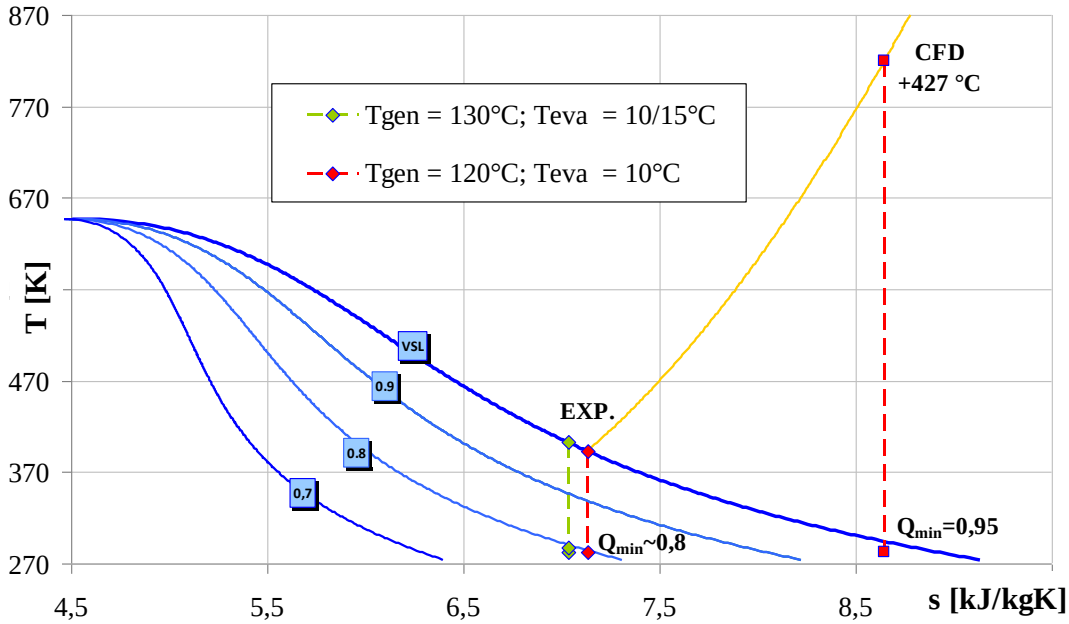

Fig. 6.6 – *T-s* diagram showing the nozzle inlet and outlet conditions of the ejector tested by Sriveerakul *et al.* (2007) and the conditions under which CFD simulations could converge

Fig. 6.7 shows the pressure and liquid mass fraction profiles along the axis in the region right after the primary nozzle exit. CFD and experimental results show that in this region the motive flow keeps on expanding due to an imperfect matching of the pressure conditions at nozzle exit (the primary nozzle is highly underexpanded in all operating conditions investigated by Sriveerakul *et al.*, 2007). Consequently, the static pressure reaches minimum values of the order of few hundreds Pascal (near or below the triple point pressure). As shown in Fig. 6.7, it is in correspondence of this minimum that the condensation shock appears and the liquid mass fraction rise to appreciable values.

However, immediately after the minimum, the pressure increases abruptly due to appearance of the first compression wave (or weak oblique shock) that is generated by the underexpansion of the primary jet. Due to the localized pressure and temperature increase all the liquid mass evaporates and the liquid mass fraction goes back to zero. This can also be seen by looking at Fig. 6.8 which shows the trend of the liquid generation rate versus its corresponding driving potential, namely, the degree of supercooling, φ_{sc} (see eq. 6-9). As soon as the degree of supercooling becomes positive the liquid starts to form. However, it is only at 40-50°C of supercooling that the generated mass becomes detectable. After the shock, the temperature increase brings φ_{sc} to negative values and the liquid mass evaporates.

Finally, Fig. 6.9 shows the same trend but focusing on the number of droplets. In particular, it should be noted that the maximum number of droplets reaches values of 10^{20} *droplets* m^3 and that this number doesn't go to zero after the shock. However, this is simply a numerical issue due to the absence of a "dissipation or sink term" in the droplet transport equation, eq. 6-4. Indeed, the same figure shows that the average radius of the droplets goes to zero, meaning that all the droplets are evaporated.

In conclusion, it is important to highlight the fact that while the theories of nucleation and droplet growth have proved to reproduce with surprisingly good accuracy the results in steam nozzle experiments, the restrictions inherent in the wet steam model adopted in this work drastically limit its use for steam ejector applications. In particular, the most critical restriction is that connected to the liquid mass fraction. As anticipated in chapter 6.1, this limit is mainly connected to numerical stability aspects and its overcoming requires the development of a new, improved numerical scheme. This will be the goal of future research.

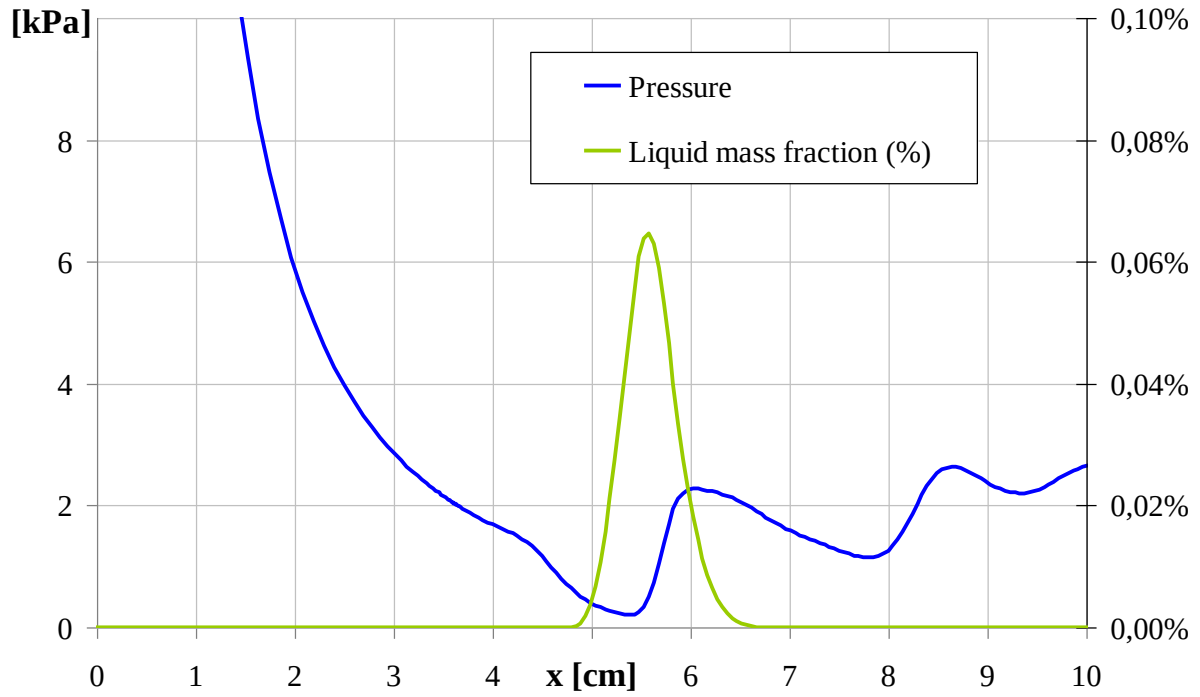

Fig. 6.7 – Trends of pressure (left axis) and liquid mass fraction (right axis) along the ejector axis of symmetry

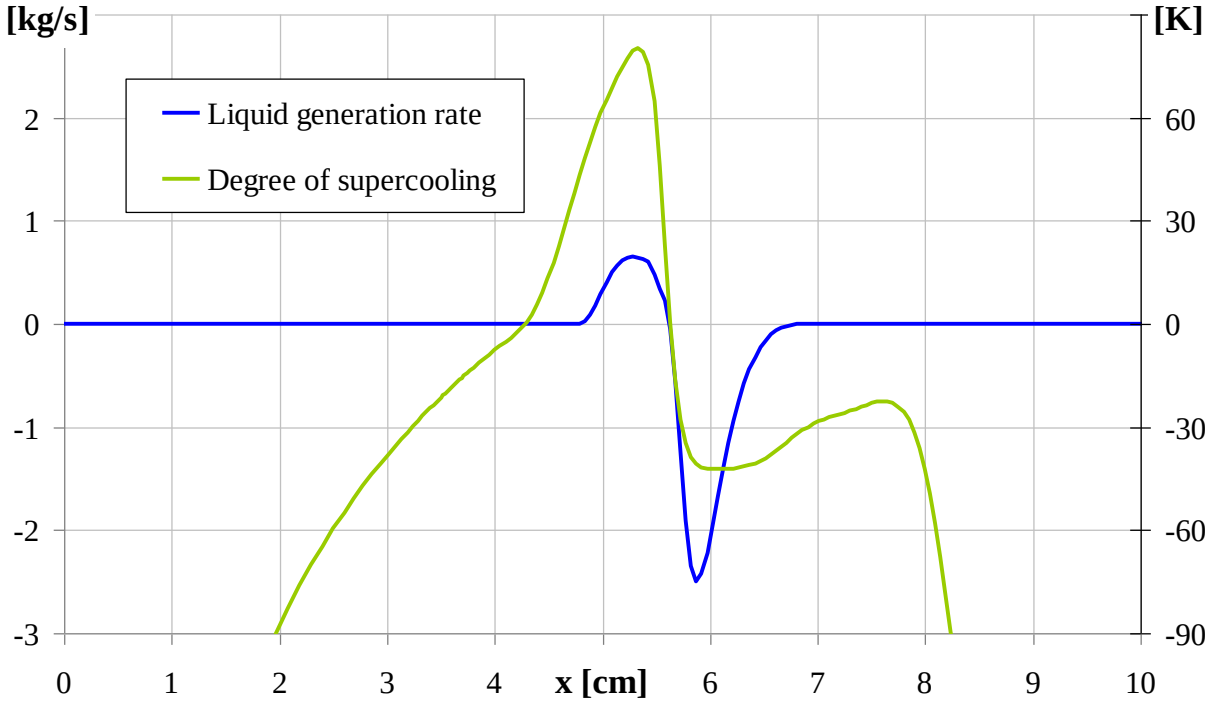

Fig. 6.8 – Trends of liquid generation rate (left axis) and degree of supercooling (right axis) along the ejector axis of symmetry

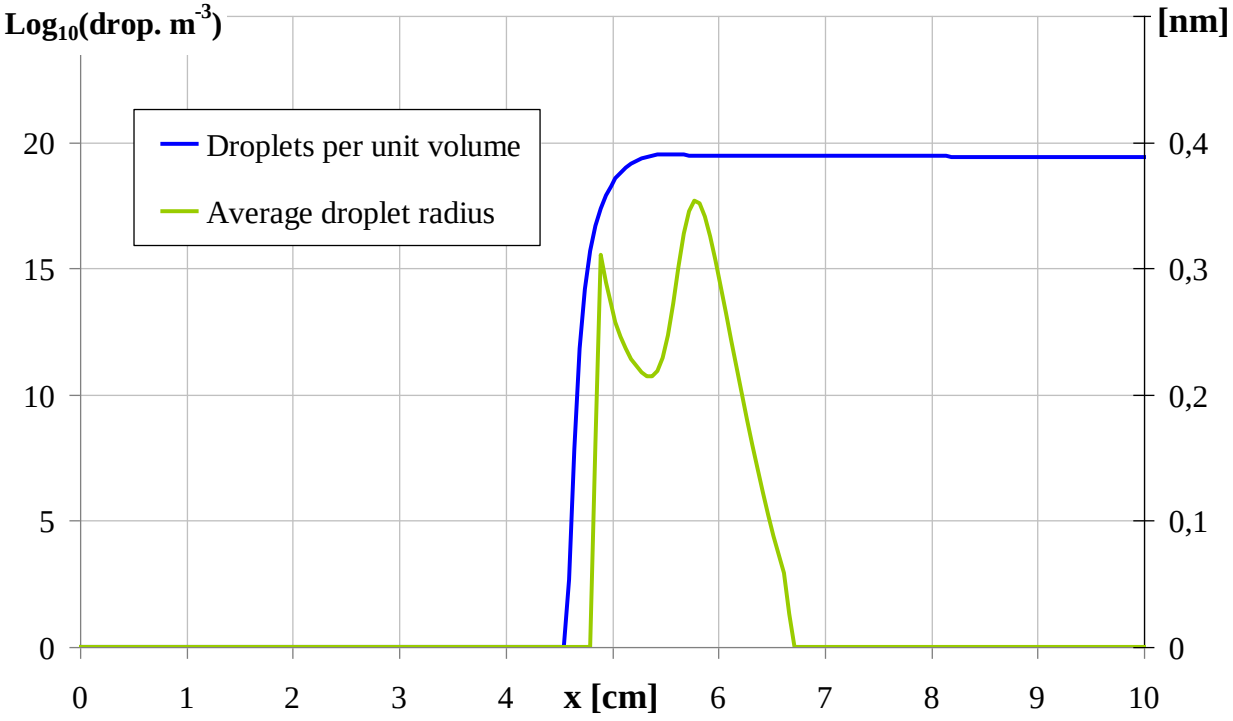

Fig. 6.9 – Trends of droplets per unit volume (left axis) and average droplet radius (right axis) along the ejector axis of symmetry

References

ANSYS Fluent Theory Guide, 2013, release 15.0, ANSYS Inc., Canonsburg, PA

Ariafar, K., Buttsworth, D., Sharifi, N., Malpress, R., 2014. Ejector primary nozzle steam condensation: Area ratio effects and mixing layer development Applied Thermal Engineering, 71, 519-527.

Bakhtar, F., Young, J.B., White, A.J., Simpson, D.A., 2005. Classical Nucleation Theory and Its Application to Condensing Steam Flow Calculations, Proceedings of the Institution of Mechanical Engineers, Part C: Journal of Mechanical Engineering Science, 1315-1333.

Bird, R.B., Stewart, W.E., Lightfoot, E.N., 2002. "Transport phenomena, second edition", John Wiley and Sons

Brennen, C.E., 2013. Cavitation and Bubble Dynamics, Paperback reprinting by Cambridge University Press.

Cardemil, J.M., Colle, S., 2012, A general model for evaluation of vapor ejectors performance for application in refrigeration, Energy Conversion and Management 64 79–86

Carey, V.P., 1992. Liquid-Vapor Phase-Change Phenomena : An Introduction to the Thermophysics of Vaporization and Condensation Processes in Heat Transfer Equipment. Taylor & Francis Series Group, LLC, New York, N.Y.

Crowe, C.T., Schwarzkopf, J.D., Sommerfeld, M., Tsuji, Y., 2012. Multiphase flow with droplets and particles, Second edition, CRC press

d'Agostino L., 2015. Private communication

Eames IW, Aphornratana S, Haider H., "A theoretical and experimental study of a small-scale steam jet refrigerator", International Journal of Refrigeration 18(6) (1995) 378–86.

ESDU, 1986. Ejectors and jet pumps, Data item 86030, ESDU International Ltd, London, UK, 1986.

Ford, I., 2013. Statistical Physics An Entropic Approach, John Wiley & Sons, Ltd.

Ford, I.J., 2004. Statistical mechanics of water droplet nucleation. Proceedings of the Institution of Mechanical Engineers, Part C: J. Mechanical Engineering Science, 218(C8), 883–899.

Gerber, A.G., 2002. Two-Phase Eulerian/Lagrangian Model for Nucleating Steam Flow, Journal of Fluids Engineering, Vol. 124, 465-475.

Grazzini, G., Milazzo, A., Piazzini, S., 2011. Prediction of condensation in steam ejector for a refrigeration system, International Journal of Refrigeration 34, 1641-1648.

Gyarmathy, G., 1962. Bases for a theory for wet steam turbines (translated from German: "Grundlagen einer Theorie der Nassdampfturbine"), Doctoral Thesis No. 3221, ETH Zurich

Gyarmathy, G., 1982. The spherical droplet in gaseous carrier streams: review and synthesis, in Multiphase Science and Technology, 1 (1), 99- 279

Hill, P.G., 1966. Condensation of water vapour during supersonic expansion in nozzles, Journal of Fluid Mechanics, 25, 593–620.

Huang, B.J., Chang, J.M., Wang, C.P., Petrenko, V.A., 1999. 1-D analysis of ejector performance, International Journal of Refrigeration 22, 354-364.

IAPWS Certified Research Need, ICRN 28, 2011. Thermophysical Properties of Metastable Steam and Homogeneous Nucleation

Kantrowitz, A.,1951. Nucleation in very rapid vapour expansions. J. Chem. Phys., 19, 1097–1100.

Moore, M.J., Walters, P.T., Crane, R.I., Davidson, B.J. , 1973. Predicting the fog drop size in wet steam turbines, In Wet steam 4, 101–109.

Moses, C.A., Stein, G.D., 1978. On the Growth of Steam Droplets Formed in a Laval Nozzle Using Both Static Pressure and Light Scattering Measurements, Journal of Fluids Engineering, 100, 311−321.

Sharifi, N., Boroomand, M., Sharifi, M., 2013. Numerical assessment of steam nucleation on thermodynamic performance of steam ejectors, Applied Thermal Engineering 52, 449-459.

Simpson, D.A., White, A.J., 2005. Viscous and unsteady flow calculations of condensing steam in nozzles, International Journal of Heat and Fluid Flow 26, 71–79.
Stodola, A., 1927. Steam and Gas Turbines, New York: McGraw-Hill.
Wegener, P.P., Mack, L.M., 1958. Condensation in supersonic and hypersonic wind tunnels, in: Advances in Applied Mechanics, Academic Press Inc., New York, NY.
Wilcox, D.C., 2006. Turbulence Modeling for CFD. DCW Industries, Inc, La Canada, CA.
Yang, Y., Shen, S., 2009. Numerical simulation on non-equilibrium spontaneous condensation in supersonic steam flow, International Communications in Heat and Mass Transfer, 36, 902–907.
Young, J.B., 1982. The spontaneous condensation of steam in supersonic nozzles. Physico Chemical hydrodynamics (PCH), 3, 57–82.
Young, J.B., 1988. An equation of state for steam for turbomachinery and other flow calculations. Trans. ASME, J. Engng Gas Turbines and Power, 110, 1–7.
Young, J.B., 1991. The condensation and evaporation of liquid droplets in a pure vapour at arbitrary Knudsen number. Int. J. Heat and Mass Transfer, 34, 1649–1661.
Zori, L., Kelecy, F., 2005. Wet Steam Flow Modeling in a General CFD Flow Solver, 35th AIAA Fluid Dynamics Conference and Exhibit 6 - 9 June 2005, Toronto, Ontario Canada

Conclusions

The structure of the present work, as well as the path of the doctoral research, has moved from the general analysis of ejector refrigeration cycles to the more specific study of single- and two-phase supersonic ejectors. In each analysis, investigation started first with a theoretical and phenomenological point of view. This was prompted by the understanding that major advancements in this field may only come from a deeper knowledge of the physics of high-speed flows.
The major results of this thesis have emerged from both experimental and numerical activities. The initial purpose of the experimental work was to improve the performance of the prototype chiller built by the University of Florence in cooperation with Frigel S.p.A. The chiller, which is intended for industrial refrigeration applications, has a nominal cooling power of 40 kW and is powered by low temperature heat (from 90 up to 100 °C). The ejector is equipped with a movable primary nozzle and 9 static pressure probes along the mixing chamber/diffuser duct. The working fluid is R245fa.
Preliminary numerical analysis on this prototype has shown that the primary nozzle was operating under highly overexpanded conditions. This issue was corrected by simulating different primary nozzles with increasingly lower levels of expansion. The trials were followed by the manufacturing and installation of the nozzle that gave the best results under the specific operating conditions required by the industrial partner. The adoption of the new primary nozzle yielded the expected improvements and now the system has reached high levels of efficiency, similar or greater than those published by other authors.
However, the increase in system COP was not associated with an equivalent increase of the critical pressure. In order to further improve the ejector performance, numerical tools were deemed to be necessary. Therefore, the subsequent activity concentrated on obtaining a reliable set of experimental measurements for comparison with CFD simulations. After some tuning of the chiller measurement system, two performance curves were extracted. The repeatability of experimental results was difficult due to some instabilities of the operating conditions (the chiller was tested in a real industrial environment). For this reason, a careful uncertainty analysis was performed in order to understand the level of confidence of the experimental data and to make coherent comparison with numerical results.

The CFD results of the single-phase ejector have shown a good agreement with experimental data, both in terms of mass flow rates and wall pressure profiles. These results were achieved thanks to careful set-up of the numerical scheme and to a correct analysis of the heat and momentum transfer at wall. In particular, this last feature should be always considered with great care.
Most of the work that can be found in the literature focuses on the validation and testing of different turbulence models. This is due to the idea that the large discrepancies commonly found at off-design conditions are caused by turbulence modeling approximations. Although this may represent a source of error, it should by no means be considered the only or the most important source of discrepancy with experimental data. Indeed, the fact that the prediction of mass flow rates is generally accurate at on-design conditions indicates that the entrainment process is well captured by CFD simulations. In turn, this is mostly due to turbulence model accuracy in predicting the shear work and turbulence intensity inside the mixing layer of the ejector.
By contrast, the large discrepancies seen at off-design conditions should be attributed to the failure in reproducing the total pressure losses inside the mixing chamber and upstream of the diffuser shock. Due to the high flow speed and compressibility, pressure losses are mostly dictated by friction at the wall. The present work suggests that by taking friction into account the transition to off-design conditions can be predicted with great accuracy, thus increasing the overall agreement of numerical simulation with experimental data (this effect may even be more significant in smaller-scale ejectors).
Moreover, by removing the usual assumption of adiabatic walls, it is seen that the average heat transfer coefficient along the ejector can by no means be considered negligible. Although the total heat loss toward the environment may be safely neglected in the global balance of the ejector chiller, the heat transfer at wall impacts the stability of the boundary layer in ways that are difficult to predict.

Consequently, it is clear that the usual approximation of "smooth and adiabatic walls" should be carefully reconsidered if an adequate level of accuracy is to be found in numerical simulations.

Although the use of CFD RANS simulations represents an accurate and relatively simple tool to predict the performance of single-phase ejectors, the same tools are not yet a viable solution for design purposes.
Generally speaking, the common practice is to use simple 1D models to compute the main geometric characteristics of the ejector, which are subsequently refined according to empirical relations. These methods are generally inadequate for thermodynamic optimization, as they are unable to predict system efficiency as a function of ejector design. In most cases, models overlook the dynamics of turbulent mixing and only consider global momentum balances adjusted through simple efficiency parameters. Yet turbulent mixing is arguably the most important process occurring inside ejectors, as it determines the amount of suction flow entrainment and a considerable share of the total system's thermodynamic losses.
Therefore, an analytical scheme was devised that captures the basic features of the turbulent mixing zone. The model improves a previous scheme found in the literature and is able to compute all flow properties inside an axisymmetric or planar mixing chamber with either constant or variable cross section. The amount of secondary flow entrainment, the work and heat exchange between the primary and secondary flow, the pressure losses and the mixing efficiency are computed as a function of the system geometry and without use of any arbitrary parameters. Consequently, this model is particularly suited for a thermodynamic optimization of the ejector system.
The model was validated with a comparison to CFD results for various operating conditions. Results generally showed good agreement in all parameters, with increasing errors as pressure gradients increased. In particular, discrepancy between numerical and theoretical Entrainment Ratio was generally well below 10%. Moreover, the analysis of the same equations that were used in the model allowed for an understanding of one of the main problems in the optimization of a supersonic ejector: the decrease of mixing effectiveness with increasing primary stream Mach number. A way to work around this problem is to enlarge and optimize the contact surfaces between primary and secondary stream. A preliminary study was performed in this direction by using the model developed in this study. Results demonstrated that splitting the primary mass flow into several smaller nozzles (ceteris paribus), notably increases the entrainment of the secondary flow.

The last part of the thesis addressed the issues connected to high-speed, two-phase simulations. In this respect, the numerical modeling of flashing ejector is still relatively undeveloped and was not considered in this work. As for condensing ejectors, the wet steam theory and models have long been used in the context of steam turbine research.
The activity in this field has yielded two important and contrasting conclusions. First, the theories of nucleation and droplet growth have proved to reproduce, with surprisingly good accuracy, the results in steam nozzle experiments. Conversely, the restrictions inherent in the wet steam model adopted in this work drastically limit the use of this method for steam ejector applications. In particular, the most critical restrictions are those connected to the ice formation (i.e., $T>273{,}16\ K$) and to the assumption of low values of liquid mass fraction. Unfortunately, efficiency considerations impose the use of low or no level of superheating at the inlet of steam ejectors, as well as the reduction of the shock diamonds formations at exit of the primary nozzle. Consequently, the expansion of steam can reach very low levels of temperature and pressure, meaning that any or both the aforementioned limits are commonly exceeded.
While the minimum temperature may be lowered by assuming some degree of water supercooling, the second limit is mainly connected to numerical stability aspects and overcoming these challenges may require the development of new and improved numerical schemes. Therefore, at the present moment, the wet steam model seems to be unsuitable to predict steam ejectors flows unless significant levels of superheat and overexpansion are imposed at the motive nozzle inlet and outlet, respectively.

The author is grateful to all the people without whom this work would not have been possible. First of all, my incomparable supervisors Prof. Grazzini and Dr. Milazzo, who constantly supported me and pushed me to succeed. Secondly, my gratitude goes to Prof. Bartosiewicz, Isabelle Hennau and all of the TFL group that kindly and warmly welcomed me during my stay at UCL. Special thanks go also to Dr. Adrienne B. Little, who tolerated my "hair-splitting approach" on paper writing, to Dr. Dario Paganini, Dr. Simone Salvadori, Dr. Antonio Andreini, Francesco Giacomelli and Giulio Biferi, who helped me in many ways.
Lastly, I would like to dedicate this work to my family and to Lisa, who are always there when I need it.